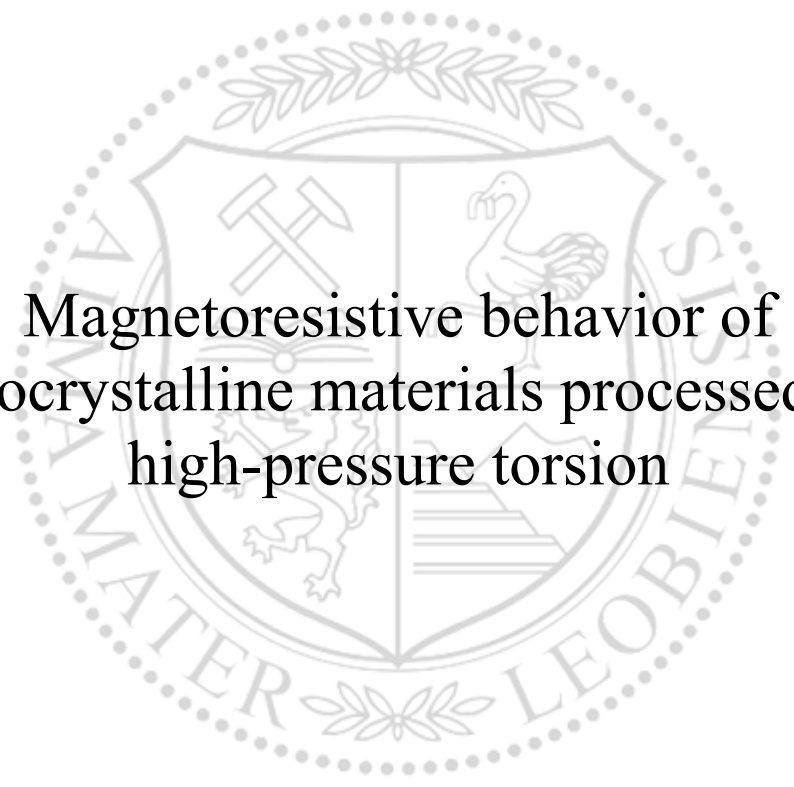




Chair of Materials Physics

Master's Thesis



Magneto-resistive behavior of  
nanocrystalline materials processed by  
high-pressure torsion

Manoel Kasalo, BSc

February 2022



**EIDESSTATTLICHE ERKLÄRUNG**

Ich erkläre an Eides statt, dass ich diese Arbeit selbständig verfasst, andere als die angegebenen Quellen und Hilfsmittel nicht benutzt, und mich auch sonst keiner unerlaubten Hilfsmittel bedient habe.

Ich erkläre, dass ich die Richtlinien des Senats der Montanuniversität Leoben zu "Gute wissenschaftliche Praxis" gelesen, verstanden und befolgt habe.

Weiters erkläre ich, dass die elektronische und gedruckte Version der eingereichten wissenschaftlichen Abschlussarbeit formal und inhaltlich identisch sind.

Datum 26.02.2022

---

Unterschrift Verfasser/in  
Manoel Kasalo

## **Acknowledgments**

I want to thank Univ.-Prof. Dr. Jürgen Eckert and Dr. Andrea Bachmaier for the excellent supervision in this master thesis.

My further thanks go to Stefan and Martin, who supported me with their expertise in the theoretical and experimental parts of the work. I also appreciate the assistance of the rest of the team members, including Lukas, Michael, and Alexander. Additional thanks to Peter Kutlesa, who assisted me with technical problems at the HPT, and to the metallographers who prepared the samples.

This project received funding from the European Research Council (ERC) under the European Union's Horizon 2020 research and innovation program (Grant No. 757333).

## Kurzfassung

Nanokristalline Werkstoffe, die einen granularen Riesenmagnetowiderstand aufweisen wurden mittels Hochdruck-Torsionsverformung hergestellt. Dafür wurden nicht mischbare binäre und ternäre Legierungen untersucht, die aus nichtmagnetischen (Ag, Cu und Cr) und ferromagnetischen (Co, Fe und Ni) Elementen bestehen. Der ferromagnetische Anteil wurde auf 20 Vol.-% festgelegt, da ein Maximum im Magnetowiderstand erwartet wird. Zusätzlich wurde ein ferromagnetischer Anteil von 40 Vol.-% für Cu- und Cr-basierte Zusammensetzungen erforscht. Verformungs- und glühinduzierte mikrostrukturelle Veränderungen beeinflussen erheblich die magnetoresistiven Eigenschaften des Materials. Diese Veränderungen wurden mit Hilfe von Lichtmikroskopie, Rasterelektronenmikroskopie, Mikrohärtemessungen und Röntgenbeugungsmessungen untersucht. Bei allen Legierungen auf Cu- und Cr-Basis wurde im verformten Zustand eine einphasige Struktur beobachtet, was auf die Bildung eines übersättigten Mischkristalls hindeutet. Cr-basierte Legierungen zeigten hingegen eine höhere Sprödigkeit, während die Ag-basierte Zusammensetzungen teilweise eine unzureichende Verformung der ferromagnetischen Phase aufwiesen. Der granulare Riesenmagnetowiderstand wurde in fast allen verformten Werkstoffen gemessen. Noch höhere Werte konnten mit einer anschließenden Wärmebehandlung des Materials erzielt werden. Der höchste Widerstandsabfall von 2.45 % wurde bei  $\text{Cu}_{60}\text{Fe}_{20}\text{Ni}_{20}$  nach einer Glühdauer von 1h bei 400°C beobachtet, wobei der Effekt bei höheren Glühtemperaturen abnimmt. Die stark plastisch verformten Werkstoffe zeigten im Allgemeinen eine bemerkenswerte Gefüge- und Phasenstabilität bei höheren Temperaturen.

## Abstract

Severe plastic deformation by high-pressure torsion was used to fabricate nanocrystalline materials in a bulk form showing the granular giant magnetoresistance effect. Immiscible binary and ternary alloys, consisting of nonmagnetic (Ag, Cu, and Cr) and ferromagnetic (Co, Fe, and Ni) elements, were investigated. The ferromagnetic content was chosen to be 20 vol% since a peak in magnetoresistance is expected to occur, and additionally to be 40 vol% for Cu- and Cr-based compositions. Microstructural changes due to deformation and annealing significantly influence the magnetoresistive properties of the material. These changes were studied using light microscopy, scanning electron microscopy, microhardness, and X-ray diffraction measurements. A single-phase structure was observed for all as-deformed Cu-based and Cr-based alloys, indicating the formation of a supersaturated solid solution. However, Cr-based alloys showed higher brittleness, whereby Ag-based compositions exhibited partially insufficient co-deformation of the ferromagnetic phase. Granular giant magnetoresistance was measured in almost all as-deformed materials and tuned in a further step with appropriate thermal treatments. Primarily, annealing had a positive effect on the magnitude of magnetoresistance. The highest drop in resistivity of 2.45 % was found in  $\text{Cu}_{60}\text{Fe}_{20}\text{Ni}_{20}$  after annealing for 1h at 400°C, whereby the effect decreases for higher annealing temperatures. Severely plastically deformed materials showed remarkable high-temperature stability of phases and microstructure.

# Content

Acknowledgments .....	I
Kurzfassung.....	II
Abstract .....	III
Content.....	IV
List of abbreviations .....	V
1. Introduction .....	1
2. Theory .....	3
2.1. Magnetoresistance .....	3
2.2. Severe plastic deformation .....	9
2.3. High-pressure torsion .....	10
3. Materials and methods .....	15
3.1. Investigated alloy systems .....	15
3.2. HPT deformation and heat treatment.....	17
3.3. Characterization of the microstructure .....	19
3.4. Magnetoresistance measurement.....	21
4. Results and discussion.....	25
4.1. Cu-based compositions.....	27
4.2. Ag-based compositions.....	42
4.3. Cr-based compositions .....	53
4.4. Discussion of the magnetoresistance .....	61
5. Summary .....	64
6. References.....	66
7. Appendix .....	70
7.1. Cu-based compositions.....	70
7.2. Ag-based compositions.....	71
7.3. Cr-based compositions .....	73

## List of abbreviations

HPT	high-pressure torsion
SPD	severe plastic deformation
SEM	scanning electron microscopy
BSE	backscattered electrons
XRD	X-ray diffraction
UFG	ultrafine-grained
NC	nanocrystalline
LM	light microscopy
RT	room temperature
EDX	energy-dispersive X-ray spectroscopy
MR	magnetoresistance
OMR	ordinary magnetoresistance
AMR	anisotropic magnetoresistance
GMR	giant magnetoresistance
CIP	current-in-plane
ARB	accumulative roll bonding
ECAP	equal channel angular pressing
BMVA	ball-milled and vacuum annealed
FWHM	full width at half maximum

# 1. Introduction

As a definition, the change of the electrical resistance of a material in an external magnetic field is called magnetoresistance (MR). Depending on the material, different MR effects can occur. About 160 years ago, the first MR effect was discovered by William Thomson in a ferromagnetic material, which is today known as anisotropic magnetoresistance (AMR) [1]. However, the AMR is a weak effect, which leads to a relative change in resistivity up to 1 % [2,3]. In 1988, Fert et al. and Grünberg et al. showed independently that the change in MR can be huge, approximately 50 %, in alternating thin layers of Cr and Fe at low temperatures, which is labeled as giant magnetoresistance (GMR) [4,5]. The GMR effect can be distinguished from the AMR effect by its isotropic behavior, i.e., the resistivity decreases for an increasing magnetic field, regardless of the orientation of the current to the applied magnetic field. The GMR effect finds its main application in magnetic field sensors, which are used in the read heads of hard disc drives or in the air- and automotive industry. Current research is being conducted on, e.g. the application of magnetoresistive random-access memories and the detection of influenza A virus by GMR biosensors [6]. In GMR biosensors, monoclonal antibodies are exchanged for a combination of viral nucleoproteins and magnetic nanoparticles. In the presence of an influenza virus, the magnetic nanoparticles can be bound to the GMR biosensor, whereby the binding rate is proportional to the concentration of the virus. A change in virus concentration results in a change in electrical resistance, which can be measured in real-time [7].

However, GMR does not only occur in alternating ferromagnetic and nonmagnetic multilayered structures. Bulk materials, which exhibit finely dispersed small ferromagnetic particles embedded in a nonmagnetic matrix can also show a GMR behavior, called granular GMR [8,9]. A disadvantage of granular materials is that the saturation of their hysteresis curve is only reached at high fields. This is due to the small size of the particles, making it difficult to saturate them. Even more, the smallest particles can be in a superparamagnetic state. As the drop in resistance is dependent on the saturation state of the material, the decreasing resistivity curve saturates also at higher fields. Regarding application, however, 3D-bulk materials show more freedom in shaping compared to 2D-multilayered materials.

The standard methods to fabricate granular alloys are melt spinning, mechanical alloying, ion implantation, and co-evaporation. Recently, it was shown that materials that have been processed by high-pressure torsion (HPT), a severe plastic deformation (SPD) technique, show also a GMR effect [10–12]. Thus, this thesis focuses on the granular GMR effect of a variety of severe plastically deformed materials. A major advantage of HPT is that nearly any material



composition can be fabricated in bulk form by deformation of the pre-compacted powder blend.

The granular GMR effect arises from spin-dependent scattering at the interfaces between ferromagnetic and nonmagnetic phases [13,14]. To obtain these interfaces, a mutual immiscibility of both phases is required. For the purpose of this thesis, ternary alloy systems, Cu-Fe-Ni, Cu-Fe-Co, Ag-Fe-Co, and Cr-Fe-Co, but also binary alloy systems, Ag-Fe and Ag-Co, were chosen. For binary alloy systems, a peak in granular GMR has been observed for a ferromagnetic volume fraction of approximately 20 % and it can be expected that this quantity does not change much when using ternary systems [15]. Consequently, volume contents close to 20 % were chosen for the ferromagnetic phase for all investigated alloy systems. For Cu-Fe-Ni and Cr-Fe-Co additionally, 40 % was chosen to be investigated. The results of Cu-Fe-Ni can be compared with available literature [16,17].

The aim of this thesis is to find suitable HPT processing conditions to build a sample composed of nonmagnetic material containing finely dispersed ferromagnetic particles. They are generated either directly, during the SPD process, or through forming a supersaturated solid solution in bulk form and, in a second the step, tune the GMR effect by segregating small ferromagnetic particles out of the supersaturated phase by appropriate subsequent heat treatments. The MR was determined by measuring the room temperature resistivity of the materials at varying magnetic fields and two different orientations of magnetic field and current. The influence of microstructural changes on the magnetoresistive behavior of the as-deformed and annealed samples was investigated by using scanning electron microscopy (SEM), X-ray diffraction (XRD), and microhardness measurements.

## 2. Theory

### 2.1. Magnetoresistance

The electrical resistivity  $\rho$ , also referred to as electrical specific resistance, describes the resistance  $R$  to current flow  $I$  in a material for a given size and geometry. For a material where the current flows through a rectangular cross-sectional area  $A$ ,  $\rho$  can be calculated according to equation (1), whereby  $U$  is the voltage, and  $L$  describes the length,  $h$  the height, and  $w$  the width of the specimen.

$$\rho = R \cdot \frac{A}{L} = \frac{U}{I} \cdot \frac{w \cdot h}{L} \quad (1)$$

For temperatures relevant for this work, the electrical resistivity of a metal is a temperature-dependent function and increases linearly with increasing temperature [18].

Furthermore, a change in resistivity is observed, when a magnetic field is applied to the conductive material. This effect is named magnetoresistance and can be defined by equation (2), where  $\rho(H)$  corresponds to the resistivity at a certain value of applied magnetic field  $H$  and  $\rho_0$  is the resistivity at  $H = 0$ . Ideally, a soft magnetic material does not show a remanent magnetization when measuring  $\rho_0$ .

$$MR = \frac{\Delta\rho}{\rho_0} = \frac{\rho(H) - \rho_0}{\rho_0} \quad (2)$$

Roughly, it can be distinguished between three material classes, leading to different magnetoresistive effects, when they are exposed to a magnetic field.

- 1.) If the material is nonmagnetic, it is referred to as ordinary MR (OMR). The OMR is characterized by its positive change in resistivity  $\Delta\rho$  with an increasing magnetic field, independent if the direction of the magnetic field is parallel or perpendicular to the current direction [19,20].
- 2.) In contrast, ferromagnetic materials show an anisotropic behavior. Therefore, their values of resistivities are dependent on the orientation between applied current and magnetic field. In parallel magnetic field direction  $\Delta\rho$  increases, whereby  $\Delta\rho$  decreases in perpendicular field direction with an increasing magnetic field. This effect is called anisotropic MR (AMR) which results only in a weak change in resistivity, typically 0.1-1 % [2,3]. As an example, ferromagnetic Ni shows such an AMR behavior, as illustrated in Figure 1. Magnetization rotation leads to a rapid change in resistivity up to approximately 4 kOe. At higher fields, the so-called forced effect is responsible for the weaker linear change in resistivity [20].

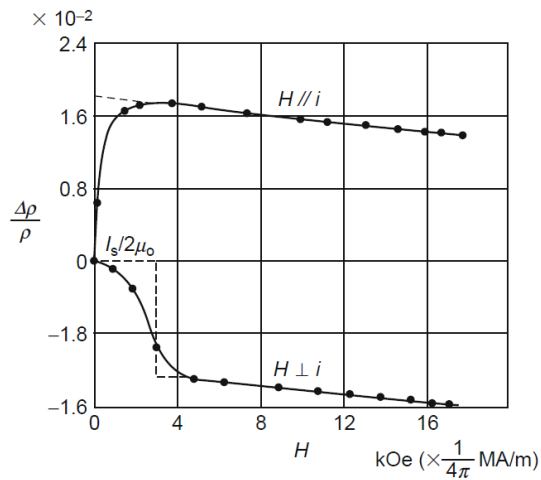


Figure 1: AMR behavior of ferromagnetic Ni exposed to a magnetic field [20].

3.) For hybrid material structures, consisting of a nonmagnetic and a magnetic material, a much larger change in resistance can occur. Depending on the structure and material combination, several different effects can be observed. These include for example the GMR effect, the tunnel MR effect, and many others. The GMR effect results in a relative change in resistivity of typically  $\sim 10\%$  but can be up to  $50\%$ . The tunnel MR can even reach values up to  $100\%$  or higher [2–5]. This thesis focuses on the GMR effect, or more precisely on the granular GMR effect. Thus, other effects resulting from hybrid materials will not be discussed here.

### 2.1.1. Giant magnetoresistance

Fert et al. and Grünberg et al. discovered independently the GMR effect more than 30 years ago. GMR occurs in multilayered materials, consisting of alternating ferromagnetic and nonmagnetic layers. A prerequisite for the appearance of the GMR effect is that the layer thicknesses must be smaller than the mean free path length of conducting electrons. Both groups chose Fe as the ferromagnetic layer and Cr as the nonmagnetic, where both layers exhibit a thickness of only a few atomic layers [4,5].

If the nonmagnetic layer between two ferromagnetic layers is thin enough, it comes to interlayer exchange coupling and adjacent ferromagnetic layers change the orientation of their magnetic spins (spontaneously) to an antiferromagnetic alignment. The alignment of the magnetization has a significant influence on the MR of the system [4,5]. At zero field, the

magnetic spins are oriented antiparallel leading to a high resistivity. With increasing field, the magnetic spins get reoriented to a parallel alignment and the resistivity decreases strongly up to the saturation field  $H_s$ . Above this value, the resistivity remains constant, because the magnetic spins of all layers are re-aligned to a ferromagnetic ordering. This GMR behavior is shown in Figure 2 (a) for a Fe/Cr multilayer measured at 4.2 K, whereby the effect becomes bigger the thinner the nonmagnetic Cr layer is [4,20].

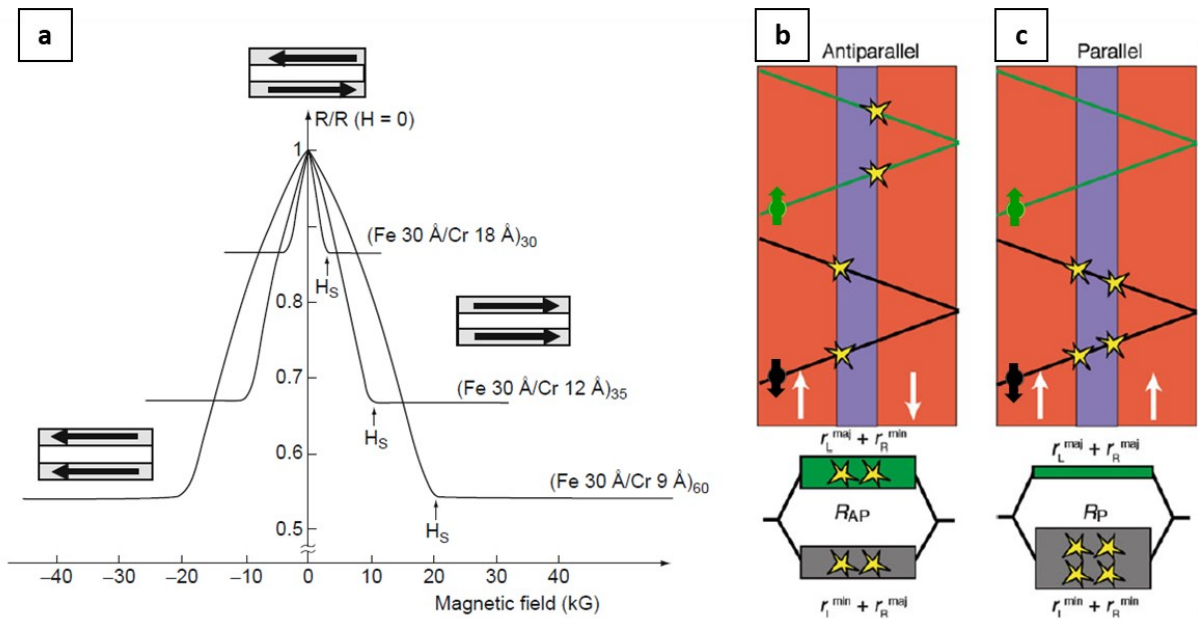


Figure 2: (a) GMR for Fe/Cr multilayers for different thicknesses of nonmagnetic Cr layers [4,20]. Simplified illustration of spin-dependent scattering in a GMR multilayer structure for (b) antiparallel and (c) parallel alignment of magnetizations (white arrows) [21].

Generally speaking, the resistivity of materials arises from scattering processes of electrons which exhibit a spin-up or spin-down. As illustrated in Figure 2 (b) and (c), electrons moving through a GMR multilayer structure are scattered at the interfaces between the ferromagnetic (orange) and nonmagnetic (purple) layers if their spin is oppositely aligned to the magnetization direction. These scattering processes are indicated by the yellow stars in Figure 2 (b) and (c) [21]. Figure 2 (b) shows an antiparallel alignment of magnetization (white arrows). Both, spin-up (green arrow) and spin-down (black arrow) electrons are scattered at that local interface where the magnetization is oppositely aligned to the electron spin. The total resistance  $R$  (or resistivity) of the system can be regarded as parallel resistors, one for each electron spin. In this case, both resistors have the same resistance, which results in high resistance. In contrast, for a parallel alignment of magnetization (see Figure 2 (c)) only the spin-down electrons are scattered. The spin-up electrons, which are oriented in magnetization

direction, pass the interfaces without spin-scattering resulting in a short circuit within the model system ( $R=0$ ). Hence, the resistance is much lower for a parallel than for an antiparallel magnetization configuration, due to less occurrence of spin-dependent interface scattering [19–21].

In contrast to the AMR effect, the GMR effect can be characterized by its isotropic MR behavior. Thus, the change in MR is negative regardless of whether the direction of the current or magnetic field is parallel or perpendicular to the layers. If the current flows parallel to the direction of the layer, we speak of a current-in-plane (CIP) geometry. The results in Figure 2 (a) were obtained for a magnetic field applied parallel to a CIP geometry. If the field is applied perpendicularly to the CIP geometry, the MR does not change significantly but saturates at higher fields than  $H_s$ . This behavior occurs because the fields have to overcome magnetic anisotropy in addition to antiferromagnetic coupling [4]. Furthermore, a higher drop in resistivity can be achieved by using a current-perpendicular-to-plane geometry [20].

### **2.1.2. Granular GMR**

However, GMR does not occur only in 2D multilayer structures, but can also be present in bulk or thin-film granular structures. This effect is referred to as granular GMR. Typically, the matrix consists of a conductive metal, Cu or Ag, in which finely dispersed small ferromagnetic particles (e.g.: Co, Fe, Ni) are embedded. The granular GMR and the corresponding magnetization curve of the sample are schematically represented in Figure 3 [6]. At zero field (or at the coercive field) the magnetization of the ferromagnetic particles exhibit a random orientation, leading to a high resistivity, resulting from spin-dependent scattering of conduction electrons at the interfaces between magnetic and nonmagnetic phases [13,14]. With increasing field, magnetic domains change gradually their alignment of magnetization towards magnetic field direction. Consequently, the resistivity decreases strongly up to the saturation field, where all magnetic domains are oriented parallel to the field.

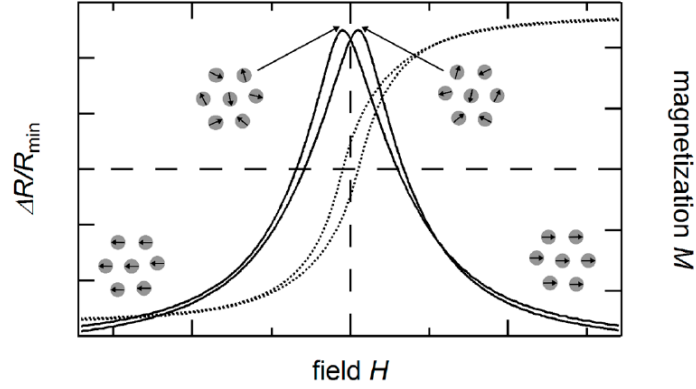


Figure 3: Granular GMR (solid line) and magnetization (dotted line) in dependency of the magnetic field [6].

It was shown that the granular GMR correlates with the squared global relative magnetization  $\mu(H)^2$  as described in equation (3).

$$GMR = \frac{\Delta\rho}{\rho_0} = \frac{\rho(H) - \rho_0}{\rho_0} = A \cdot \mu(H)^2 = A \cdot \left(\frac{M(H)}{M_S}\right)^2 \quad (3)$$

$A$  describes the ultimate size of the GMR. Its magnitude depends on spin-dependent scattering, but also on the size and volume fraction of the ferromagnetic particles.  $M(H)$  and  $M_S$  describe the magnetic field-dependent global magnetization and the saturation magnetization of the sample, respectively [8].

The magnitude of granular GMR but also the saturation field is strongly affected by the size and volume fraction of ferromagnetic particles. As illustrated in Figure 4 (a), there is a certain size for single domain ferromagnetic granules at which the GMR becomes maximum. The change of MR amplitude is determined by two competing effects that occur simultaneously. On the one hand, a decreasing particle size leads to an increase in the surface-to-volume ratio, resulting in a raise of spin-dependent scattering at the magnetic-nonmagnetic interfaces and thus to an increasing GMR. It was observed that the MR scales inversely to the average ferromagnetic particle size [9]. On the other hand, if the granule size is too small, their mutual distance falls below the mean free path of the electrons and the current can pass more easily between the granules. This causes less interface scattering and thus a decreasing GMR [22,23]. It should be mentioned that small particles are not always single domain ferromagnetic, but can also be superparamagnetic or multidomain magnetic. Depending on which particle is present, changes in particle size result in different dependencies of the granular GMR. While superparamagnetic granules show a constant increase in GMR until their saturation at very high fields, multidomain granules tend to a constant decrease in GMR for decreasing average granule size [22].

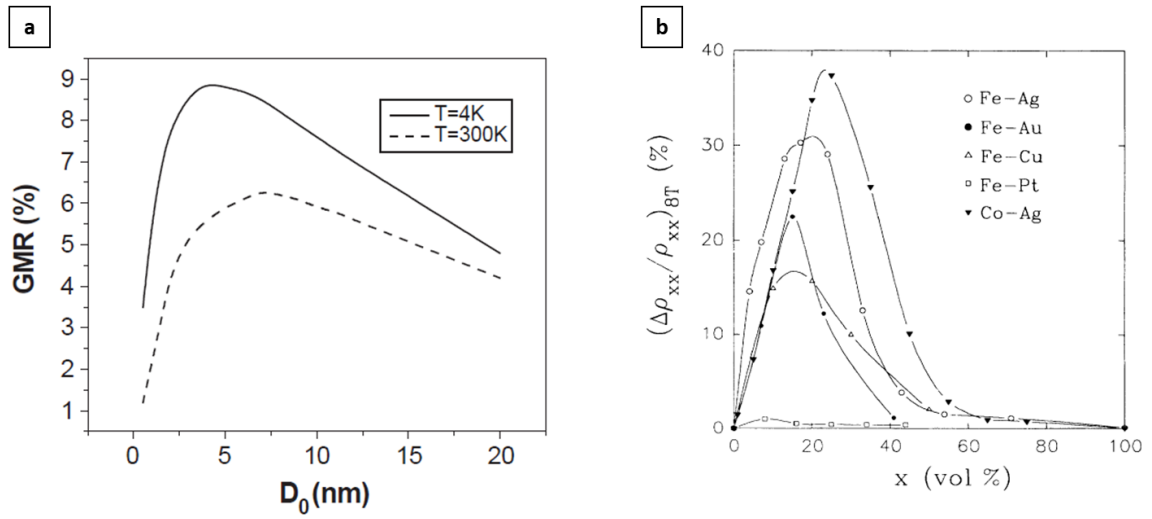


Figure 4: Schematic illustration of the granular GMR in dependency of (a) the ferromagnetic particle size [22] and (b) volume fraction [15].

The initial particle size is dependent on the used manufacturing method and material system and can be further adjusted by an appropriate subsequent annealing treatment. In general, the obtained microstructure depends on annealing parameters, such as annealing temperature, annealing time, and cooling rate. Wang et al. reported a decrease in GMR with increasing annealing temperatures (resulting in an enlargement of magnetic particles) for Fe-Ag, Fe-Cu, Fe-Au, and Co-Ag. However, higher annealing temperatures lead to a reduction in saturation fields, which is advantageous concerning sensor applications [2,15]. A further increase in GMR can be realized by lower measuring temperatures as indicated in Figure 4 (a), where the solid and dashed line represents the GMR at 4 K and 300 K, respectively [22]. For example, Berkowitz et al. measured a GMR of 10 % at 10 K in  $\text{Cu}_{81}\text{Co}_{19}$  (given in at%) at an applied field of 20 kOe. In comparison, the measured GMR at RT was negligible [9].

The ferromagnetic volume fraction dependency is similar to the granular size dependency. As shown in Figure 4 (b), a peak in granular GMR occurs at values of ferromagnetic volume fractions between 15 % and 25 %, depending on the used alloy system [15]. On the left side of the peak, i.e. with decreasing ferromagnetic contents, only a few particles are present. This leads to less spin-dependent interface scattering and therefore to decreasing GMR values. With increasing volume fractions, the granules become larger, which decreases the distance between the particles. It comes to an increase in the surface-to-volume ratio, thus a reduction in interface scattering, leading to a decreasing GMR. Above a percolation threshold of 50-60 %, only AMR is observed due to the coalescence of ferromagnetic particles to a network consisting of ferromagnetic domains [6,22].

A ferromagnetic–nonmagnetic interface is required for the occurrence of a granular GMR, which thus presumes the mutual (partial) immiscibility of both phases. Therefore, one is limited in the choice of material combinations. So far, binary alloys such as Ag-Co, Ag-Fe, Cu-Co, Cu-Fe but also ternary alloys such as Cu-FeNi, Cu-FeCo, and Ag-FeCo have been investigated [8–11,15,17,24,25]. Most of the above-mentioned alloys were processed by bottom-up techniques. For example, melt spinning, magnetron sputtering, ion beam co-sputtering, molecular beam epitaxy, electrochemical deposition, and thermal evaporation were used to produce thin films. The classical technique to create bulk materials is mechanical alloying (ball milling) [10]. However, top-down techniques, such as HPT, were barely used as a manufacturing method for GMR structures. So far, HPT was only used to produce bulk granular GMR structures of binary alloys, such as Cu-Fe and Cu-Co [10–12]. Though, no investigations were made yet to the magnetoresistive properties of ternary alloys (e.g., Cr-FeCo, Cu-FeNi, Cu-FeCo, and Ag-FeCo) processed by HPT.

## **2.2. Severe plastic deformation**

Over the past 40 years, the methods for producing ultra-fine grained (UFG) and nanocrystalline (NC) bulk materials have evolved rapidly. Basically, NC materials show typically grain sizes below 100 nm, while UFG materials are in the range of 100 nm to 1  $\mu$ m. Due to their unique microstructure, UFG and NC materials show enhanced mechanical and physical properties, leading to a wide range of possibilities regarding applications [26–30].

Bulk samples with a structure in the UFG or even NC regime can be fabricated by using “bottom-up” or “top-down” approaches. For example, “bottom-up” techniques involve inert gas condensation, electrodeposition, and chemical and physical vapor deposition. In this process, larger structures are built from smaller basic units, e.g., of individual atoms. In the “top-down” approach, a NC structure can be generated by a significant grain refinement of an existing coarse-grained bulk material. Such a substantial grain refinement of a bulk material can be easily induced by SPD, which is one of the most often used “top-down” approaches [26]. Thereby, the bulk material is exposed simultaneously to high hydrostatic pressure and large strains (true strains  $\geq 10$ ) without a significant change of sample dimensions and shape. The most used SPD techniques for producing fine-grained alloys are accumulative roll bonding (ARB), equal channel angular pressing (ECAP), and HPT [31,32].



### 2.3. High-pressure torsion

Figure 5 (a) shows a schematic illustration of the HPT setup nowadays usually used. Therein, two cylindrical anvils are arranged concentrically to each other. To enable precise torsional straining, the sample must be positioned centrally between the anvils. For that purpose, each anvil has a cylindrical, slightly conical cavity in its center. The disc-shaped specimen (Figure 5 (b)) is placed between the cavities, whereby the anvil cavity diameter corresponds to the sample diameter. Furthermore, the cavities fulfill a second important purpose. When the sum of the cavity depths is somewhat smaller than the initial HPT sample thickness, a small amount of the material can flow in the slit between the anvils when pressure is applied. The friction between material and anvils (outside the processing zone) leads to confinement of material flow. Consequently, the backpressure induces a hydrostatic pressure within the processing zone. In addition, the material in this gap prevents contact between the anvils, which would lead to their failure during processing [28,32,33].

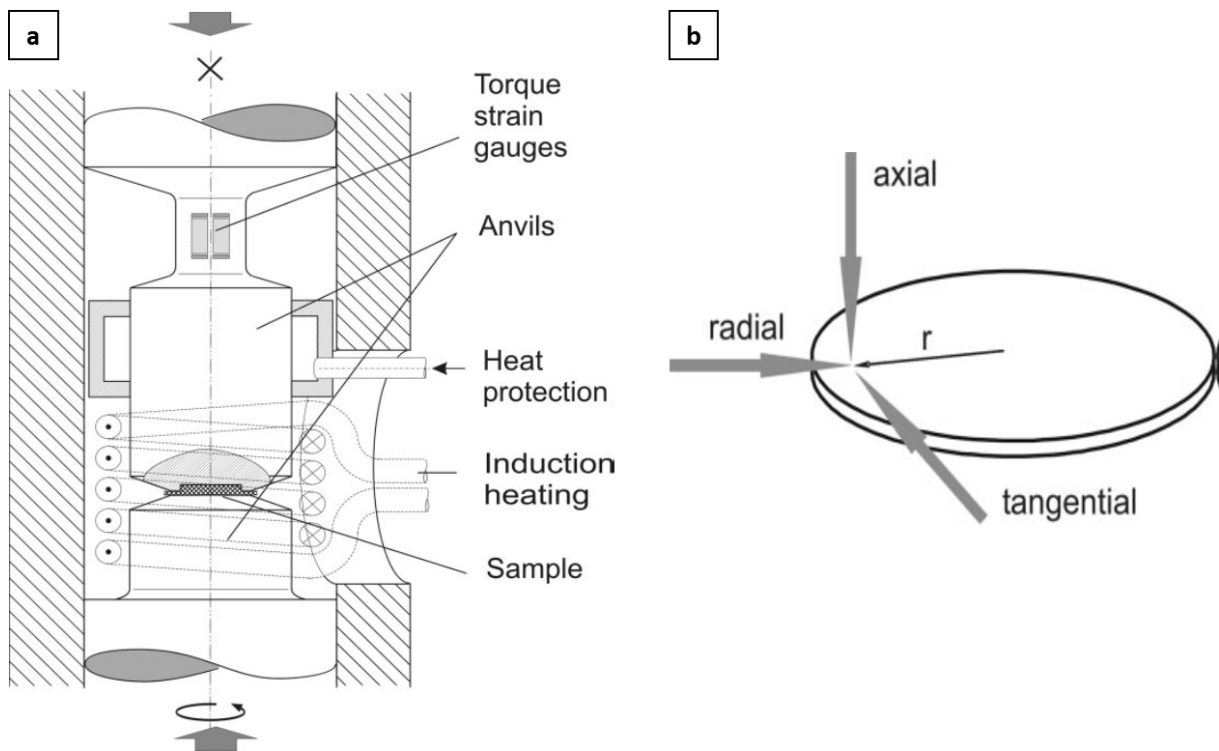


Figure 5: Schematic illustration of (a) the HPT setup and (b) disc-shaped HPT specimen showing different observation directions [33].

After applying load on the anvils, they are rotated against each other, whereby one of them is fixed. To accomplish continuous plastic deformation, sliding of the sample between the anvils has to be prevented. Thus, sufficient friction between the sample surfaces and the anvil surfaces is necessary. For this purpose, the micro-roughness can be increased by sandblasting

the anvil cavities and the sample surfaces on the one hand. On the other hand, an increase in applied pressure leads to higher friction forces. Furthermore, a minimum pressure, at least equal to the yield stress of the material, is necessary to achieve material flow. As a rule of thumb, the minimum pressure (several GPa) should be approximately three times the yield stress of the undeformed material. As an upper limit, the applied pressure should not exceed three times the yield stress of the anvils. Besides the pressure, other processing parameters can be adjusted for the HPT deformation process, like the temperature, strain rate, and strain path (cyclic or monotonic). A change of the processing parameters affects the obtained microstructure, which generally can be observed in the axial, tangential, and radial HPT sample direction, as illustrated in Figure 5 (b) [32,33]. Furthermore, the composition of the starting material has a strong influence on the resulting microstructure of the as-deformed material [34]. The influence of these parameters on the microstructural evolution will be discussed later in Chapter 2.3.1.

Basically, the ideal HPT process can be considered as a shear process, due to the predominant hydrostatic pressure. The shear strain  $\gamma$  can be determined according to equation (4) assuming a constant sample thickness  $t$ .

$$\gamma = \frac{2\pi \cdot r}{t} \cdot n \quad (4)$$

In equation (4),  $n$  is the number of turns and  $r$  denotes the radius of the HPT sample. Moreover, to enable a comparison of the strain with other deformation processes, e.g. a tensile test, the von Mises equivalent strain  $\varepsilon$  can be calculated according to equation (5):

$$\varepsilon = \frac{\gamma}{\sqrt{3}} \quad (5)$$

In the ideal torsion deformation process, the shear strain exhibits a linear dependence on the radius, i.e., should be zero in the center and highest at the edge of the disc-shaped sample. However, the sample thickness decreases in the real HPT process due to material flow. As long as the thickness-to-diameter ratio does not exceed 0.1, equations (4) and (5) are applicable for real HPT processes. Basically, the compression deformation (usually 10%) is often negligibly small compared to the high imposed shear strains. It should be noted that the above-mentioned equations are not valid near the edge of the specimen, due to the small

sample thickness and the barely defined sample shape. For example, a deformation of a sample with a thickness of 0.6 mm by 100 turns corresponds to an equivalent strain of 1800 at  $r = 3$  mm. Such high values of shear strains cannot be reached with other SPD techniques, e.g., ARB or ECAP. In addition, it is possible to adjust the shear strain precisely at a particular radius by changing the number of turns. Due to the high hydrostatic pressure, it is even feasible to deform brittle or high-strength materials far below RT, whereby the hydrostatic pressure may counteract crack formation during SPD. The processing temperature can be adjusted between  $-195^{\circ}\text{C}$  and  $500^{\circ}\text{C}$  by using liquid nitrogen for cooling and an induction coil for heating the anvils, respectively. Nevertheless, the HPT technique exhibits also disadvantages. The resulting sample size is limited, keeping it from many applications. In the last decades, HPT devices were further developed. An upscaling of sample size is possible by using bigger anvils, which also require higher forces and torques for deformation [28,32,33].

### **2.3.1. Influence of HPT processing parameters on microstructural evolution**

For both, single-phase and multiphase materials, an increasing shear strain leads to decreasing grain size. However, saturation in grain size occurs above a critical shear strain value. This grain refinement saturation behavior is schematically shown in Figure 6 [33]. The initial grain refinement of severe plastically deformed single-phase materials arises from dislocation rearrangement. With increasing shear strain, dislocations pile up at grain boundaries, leading to a drastic rise of dislocation density. Within the initial grains, the dislocations arrange themselves to sub-grain boundaries and the grains are subdivided into cells with smaller and larger misorientations. The sizes of these cells decrease with evolving strain and the misorientation of the neighboring cells becomes higher, leading partially to a transition of low-angle grain boundaries to high-angle grain boundaries. Above a critical strain, the refinement process reaches saturation. The initial grain boundaries vanish and sub-grain boundaries transform to high-angle grain boundaries, finally resulting in a uniform microstructure [28,33].

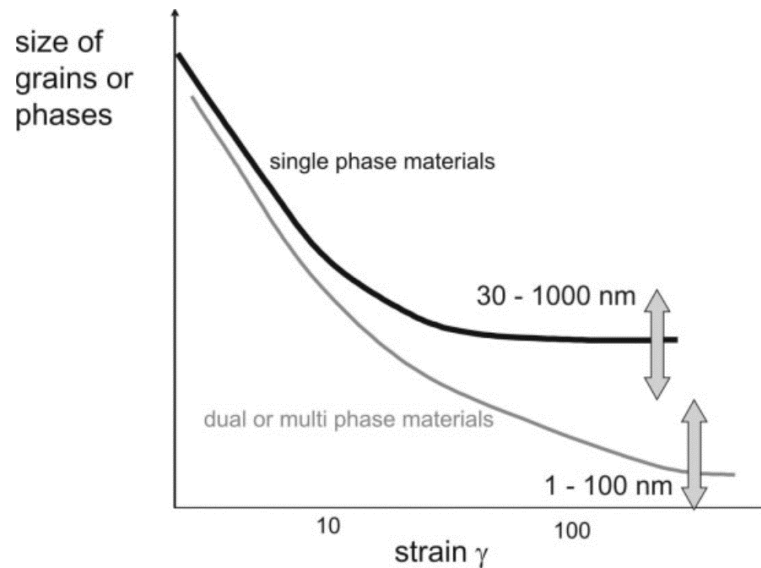


Figure 6: Schematic illustration of the structural refinement of single- and dual- or multiphase materials as a function of applied shear strain [33].

At the saturation shear strain, the grain size reaches its minimum and remains constant for single-phase materials, independent of the initial grain size. During SPD, a coarse-grained microstructure refines, while a finer NC microstructure coarsens until the saturation grain size is reached. The flow stress, and therefore the microhardness, correlates with the crystallite size of a material. Basically, the hardness exhibits a radial dependency and does not change significantly in the axial direction. Thus, by using microhardness measurements, the radial position where the saturation grain size occurs can be easily determined [32], which will be shown later in chapter 3.3 in Figure 8.

The saturation grain size of single-phase materials is mainly affected by alloying, deformation temperature, and strain path, but is only slightly dependent on applied pressure and strain rate at lower temperatures. However, the influence of the strain rate on the saturation grain size becomes more relevant at elevated deformation temperatures. Basically, the crystallite size increases because of increasing grain boundary migration and triple junction motion with increasing deformation temperatures. Temperature-induced diffusion processes and shear deformation work against each other during HPT. Regarding the strain path, monotonic shearing of the material leads to a finer microstructure compared to cyclic shearing [28,33,35].

Furthermore, the saturation grain size depends on the number of existing phases. As indicated in Figure 6, dual or multiphase materials can achieve a smaller saturation grain size than single-phase materials, though requiring higher strains. It should be mentioned that alloying does not necessarily result in a multiphase material, a single-phase material can also be obtained. An additional benefit of HPT is that bulk samples with a well-defined composition can be

produced out of any material combination by HPT compaction and deformation of blended elemental powders. Basically, dual-phase materials show a more complex deformation behavior than single-phase materials, depending on the chosen alloy system, the hardness difference, and the volume fraction of constituent phases [34].

As a definition, composite materials have two or more distinct constituents or phases. Moreover, in a real composite, the physical and chemical properties of the constituent phases must differ noticeably from the properties of the components. Classical examples are particle- or fiber-reinforced metal-matrix composites, e.g. WC. However, an alloy exhibiting a two-phase microstructure, obtained by solidification out of the melt or by subsequent heat treatment of a solid, is usually not classified as a real composite [31,36]. Nevertheless, composites and alloys will be treated as the same in this thesis, due to their same behavior.

For example, in a metal-metal matrix either a nanocomposite can be formed by fragmentation processes (e.g. W-Cu) or supersaturated solid solutions by the dissolution of one phase (e.g. Fe-Cu), even if the mutual solubility of the solid phases is vanishingly low at RT and equilibrium conditions. Another deformation behavior is observed during SPD of a metal-nonmetal matrix (e.g. SiC-Al6061). Therein, it comes to a homogenization of the particle distribution (SiC) in the metal matrix. Generally, the limitation in grain refinement during SPD of dual-phase materials can be explained by pinning of grain boundaries by a fine second phase, hindering them in their migration. This leads to a stabilization of a finer microstructure compared to single-phase materials and even to enhanced thermal stability [28,31,33,34].

### 3. Materials and methods

#### 3.1. Investigated alloy systems

In this thesis, different alloy systems were investigated, which are expected to show the granular GMR effect. For this purpose, an interface of a ferromagnetic and nonmagnetic phase is necessary. Therefore, the chosen alloys should show a pronounced miscibility gap of both phases. For the magnetic phase, Fe, Co, Fe-Co, or Fe-Ni have been chosen and for the nonmagnetic phase, Ag, Cr, or Cu. Mainly ternary, but also binary alloy systems were examined. For better classification, the alloy systems are divided by their nonmagnetic phase. We distinguish between Ag-based, Cu-based, and Cr-based alloys. The ferromagnetic volume fraction was chosen to be 20 vol-% for all compositions, for CuFeNi and CrFeCo in addition 40 vol-%. The investigated alloys with their compositions in weight percentage are listed in Table 1.

Table 1: Elemental compositions of the three investigated alloy systems with the corresponding HPT deformation process parameters.

Nominal Composition	Pressure	Deformation Temperature	Rotational Speed	Number of Turns
wt-%	GPa	°C	1/min	-
Ag <sub>83</sub> Co <sub>17</sub>	5	RT	1.28	100
Ag <sub>84</sub> Fe <sub>16</sub>	5	RT	1.28	100
Ag <sub>84</sub> Fe <sub>12</sub> Co <sub>4</sub>	5	RT	1.28	100
	5	300	1.28	100
Cu <sub>82</sub> Fe <sub>12</sub> Co <sub>6</sub>	5	RT	1.28	100
Cu <sub>80</sub> Fe <sub>10</sub> Ni <sub>10</sub>	5	RT	1.28	100
Cu <sub>60</sub> Fe <sub>20</sub> Ni <sub>20</sub>	5	RT	1.28	100
Cr <sub>78</sub> Fe <sub>16</sub> Co <sub>6</sub>	7.5	RT	0.63	4; 8
	7.5	400	0.63	2
Cr <sub>64</sub> Fe <sub>27</sub> Co <sub>9</sub>	7.5	RT	0.63	10; 20
	7.5	400	0.63	1; 2; 5

The Ag-based and Cu-based compositions were produced by the powder route. In the first step, the pure elemental metal powders were mixed to the desired composition in a glove box. This glove box is filled with an Ar atmosphere to prevent contamination and oxidation of the metal powders. The elemental powders used for the powder route are listed in Table 2. In the second step, the powder blends of each composition were pre-compacted hydrostatically in Ar atmosphere to obtain a bulk sample. For this purpose, a Cu-ring (2.5 mm height and 10 mm diameter) was placed concentrically in the cavity (0.3 mm depth and 8 mm diameter) of an HPT steel anvil. The powder mixture was filled in this hollow space, then hydrostatically pressed and torqued by the second anvil of the HPT setup. For the HPT pre-compaction process, a pressure of 5 GPa and a rotational speed of 0.2 rpm was applied for 20 s at room temperature (RT) on each powder mixture. The obtained disc-shaped sample exhibits typically a height of about 1 mm and a diameter of 8 mm.

Table 2: Elemental powder materials for the powder route.

Powder Material	Purity/%	Manufacturer	Particle Size/ $\mu\text{m}$	Mesh
Ag	99.9	Alfa Aesar	<25	-500
Co	99.998	Alfa Aesar Puratronic	<30	-22
Cu	99.9	Alfa Aesar	37-88	170+400
Fe	99.9	MaTeck	74-149	-100+200
Ni	99.9	Alfa Aesar	3-7	-3+6

As will be shown later, the harder Co and Fe particles did not properly co-deform in the softer Ag-matrix during the HPT deformation process. To enhance the co-deformability and thus the refinement of the ferromagnetic phase in Ag-Fe and Ag-Fe-Co during the HPT process, the initial elemental powders were heat treated or ball-milled before the HPT pre-compaction process. The idea behind this additional processing step was to harden the soft Ag powder by ball milling and to soften the harder Co and Fe powder by annealing, respectively. For that purpose, the Co and the Fe powder were exposed to a vacuum annealing for 1h at 650°C with a subsequent furnace cooling in a vacuum furnace by Xerion. The Ag powder was ball-milled in an Ar atmosphere for 1h at low energy (100 rpm). The ball-milling treatment was performed in a Retsch Planetary Ball Mill PM400. The grinding ball to powder ratio was 10:1, whereby 20 g bigger and 80 g smaller steel balls were used. This powder pre-treatment of ball milling (of Ag) and vacuum annealing (of Fe and FeCo) is abbreviated with BMVA. To compare the

evolution of the microstructure and particle morphology of the powders, XRD and SEM have been carried out before and after the ball milling process.

The Cr-based alloys were fabricated by the arc melting route to enhance the subsequent HPT deformation processability [37]. Again, the elemental materials (Cr-granules, Co-granules, and Fe-flakes) were mixed in an Ar atmosphere to the desired composition (see Table 1). The data of the used starting materials can be found in Table 3. The arc melting process of the granule composition took place in an AM200 device Edmund Buehler GmbH, whereby the ingot was turned and five times remelted in an Ar atmosphere. To receive the same initial sample geometry as in the powder route, cylinders with a diameter of 8 mm were cut out of the arc melted CrFeCo- ingot by electro-discharge machining. Before HPT deformation, the cylinders were cut into discs with a height of about 1 mm.

Table 3: Elemental materials for the arc melting route.

Material	Shape	Purity/%	Manufacturer	Particle Size/mm
Co	Granules	99,99	HMW Hauner GmbH & Co. KG	<20
Cr	Granules	99,8	HMW Hauner GmbH & Co. KG	1-4
Fe	Flakes	99,99	HMW Hauner GmbH & Co. KG	<20

### 3.2. HPT deformation and heat treatment

For the granular GMR effect, a nonmagnetic matrix with finely dispersed ferromagnetic particles is necessary. For that purpose, all bulk samples produced by the arc melting route and the powder route, respectively, were severely deformed by HPT. Due to the high applied strain, it is possible to form supersaturated solid solutions or nanocomposites with a grain size in the UFG or even in the NC regime. Table 1 shows the HPT processing parameters, such as the applied pressure, deformation temperature, rotational speed, and the number of turns of the respective nominal composition. Due to the high brittleness of the Cr-based alloys, various combinations of deformation temperatures and number of turns were performed with the goal to obtain a crack-free specimen. For HPT at RT, the anvils were air-cooled to prevent sample heating. Basically, a cavity height of 0.2 mm and a diameter of 8 mm were chosen for each anvil of a set. After deformation, disc-shaped specimens with a diameter of 8 mm and heights between 0.40-0.60 mm were obtained.



After deformation, the obtained bulk specimens were cut in half by a water-cooled diamond wire saw. One of these two halves was subsequently annealed. The subsequent heat treatment aimed to reach fine precipitation of the ferromagnetic phase out of the supersaturated solution. Thus, by comparing the two disc-halves, the influence of the annealing parameters on the microstructural evolution and magnetoresistive behavior can be investigated. In general, all heat treatments were performed according to the same scheme. First, the half samples were annealed at a specific temperature for a certain time (see Table 4) in air (except the ones marked with an asterisk) and then subsequently quenched in water. For Cu-based alloys, several heat treatments were performed. For this purpose, the as-deformed samples were cut as schematically shown in Figure 7 (c) to receive three instead of two MR samples from one HPT disc. The blue shaded areas represent thereby the MR samples. One of the MR samples stays in the as-deformed state acting as a reference sample, the other two were subsequently annealed. When annealing an MR sample, the outer segment of the disc was also annealed for further microstructural investigations. To prevent a high mass loss by oxidation at elevated annealing time-temperature ratios (60|600 min|°C and 6000|400 min|°C), these  $\text{Cu}_{60}\text{Fe}_{20}\text{Ni}_{20}$  specimens were inserted in a glass capsule filled with Ar before annealing.

Table 4: Annealing duration and temperature carried out for the given nominal compositions. The specimens marked with an asterisk were encapsulated in a glass tube filled with Ar.

Nominal Composition		Time   Temperature						
wt-%		min   °C						
$\text{Ag}_{83}\text{Co}_{17}$	-	-	-	-	-	-	-	-
$\text{Ag}_{84}\text{Fe}_{16}$	-	-	60 400	-	-	-	-	-
$\text{Ag}_{84}\text{Fe}_{12}\text{Co}_4$	-	-	60 400	-	-	-	-	-
$\text{Cu}_{82}\text{Fe}_{12}\text{Co}_6$	-	-	60 400	-	10 500	-	-	-
$\text{Cu}_{80}\text{Fe}_{10}\text{Ni}_{10}$	-	-	60 400	-	10 500	-	-	-
$\text{Cu}_{60}\text{Fe}_{20}\text{Ni}_{20}$	60 300	10 400	60 400	6000 400*	10 500	-	10 600	60 600*
$\text{Cr}_{78}\text{Fe}_{16}\text{Co}_6$	-	-	-	-	-	60 520	-	-
$\text{Cr}_{64}\text{Fe}_{27}\text{Co}_9$	-	-	-	-	-	60 520	-	-

### 3.3. Characterization of the microstructure

For better handling, the as-deformed and annealed specimen halves were embedded in resin or clamped in metal holders. Initial examinations of the microstructure were carried out by an Olympus BX51 optical light microscope (LM). However, the LM was only used for overview images, because its resolution is not sufficient to capture the NC structure of the specimen. Therefore, a SEM was used, which enables a much higher resolution. Both, LM and SEM image acquisition, were conducted in the tangential sample direction, which is schematically shown in Figure 7 (a).

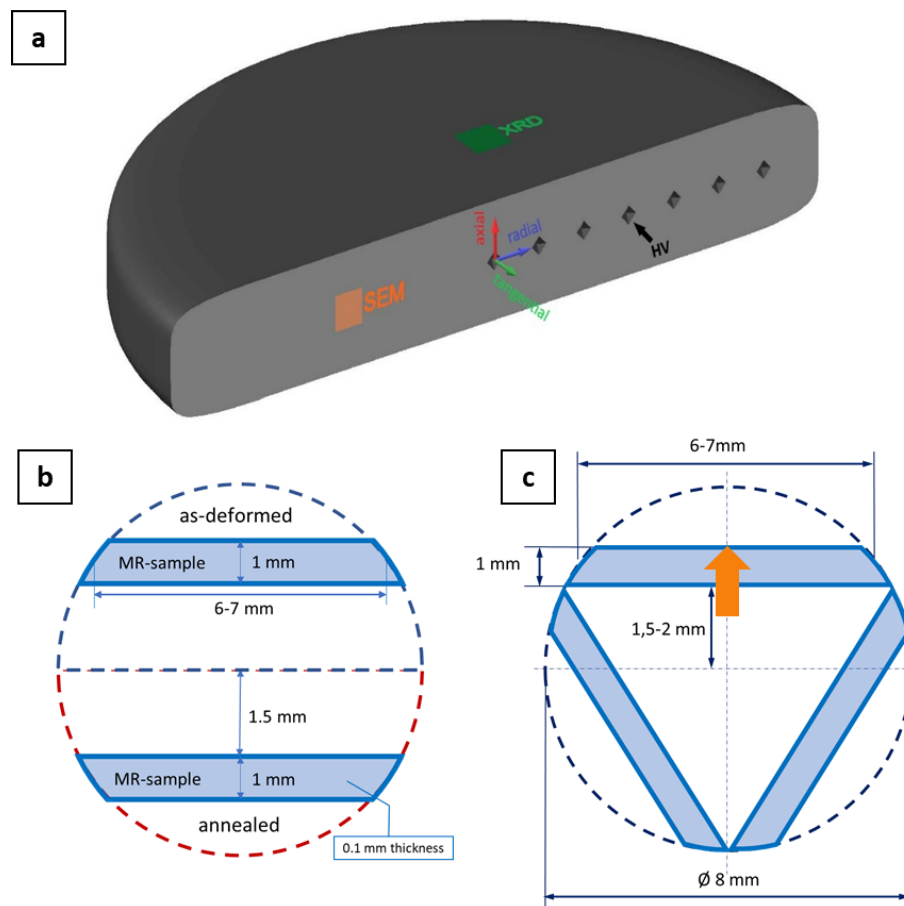


Figure 7: Schematic illustration of the positions, where (a) measurements for microstructural characterization were carried out at a half HPT disc and (b) MR samples were cut out of a half HPT disc. (c) Optimization of the maximum number of MR samples (blue shaded), which can be cut out of a whole HPT disc. The orange arrow indicates the direction and position where SEM micrographs were taken at the annealed disc segments.

LM images were taken of the whole sample cross-section. For the SEM micrograph acquisition, a Zeiss Leo 1525 SEM was used and an acceleration voltage of 20 kV and an aperture size of 60  $\mu\text{m}$  were adjusted. To correlate the observed microstructure to the applied strain, sets of micrographs were acquired along the radial direction. They were taken in 1 mm increments from radius 0-3 mm at the half sample height using a backscattered electron (BSE) detector. In the case of annealed MR samples, the outer segment of the disc was investigated (see Figure 7 (c)). Thereby, micrographs were only taken in the radial direction at the center of the cross-section (orange arrow). The cross-section center of each disc segment corresponds to a radius of about 2.5-3 mm.

To examine the actual occurring chemical composition, energy-dispersive X-ray spectroscopy (EDX) was performed using a Bruker XFlash 6|60 device for all as-deformed samples at a radius of 3 mm. For samples with a homogeneous microstructure, the composition (expressed in weight percentage) was averaged from 30 measuring points. In the case of an inhomogeneous microstructure, the composition was averaged from the measured area.

To investigate the constituting crystallographic phases after HPT deformation and subsequent annealing treatments, XRD measurements were carried out using a BRUKER D2 Phaser. The sample was radiated in the axial sample direction (see Figure 7 (a)) with a Co -  $K\alpha$  source, which produces photons with a wavelength of  $\lambda = 0.178897$  nm. The 1D detector measured the XRD pattern in a range of  $45^\circ \leq 2\theta \leq 105^\circ$ , whereby  $\theta$  is the Bragg-angle. For enhanced statistical recording, the sample was rotated with a rotational speed of 15 rpm and measured with 1485 steps and 5 seconds per step. XRD measurements were carried out on half HPT discs and in addition directly on the MR samples. To reduce background radiation, the polymer substrate was replaced by a single-crystalline Si substrate and the MR samples were fixed with petroleum jelly instead of plasticine.

To verify, at which radius the grain refinement reaches a steady-state, microhardness measurements were carried out in the tangential direction along the sample radii by using a Buehler Micromet 5102. A constant load of 200 g, 300 g, or 500 g was applied to the Vickers indenter for the Ag-, Cu-, and Cr-based samples, respectively. The indents were performed in increments of 0.25 mm starting at the middle position of the sample up to a radius of 3.5 mm. This is shown schematically in Figure 7 (a). Furthermore, microhardness values were used to determine, at which position the MR samples had to be cut out of the HPT disc as the MR sample has to be taken from a region where microstructural saturation is reached. A steady-state of hardness values occurs above a radius of 1 mm for all as-deformed samples as schematically indicated in Figure 8 for as-deformed  $\text{Cu}_{82}\text{Fe}_{12}\text{Co}_6$ . The shear strain values in Figure 8 were calculated according to equation (4) with a constant sample thickness of 0.33 mm after deformation of 100 turns at RT.

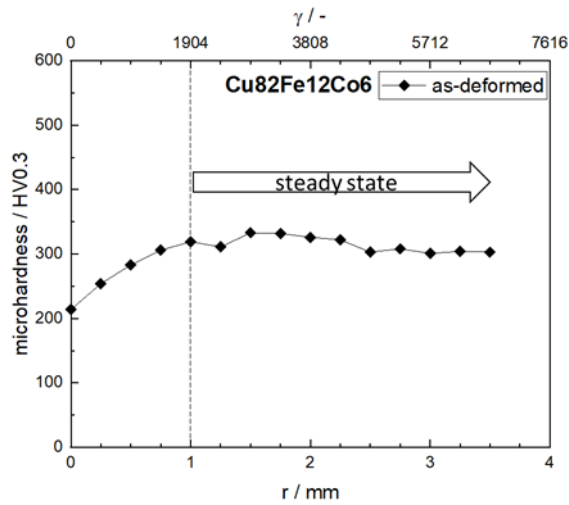


Figure 8: Steady-state of microhardness values of as-deformed  $\text{Cu}_{82}\text{Fe}_{12}\text{Co}_6$  as a function of the sample radius  $r$  and consequently of the shear strain  $\gamma$ .

Therefore, to ensure a homogeneous deformed microstructure, the distance of the extracted MR specimen is 1.5 mm or more from the center of the HPT specimen (see Figure 7 (b) and (c)).

### 3.4. Magneto-resistance measurement

This master thesis aims to produce bulk material alloys by HPT deformation, which exhibit the granular GMR effect. For resistivity measurements, a long and thin specimen is necessary, which exhibits a homogeneously deformed microstructure with small ferromagnetic particles. As above mentioned, a saturation of hardness values occurs above a radius of 1.5 mm. This indicates that the microstructure does not change above this radius. However, the size of the existing MR measurement setup is limited, which requires a minimum sample length of about 6 mm and a width of about 1 mm. To reach such a sample size and to accomplish a homogeneous microstructure, MR samples were cut out either at a distance of 1.5 mm parallel to the center cross-section axis of the as-deformed and annealed disc halves (see Figure 7 (b)) or inclined at an angle of  $60^\circ$  (see Figure 7 (c)) to maximize the number of MR samples. Using the first method, a mean length of 6.9 mm can be reached, which is enough to fix the sample in the dedicated sample holder. After cutting, thinning of the sample in the axial direction is necessary to ensure a large voltage drop, yielding a better quality of the magneto-resistive results.

The specimen is mechanically ground from both sides until the sample thickness reaches approximately 100  $\mu\text{m}$ . This ensures furthermore that the oxide layer possibly formed on the annealed samples is removed and that all MR samples exhibit the same geometry of about  $7 \times 1 \times 0.1 \text{ mm}^3$  (length x height x thickness).

In the case of  $\text{Cu}_{60}\text{Fe}_{20}\text{Ni}_{20}$ , several heat treatments were carried out. To achieve more MR samples from one as-deformed HPT sample, the HPT disc was cut as shown in Figure 7 (c). Two of the three obtained samples were exposed to a heat treatment. The third one was left in the as-deformed state to have a comparison to all annealed samples. Furthermore, it is possible to check whether the MR measurement is consistent for different as-deformed specimens of the same composition and the same HPT processing parameters.

The magnetic field-dependent resistivity of the investigated materials was determined using a Bruker B-E 30 electromagnet. This magnet has two concentric pole pieces with a diameter of 176 mm, which are separated by a 50 mm air gap (see Figure 9 (f)). In this gap, the MR measurement setup is placed. The used electromagnet can be supplied with a maximal current of 200 A, which corresponds to a magnetic field of about 22.5 kOe. The magnetic field values, which are dependent on the applied current, were measured by a Lakeshore Model 475 DSP Gaussmeter. It is necessary to note that the saturation field of most materials occurs at much higher fields or for the achievable field at much lower temperatures. Stücker et. al showed that small Fe particles in as-deformed Fe-Cu, which would be also necessary for an enhanced granular GMR effect, do not saturate magnetically, even at an applied field of 70 kOe at 300 K [38]. Therefore, the given GMR values in this thesis refer to the maximum field of 22.5 kOe and not to the saturation field. The electromagnet power supply by Bruker B-MN 170/200R was water-cooled by a Bruker B-MT 15/40 heat exchanger to prevent overheating. The actuated electromagnet was controlled automatically by a provided SciLab script. In this script current values of 0, 10, 20, 30, 40, 50, 60, 80, 100, 120, 160, 200 A were set for magnetization, and the same values backward for demagnetization of the sample. The current values were chosen to receive about evenly distributed magnetic fields from 0 kOe to 22.5 kOe. For data evaluation, only the magnetic fields were considered which correspond to the current values for increasing magnetization. In addition, the SciLab script was also used for data recording of the current applied to the MR sample and the voltage drop.

Before starting the measurement, the MR sample was attached to a MR measurement setup (four-point probe method) designed by Mirjam Spuller (see Figure 9 (c)-(f)). The MR sample is positioned above the holes (where the pins for voltage measurement are located) and then fixed to the specimen stage with the Cu-blocks (for current supply) as shown in Figure 9 (d). Thus, these pins are movable in the vertical direction due to springs.

The red arrow indicates the direction of the current, which is applied to the specimen via the Cu-blocks. Basically, a direct current of maximum 1 A was applied by a KEITHLEY model 2400 source meter. The set current depends on the specific resistance and the geometry of the sample. Thus, before applying a magnetic field, for each sample, the current was adjusted until a voltage drop of about 5 mV was reached between the measuring pins. Using the maximum current for low conducting samples might lead to undesired heating of the MR sample. After fixing, a sample counter hold tool is positioned between the Cu-blocks, as shown in Figure 9 (e). Then, the counter hold tool together with the sample stage is brought down with a locking screw until the voltage needles have sufficient contact with the sample. The counter hold tool prevents bending of the thin MR samples, thus providing constant contact between pins and sample. After attaching the sample, the MR measurement setup was placed between the pole pieces. To probe the isotropic magnetoresistive behavior, the setup must be rotated until the current direction of the sample is either perpendicular or parallel to the magnetic field as shown in Figure 9 (a) and (b).

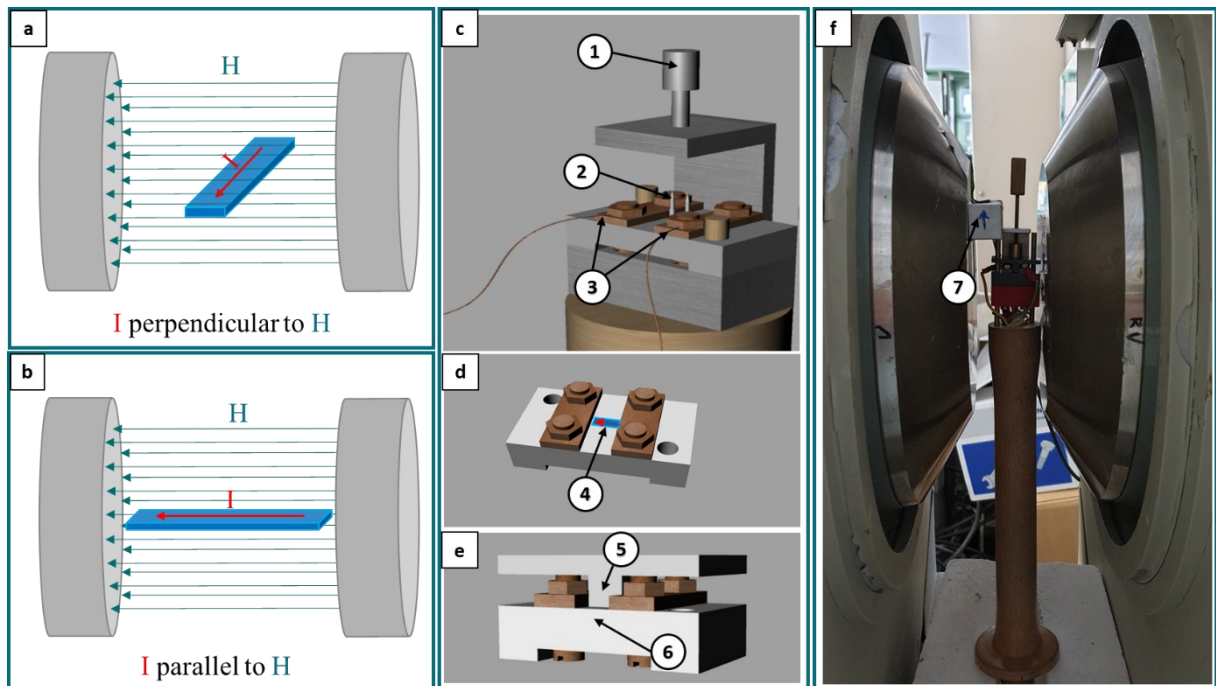


Figure 9: (a)-(b) Schematic illustration of the orientation of current  $I$  (red arrow) and magnetic field  $H$  (green arrows). (c)-(e) Schematic representation of the MR measurement setup: (1) locking screw (2) movable pins for voltage measurement (3) Cu-blocks for fixing the MR sample and applying current on the sample (4) MR sample clamped between sample table and Cu-blocks (5) sample counter hold tool (6) sample table. (f): MR measurement setup between conical pole pieces. (7) encapsulated Hall-probe.

To determine the GMR behavior, two measurements must be performed. First, the long side of the sample (and thus the current) was aligned perpendicular, and second, parallel to the magnetic field, as schematically shown in Figure 9 (a) and (b), respectively. The essential part of the measurement is the determination of the voltage changes with an increasing magnetic field. Voltage drops are recorded using a Keithley model 2000 multimeter. The values of the resistivity are calculated according to equation (1), whereby the length of the specimen  $L$  is replaced by the distance between the pins for voltage measurement. In this measurement setup, the pins have a constant distance of 3.1 mm. The GMR data, which are displayed in the results chapter, are calculated according to equation (3)

## 4. Results and discussion

In this chapter, the results of the investigated Cu-, Ag-, and Cr-based compositions are presented. To avoid confusion, the compositions herein are referred to as nominal compositions and not actual compositions. The actual occurring composition was measured in each case at  $r = 3$  mm using EDX. In general, the microstructure was investigated by using LM and SEM. LM was used for overview images of the HPT sample cross-section in the tangential direction. These images can be found in the appendix. SEM was used in BSE-mode to investigate the microstructure of the as-deformed and subsequent annealed samples in the tangential direction along the radii in more detail. The here shown as-deformed Cu-, Ag-, and Cr-based compositions were deformed with 100 turns at RT and the respective SEM micrographs were acquired in tangential direction at  $r = 3$  mm in BSE mode unless otherwise stated.

A reference measurement was carried out to validate the measurement accuracy of the MR setup. The reference measurement was conducted on a severely deformed tungsten sheet (25  $\mu\text{m}$  thickness) using the same parameters as for the later measured HPT samples. As shown in Figure 10, tungsten exhibits a constant electrical resistivity with an increasing field for both orientations of  $I$  to  $H$ .

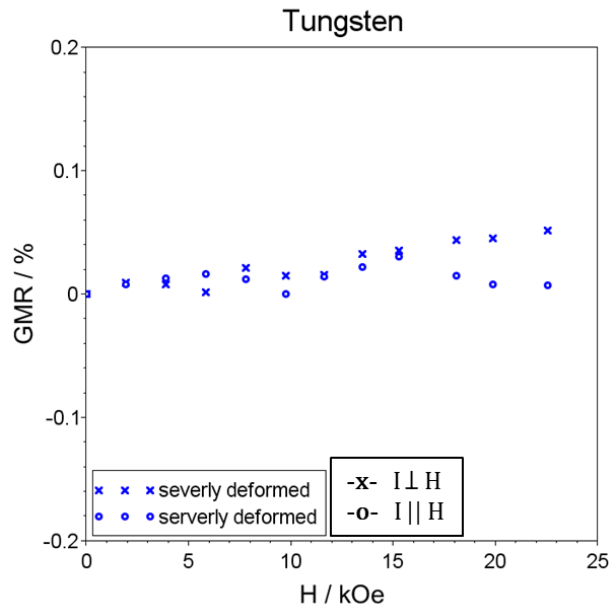


Figure 10: Change in electrical resistivity in dependency of the applied magnetic field of a severely deformed tungsten sheet.



Basically, in all GMR diagrams in this thesis, a perpendicular orientation is indicated with crosses and a parallel orientation with circles as data points. As was to be expected, pure tungsten does not exhibit a GMR behavior, due to its paramagnetic properties. Furthermore, a value of electrical resistivity of  $0.067 \Omega \text{ m}^2 \text{ m}^{-1}$  was obtained for tungsten at  $H = 0$  for both field directions at RT. This value is in good accordance with the literature values, which are in the range of  $0.059 \Omega \text{ m}^2 \text{ m}^{-1}$  to  $0.083 \Omega \text{ m}^2 \text{ m}^{-1}$  at  $20^\circ\text{C}$  [39]. Therefore, it can be assumed that the measured resistivity values and consequently also the evaluated GMR values are valid.

## 4.1. Cu-based compositions

### 4.1.1. Results of $\text{Cu}_{82}\text{Fe}_{12}\text{Co}_6$

As shown in Figure 11 (a), a homogeneous microstructure in the NC regime could be reached for  $\text{Cu}_{82}\text{Fe}_{12}\text{Co}_6$  after deformation for 100 turns at RT. Due to the Z-contrast, particles or phases in the BSE mode appear brighter the higher the atomic mass (or atomic number) of the respective element. Thus, Co- and Fe-particles appear darker than Cu-particles, which occur grayish. However, there is only a small difference between the atomic numbers of Co and Fe, therefore an exact identification is not possible. Moreover, superimposing channeling contrast is also present. The low phase-contrast indicates a good intermixing of the phases. The additional annealing for 1h at 400°C and 10min at 500°C, respectively, does not change the grain size significantly, as can be seen in Figure 11 (b) and (c). However, a higher number of small finely distributed black particles are observed in Figure 11 (b) compared to (a) and (c). These can be identified as ferromagnetic particles (Fe or Co) due to Z-contrast.

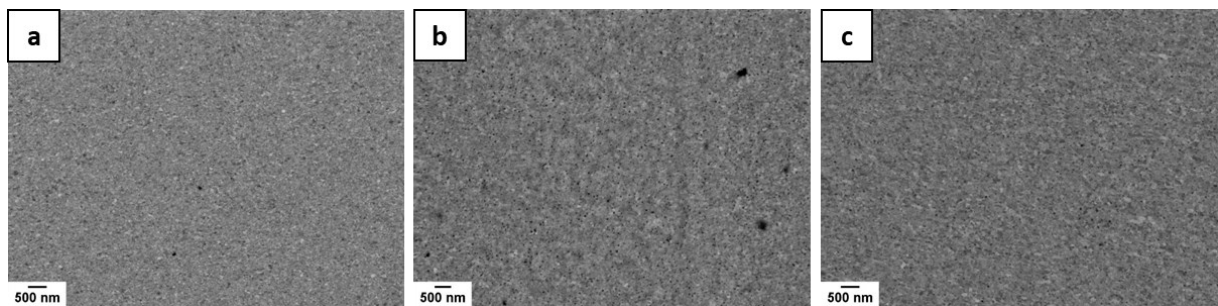


Figure 11: SEM micrographs of  $\text{Cu}_{82}\text{Fe}_{12}\text{Co}_6$  for different annealing states (a) as-deformed (100 turns at RT), (b) 1h at 400°C, and (c) 10min at 500°C (taken in the radial direction).

The averaged chemical composition of this sample was determined by using EDX, consisting of 78.0 wt% Cu, 15.8 wt% Fe, and 6.2 wt% Co.

XRD measurements were performed to study the constituting crystallographic phases of  $\text{Cu}_{82}\text{Fe}_{12}\text{Co}_6$ . Figure 12 and Figure 13 show on the left side the results and on the right side the corresponding sample positions, where the XRD measurements were carried out. To resolve even small particles, a logarithmic scale of normalized intensities of measured patterns was used as a function of the Bragg-angle  $2\theta$ . For this purpose, the measured XRD patterns of the compositions were compared to the calculated diffraction patterns of the individual elements: Cu-fcc, Fe-bcc, and Co-hcp. However, Edalati et al. showed that HPT deformation of pure Co can affect an allotropic phase transformation of hcp to fcc when the grain size can be reduced

down to the nanometer regime so that a fcc and a distorted hcp structure coexist together [40]. Thus, Co-fcc was considered as well.

As can be seen in Figure 12, peaks appear at Bragg-angles which correspond to the calculated patterns of Cu-fcc and Fe-bcc, thus showing a dual-phase structure.

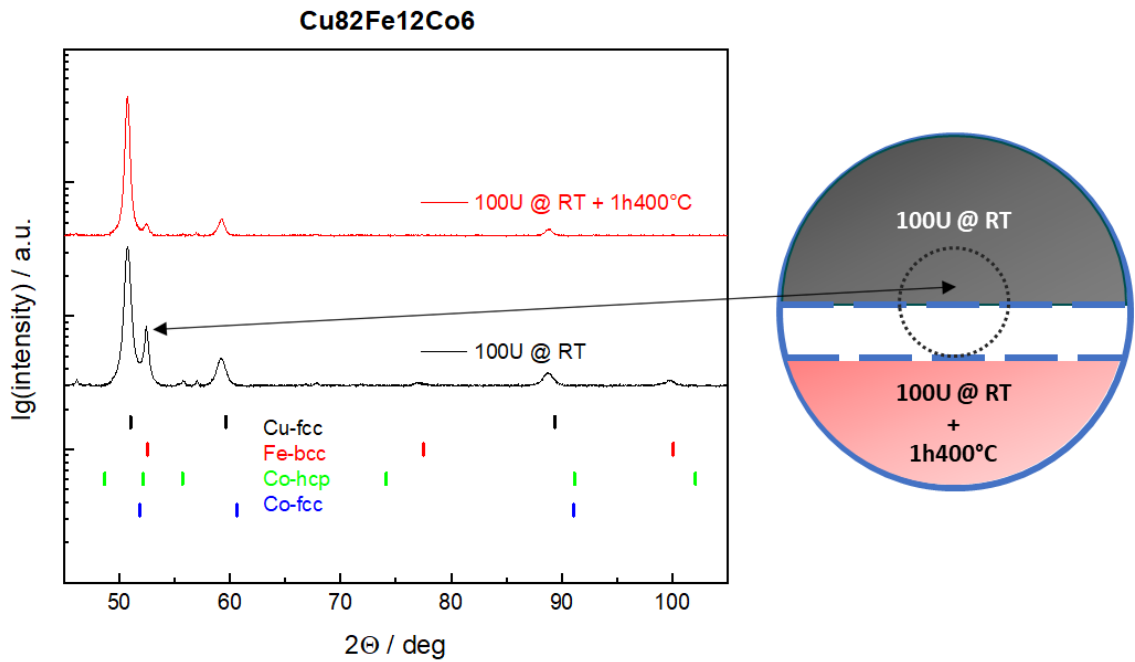


Figure 12: XRD patterns of as-deformed and annealed  $\text{Cu}_{82}\text{Fe}_{12}\text{Co}_6$  taken in the axial direction at half HPT discs (left). Schematic illustration of a HPT disc and the approximate sample positions (red and black shaded areas) where the respective measurement was performed (right).

However, Co-hcp peaks do not occur in the pattern. It can be assumed, that Co-hcp transformed during deformation to Co-fcc. A slight deviation of the Cu-fcc peaks of the as-deformed sample (black pattern) to their calculated pattern position might be explained by supersaturation of the Cu-matrix with Co. In both patterns, the intensity of Cu-fcc peaks is also higher than Fe-bcc peaks, which correlates with the chemical composition of the as-deformed sample. Since annealing promotes phase separation, the intensity of the Fe-bcc peaks of the annealed sample (red pattern) is supposed to be higher than those of the as-deformed sample (black pattern). Nevertheless, the annealed sample shows a lower intensity of Fe-bcc peaks in comparison. However, this behavior can be explained by the sample positions, where the XRD measurements were carried out. The as-deformed sample (black shaded in Figure 12 – right) was measured at sample radii of  $0 \text{ mm} < r < 4 \text{ mm}$  (half HPT disk), while the annealed sample

was measured at higher radii of  $1 \text{ mm} < r < 4 \text{ mm}$  (red shaded in Figure 12 – right). According to equation (4), lower radii correspond to lower shear strain values and therefore to less deformation in the center of the sample. Consequently, a higher occurrence of the Fe-bcc phase is observed in the as-deformed sample is, which is due to less phase intermixing in this low deformation area. This area is indicated by the dotted circle ( $r = 1 \text{ mm}$ ) on the right side of Figure 12. The peaks in Figure 12 at Bragg-angles of approximately  $46^\circ$ ,  $55^\circ$ , and  $57^\circ$  do not agree with any calculated Cu, Co, and Fe patterns. They arise from plasticine, which was used to fix samples on a polymer substrate. It is possible, that the used plasticine contains diffracting particles. However, peaks at these positions were not observed in Figure 13, where the samples were fixed with petroleum jelly on a single-crystalline Si substrate. Moreover, background radiation could be reduced.

In contrast to Figure 12, representing the XRD results of  $\text{Cu}_{82}\text{Fe}_{12}\text{Co}_6$  performed on HPT disc halves, Figure 13 shows XRD measurements, performed directly on the MR samples. As can be seen on the left side of Figure 13, a single-phase fcc structure is visible for the as-deformed  $\text{Cu}_{82}\text{Fe}_{12}\text{Co}_6$  MR sample (black pattern). The stripe-shaped MR samples (blue shaded in Figure 13 – right) were extracted out of the HPT disc halves and cover radii higher than 1.5 mm.

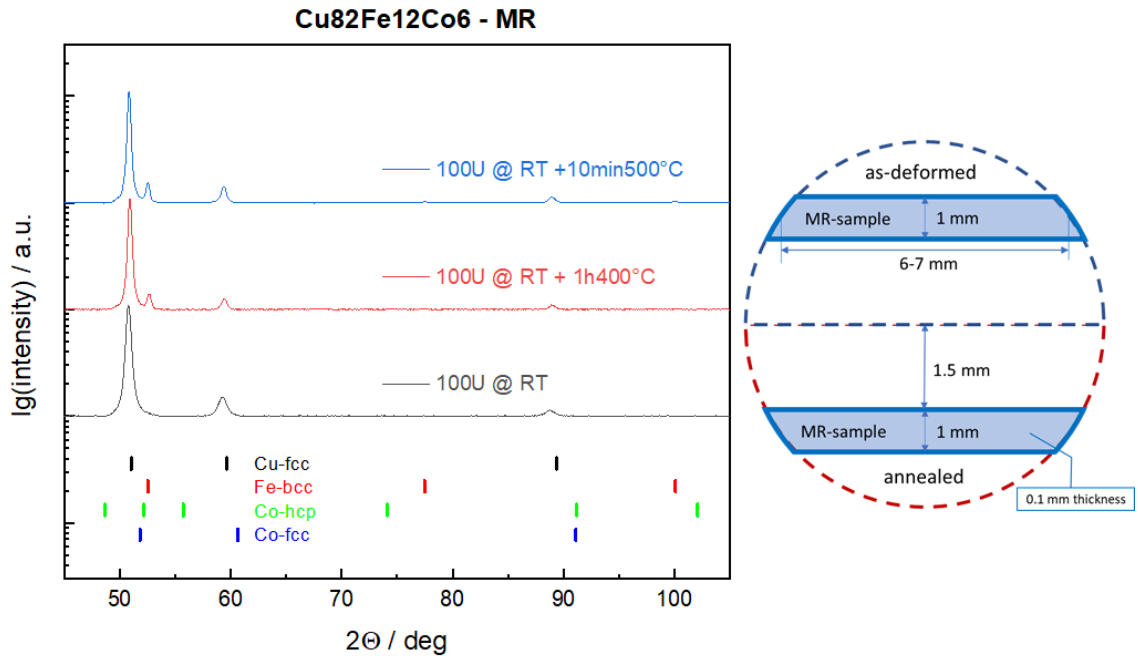


Figure 13: XRD patterns of as-deformed and annealed  $\text{Cu}_{82}\text{Fe}_{12}\text{Co}_6$  taken in the axial direction at MR samples (left). Schematic illustration of a HPT disc and the approximate positions (blue shaded areas) of the MR samples (right).

Compared to the results of the initial as-deformed sample (covering also lower radii) in Figure 12, no Fe-bcc peaks are present in the as-deformed MR sample in Figure 13. This indicates a formation of a supersaturated solid solution at  $r > 1.5$  mm, although Co-Cu and Fe-Cu are immiscible systems at equilibrium conditions [34]. Another possible explanation is that the measured intensity of Fe-bcc peaks may be so low that they disappear in the background radiation. After annealing the samples (red and blue patterns in Figure 13 – left), Fe-bcc peaks occurred, which indicate Fe precipitation. Furthermore, annealing resulted in a slight narrowing of full width at half maximum (FWHM). This indicates slight grain growth, which is in good accordance with the BSE micrographs in Figure 11. A somewhat higher intensity was detected for the Fe-bcc peak at  $2\theta \approx 52^\circ$  for the for 10min at  $500^\circ\text{C}$  compared to the one for 1h at  $400^\circ\text{C}$ , indicating a higher amount of Fe precipitation.

In Figure 14, the decrease of resistivity in dependency of the applied magnetic field is shown. As-deformed (blue data points) and annealed (green and red data points)  $\text{Cu}_{82}\text{Fe}_{12}\text{Co}_6$  samples exhibit a linear negative decrease of resistivity values with increasing magnetic field for both  $I$  to  $H$  directions. Moreover,  $\text{Cu}_{82}\text{Fe}_{12}\text{Co}_6$  exhibits an isotropic GMR behavior in each state, which is indicated by the small difference between the perpendicular and parallel measurements. At a maximum applied field of 22.5 kOe, a GMR of about 1.1 % could be reached for the as-deformed state.

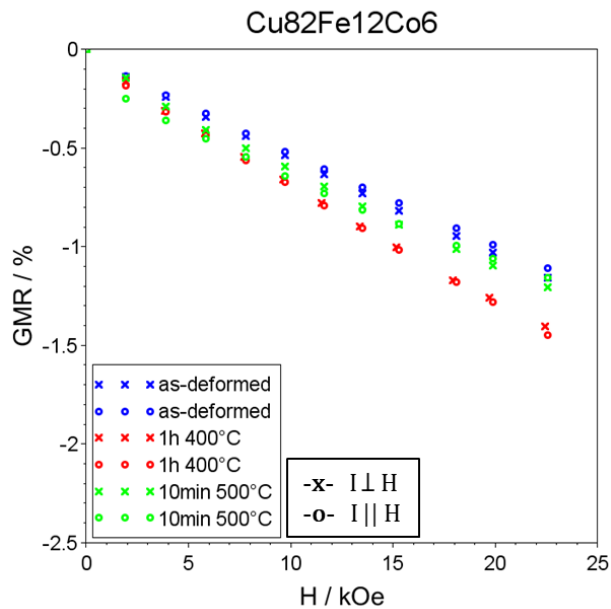


Figure 14: Decrease in resistivity in dependency of the applied magnetic field of  $\text{Cu}_{82}\text{Fe}_{12}\text{Co}_6$  after different annealing states.

For the occurrence of a granular GMR effect, interfaces between magnetic and nonmagnetic phases are required. From XRD-data, these interfaces are not expected to be present. However, a granular GMR effect was measured for the as-deformed sample, despite exhibiting a single-phase fcc structure. Stückler et. al showed with atom probe tomography measurements, that intermixing of Fe and Cu on an atomic scale can be obtained after HPT deformation when the Fe-content is between 7 wt% and 25 wt% with some Fe particles still remaining in the Cu-matrix [38]. It is evident out of the MR results in Figure 14 that magnetic-nonmagnetic interfaces must be present in the as-deformed sample, though are so small that they cannot be detected by low energy XRD. Subsequent annealing led in each case to an amplification of the GMR amplitude. The highest GMR of approximately 1.45 % at 22.5 kOe could be reached after annealing of 1h at 400°C (red data points in Figure 14).

Compared to literature values, a GMR of approximately 15 % was observed for ball-milled  $\text{Cu}_{80}\text{Fe}_{14}\text{Co}_6$  powder annealed for 1h at 415°C. It should be mentioned that this GMR value was estimated out of Fig.3 at  $H \approx 22$  kOe in reference [41]. Furthermore, the annealed composition reaches even higher GMR values up to 16 % at fields of 50 kOe and shows a saturation behavior [41]. Though, it must be mentioned, that the MR measurements in the literature were carried out at a temperature of 5 K, where higher GMR values are accessible at the same fields compared to measurements at RT. As can be seen in Figure 14, no saturation in GMR occurs for  $\text{Cu}_{82}\text{Fe}_{12}\text{Co}_6$  in the range of 0 kOe to 22.5 kOe, even for the annealed samples. This behavior could be caused by local magnetic disorders, due to a transition from ferromagnetic to superparamagnetic behavior, when the particle size of the magnetic particles falls below a critical size. On the one hand, such a superparamagnetic transition results in a decrease of scattering and consequently of the GMR amplitude. On the other hand, a total transition to a superparamagnetic behavior results in no hysteresis and zero coercivity. It can be assumed, due to literature values [41], that a saturation behavior could be reached for  $\text{Cu}_{82}\text{Fe}_{12}\text{Co}_6$  at much higher applied magnetic fields. In addition, increasing the annealing temperature while keeping the time constant can reduce coercivity but at the expense of the GMR amplitude.

#### 4.1.2. Results of $\text{Cu}_{60}\text{Fe}_{20}\text{Ni}_{20}$

The microstructure of as-deformed and annealed  $\text{Cu}_{60}\text{Fe}_{20}\text{Ni}_{20}$  is shown in the SEM micrographs in Figure 15 (a)-(i). The as-deformed sample (see Figure 15 (a)-(c)) exhibits a homogeneously deformed microstructure at any scale and the obtained grain size is in the NC regime.

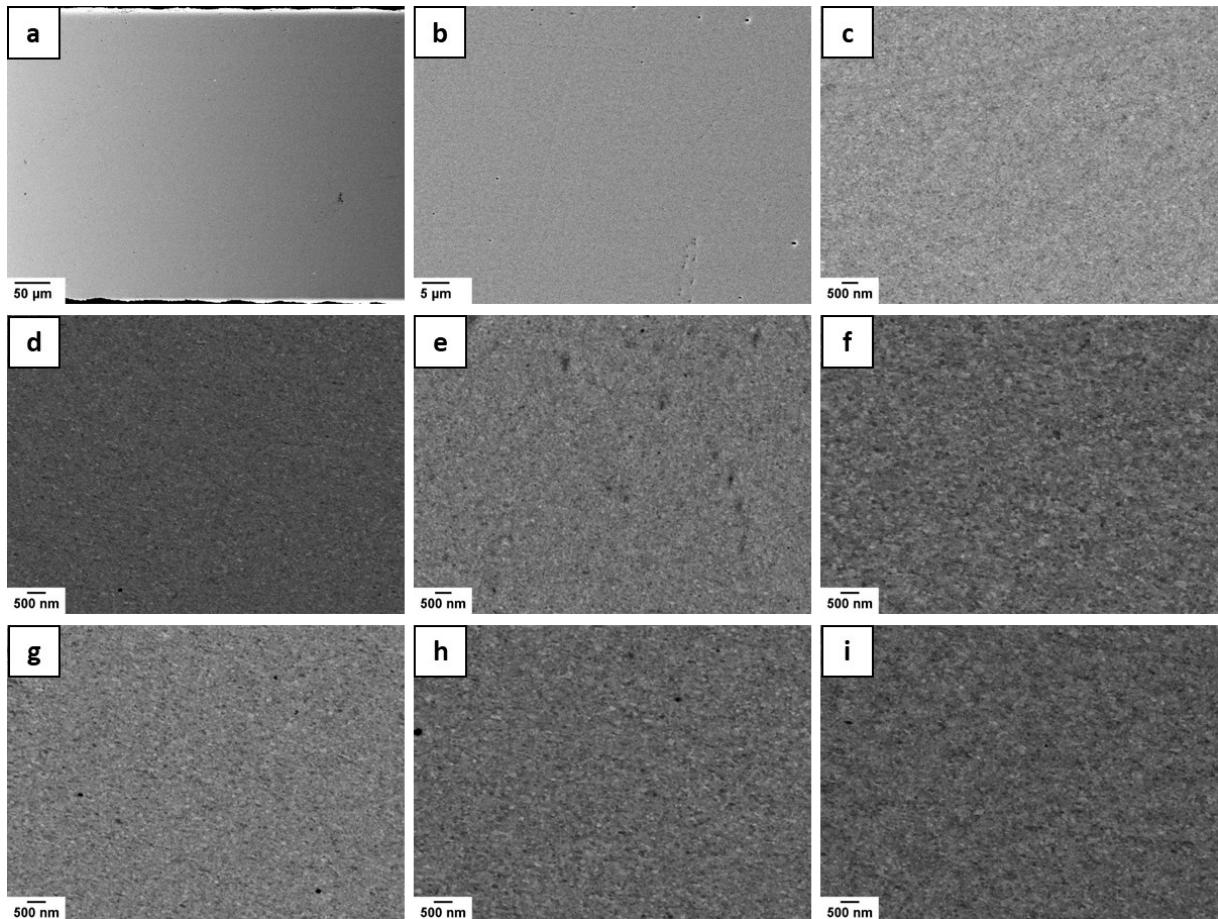


Figure 15: SEM micrographs of the microstructure of  $\text{Cu}_{60}\text{Fe}_{20}\text{Ni}_{20}$  for different annealing states. The micrographs in (a) – (c) show the as-deformed state at different magnifications. The following micrographs show the microstructure after annealing of (d) 1h at 300°C, (e) 1h at 400°C, (f) 100h at 400°C, (g) 10min at 500°C, (h) 10min at 600°C, and (i) 1h at 600°C. The micrographs (a)-(c) were taken in the tangential direction and (d)-(i) in the radial direction at  $r = 3$  mm in BSE mode.

The obtained microstructure after subsequent annealing at different annealing temperatures and durations is shown in Figure 15 (d)-(i). In comparison to the as-deformed state (c), annealing for 1h at 300°C (d) and 400°C (e) caused barely noticeable grain growth. The achieved microstructure is somewhat coarser for higher annealing durations, 100h at 400°C

(f), and higher annealing temperatures, 500°C - 600°C (g)-(i). However, a homogeneous NC microstructure was retained in each case, even at the highest annealing temperature for 1h at 600°C (see Figure 15 (i)). Due to small changes in grain size, the microstructure of  $\text{Cu}_{60}\text{Fe}_{20}\text{Ni}_{20}$  shows high-temperature stability up to 600°C, corresponding to a homologous temperature of 0.64 of Cu. An even better thermal stability (homologous temperature of 0.71) was found for HPT-processed Ag with nanocarbon reinforcements [42]. The coarsest microstructure was obtained for the longest annealing duration of 100h at 400°C (see Figure 15 (f)). However, the grain sizes are still in the NC regime. In the micrographs, Cu-particles are supposed to appear brightest and Fe-particles darkest, whereby Ni-particles exhibit a phase-contrast between Cu and Fe due to Z-contrast. Nevertheless, an exact identification between Ni and Cu is not possible due to the small difference in atomic numbers. Moreover, superimposing channeling contrast is also present. The annealed samples only show a slightly higher phase contrast than the as-deformed sample, which indicates that the phase separation process is in the early stages.

The micrographs in Figure 15 correspond to three different samples with the same nominal composition. Therefore, EDX measurements were carried out on all of these three samples in the as-deformed state at  $r=3$  mm. Sample 08 consists of 62.4 wt% Cu, 19.2 wt% Fe, and 18.5 wt% Ni and corresponds to Figure 15 (a)-(c), (e), and (g). Sample 20 consists of 59.6 wt% Cu, 21.4 wt% Fe, and 19 wt% Ni and corresponds to Figure 15 (f) and (i). Sample 22 consists of 60.5 wt% Cu, 20.6 wt% Fe, and 18.9 wt% Ni and corresponds to Figure 15 (d) and (h). The powder fabrication route via HPT is thus a suitable process regarding reproducibility since the deviations from the nominal composition are small.

Figure 16 shows a qualitative XRD analysis of constituting phases after different annealing of as-deformed  $\text{Cu}_{60}\text{Fe}_{20}\text{Ni}_{20}$  MR samples. For the phase analysis, measured XRD patterns of the compositions were compared to the calculated diffraction patterns of the individual elements: Cu-fcc, Fe-bcc, and Ni-fcc. A single-phase fcc structure consisting of mainly Cu-fcc was reached for as-deformed  $\text{Cu}_{60}\text{Fe}_{20}\text{Ni}_{20}$  (black pattern), as illustrated in Figure 16. No peaks appear at the Fe-bcc and Ni-fcc positions neither in the as-deformed state nor in the annealed states, as shown in Figure 16.



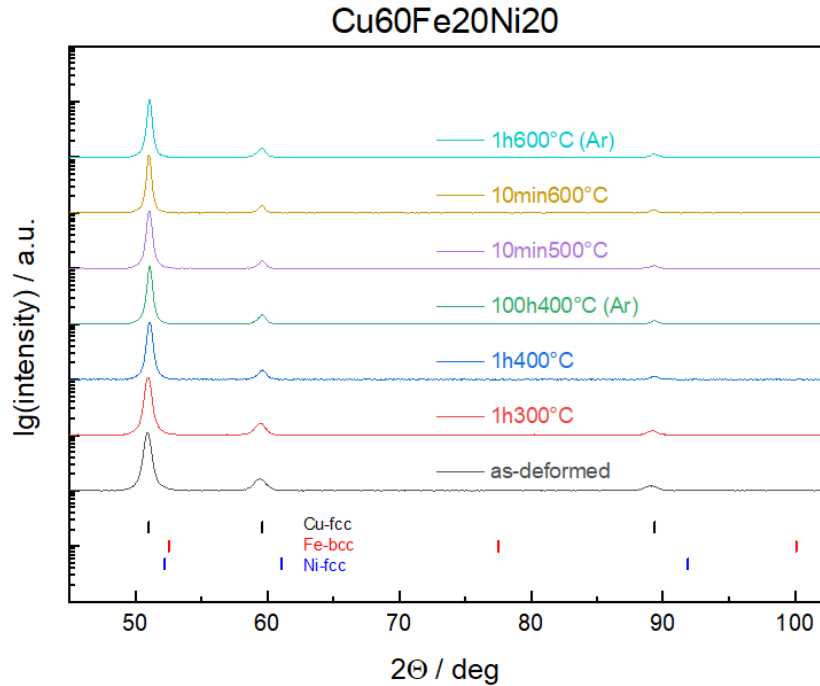


Figure 16: XRD patterns of  $\text{Cu}_{60}\text{Fe}_{20}\text{Ni}_{20}$  for different annealing states. The measurement was conducted on MR samples.

However, the EDX measurements confirm the presence of Fe and Ni in the samples. Therefore, one can assume that Fe and Ni are dissolved in the fcc Cu-matrix. The annealing leads to a peak narrowing, especially for 100h at 400°C and 1h at 600°C. This indicates grain growth and correlates with the BSE micrographs in Figure 15. In addition, XRD measurements confirm the high-temperature stability of the  $\text{Cu}_{60}\text{Fe}_{20}\text{Ni}_{20}$  alloy, since no phase separation occurs, even after annealing at 1h at 600°C.

All as-deformed  $\text{Cu}_{60}\text{Fe}_{20}\text{Ni}_{20}$  samples, named numbers 08, 20, and 22 (corresponding to Figure 17 (a), (b), and (c), respectively) show a linear drop in resistivity with increasing magnetic field. The as-deformed samples (blue data points) in Figure 17 (b) and (c) show a higher deviation from perfect isotropic GMR behavior than the as-deformed sample in (a). In general, a higher decrease of resistivity values was measured when the applied field was perpendicularly oriented to the current. This behavior could be caused by different reasons. On the one hand, the obtained grain shape may differ from a perfect globular shape. Due to shear deformation, the obtained grains exhibit perhaps an ellipsoidal shape. Scattering occurs at ferromagnetic-nonmagnetic interfaces and is thus dependent on the cross-sectional area of the particles. Since an elongated particle exhibits different cross-sectional areas in the longitudinal and transversal directions, the scattering can be influenced by the orientation of the applied field to the current.

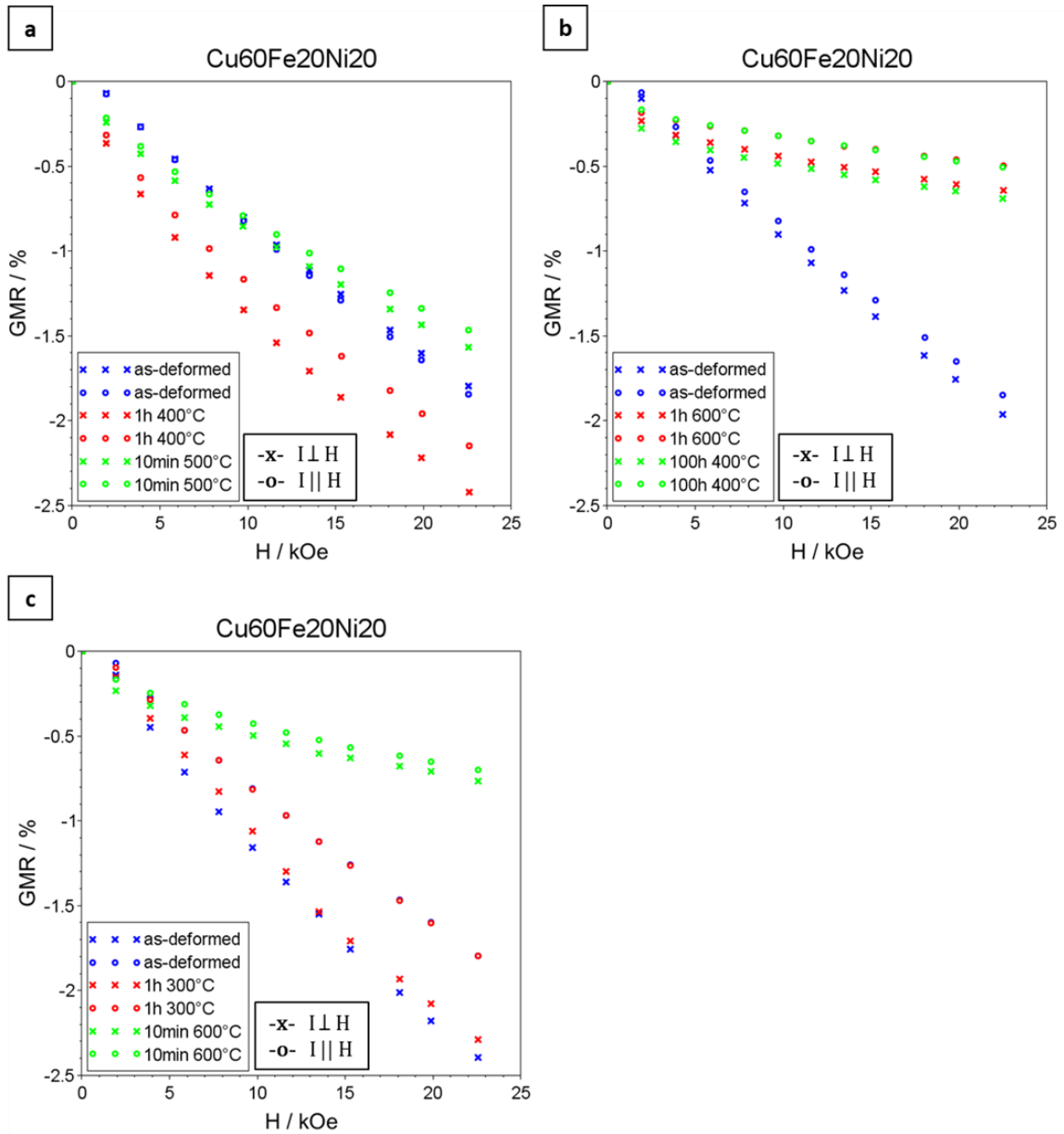


Figure 17: Decrease in resistivity in dependency of the applied magnetic field of  $\text{Cu}_{60}\text{Fe}_{20}\text{Ni}_{20}$  for different annealing states. The results in (a), (b), and (c) correspond to three different samples with the same nominal composition, numbered 08, 20, and 22, respectively.

On the other hand, the ferromagnetic content is approximately 40 wt%. A higher ferromagnetic content favors the formation of multiple domains e.g., large ferromagnetic particles or large percolating domains of a ferromagnetic-rich phase. Thus, a co-existing of the AMR and GMR effect is possible, due to multidomain granules do not contribute to the GMR [43]. For the parallel field measurement at a field of 22.5 kOe, all as-deformed samples show perfect agreement of GMR values of 1.84 %, 1.85 %, and 1.80 %, respectively. GMR values of 1.80 %, 1.96 %, and 2.39 %, respectively, were reached at the same applied field for the perpendicular field measurement. The small deviations of the GMR values of the as-deformed

samples in parallel field direction justify the calculation of a mean value. The mean GMR of  $1.83 \% \pm 0.02 \%$  is illustrated as a gray checkered bar in Figure 18 (b). However, the difference between the reached GMR values at 22.5 kOe of the different as-deformed samples in Figure 17 (a)-(c) is higher for the perpendicular field measurements. Especially, as-deformed sample 22 in Figure 17 (c) exhibits a higher deviation. Nevertheless, the mean GMR of  $2.05 \% \pm 0.25 \%$  was formed for a better comparison of the results, which is displayed as a checkered bar in Figure 18 (a). Moreover, the small deviations in GMR (for the parallel field measurement) between the three as-deformed  $\text{Cu}_{60}\text{Fe}_{20}\text{Ni}_{20}$  samples indicate, that a similar grain size must be obtained after deformation. As a result, good reproducibility of the granular GMR effect could be achieved for the as-deformed state. Thus, it is possible to tune GMR values by adjusting the ferromagnetic particle size with proper annealing. The as-deformed and annealed samples (1h at 300°C and 1h at 400°C) show a linear decrease of GMR values and thus no saturation behavior. An increase of GMR amplitude could be achieved by annealing for 1h at 400°C. At higher annealing temperatures or for longer annealing times (100h at 400°C, 10min at 500°C, 10min at 600°C, and 1h at 600°C) the GMR curves deviate from the linear shape and show a tendency to a saturation behavior. However, at these annealing conditions, a reduction of GMR amplitudes was obtained compared to the as-deformed state. For better comparability, the GMR values occurring at 22.5 kOe in Figure 17 were displayed as absolute values for the perpendicular and parallel orientation of  $H$  to  $I$  in Figure 18 (a) and (b), respectively. Figure 18 (b) clearly shows that the parallel measurements lead to smaller GMR values compared to perpendicular measurements. In comparison to the as-deformed state, increasing annealing temperatures affect an increase of the GMR amplitudes up to 400°C. For 1h at 400°C the highest GMR values of 2.45 % and 2.15 % were observed for perpendicular and parallel orientation, respectively. This increase in GMR is related to an increase in spin-dependent interface scattering, arising from uniform precipitation of small ferromagnetic particles out of the Cu-matrix. Such precipitation was observed in the BSE micrograph in Figure 15 (e). An increase of the annealing duration (100h at 400°C) results in a significant reduction of the GMR amplitude to 0.69 % (perpendicular) and 0.51 % (parallel). Annealing temperatures above 400°C affect a decrease of GMR amplitudes compared to the as-deformed state. This behavior is caused by a coarsening of the microstructure and correlates with the observed XRD measurements (Figure 16) and micrographs (Figure 15). The smallest GMR, 0.64 % (perpendicular) and 0.50 % (parallel), was observed for annealing for 1h at 600°C, which is nearly equivalent to the GMR values of the 100h at 400°C annealed sample.

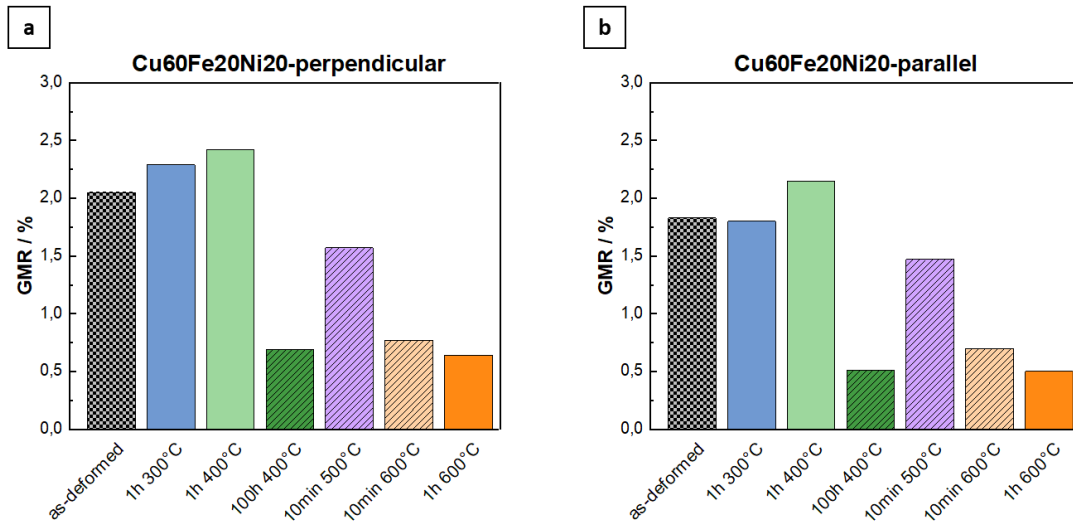


Figure 18: Comparison of the absolute GMR values of Cu<sub>60</sub>Fe<sub>20</sub>Ni<sub>20</sub> for different annealing durations and temperatures. The orientation of the current to the applied magnetic field is in (a) perpendicular and (b) parallel. In both charts, the GMR values correspond to an applied field of 22.5 kOe. For better clarity, the as-deformed sample is checked and those samples whose annealing time deviates from 1h are illustrated hatched.

In comparison to the literature [16], a  $GMR \approx 2.4\%$  was observed at similar conditions (RT measurement up to  $H = 20$  kOe) in spinodal decomposed Cu<sub>60</sub>Fe<sub>20</sub>Ni<sub>20</sub> films. It should be mentioned, that this value was estimated out of Fig.5 from reference [16]. These spinodal decomposed films were fabricated by magnetron sputtering. However, higher GMR values of 6.5 % were reached in this work for applied fields up to 60 kOe, whereby the GMR curve does not saturate even at the maximum applied field. Therefore, it can be assumed that increased GMR amplitudes can be achieved by increasing the strength of the applied field. Furthermore, a RT GMR of about 5 % was reported for bulk as-deformed Cu<sub>60</sub>Fe<sub>20</sub>Ni<sub>20</sub> at 60 kOe [17]. In comparison, a resistivity decrease of only 0.6 % was reported for as-received Cu<sub>60</sub>Fe<sub>20</sub>Ni<sub>20</sub> (~50 nm ferromagnetic particle size) at the maximum applied field. Hence, a deformation of the bulk led to an incredible increase of granular GMR by decreasing the ferromagnetic particle size to 1.5 nm. For better comparability with this work, the GMR value was estimated out of Fig.2 from [17] at almost the same applied field. The GMR amplitude is approximately 2.2 % at 20 kOe for 1.5 nm ferromagnetic particle size.

The measured GMR of 2.45 % (perpendicular) in this thesis is somewhat higher than the reported RT GMR values in reference [16,17]. Nevertheless, Cu<sub>60</sub>Fe<sub>20</sub>Ni<sub>20</sub> is not suitable for GMR-based sensor applications since a large change in resistivity is only achieved at high magnetic fields. Moreover, a saturation behavior of GMR was not observed even at 22.5 kOe.

#### 4.1.3. Results of $\text{Cu}_{80}\text{Fe}_{10}\text{Ni}_{10}$

For better comparability between the different Cu-based compositions,  $\text{Cu}_{80}\text{Fe}_{10}\text{Ni}_{10}$  was exposed to the same heat treatment as  $\text{Cu}_{82}\text{Fe}_{12}\text{Co}_6$  and  $\text{Cu}_{60}\text{Fe}_{20}\text{Ni}_{20}$  in previous chapters. The microstructure of as-deformed and annealed  $\text{Cu}_{80}\text{Fe}_{10}\text{Ni}_{10}$  is shown in the SEM micrographs in Figure 19. A homogeneous NC microstructure was reached in each state.

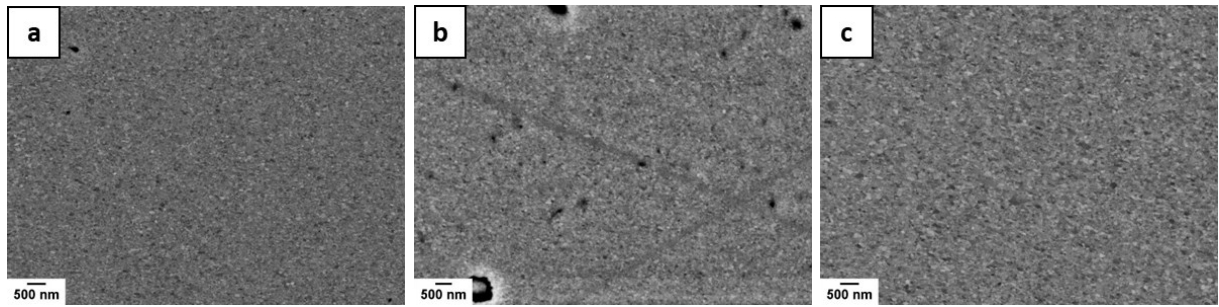


Figure 19: SEM micrographs of  $\text{Cu}_{80}\text{Fe}_{10}\text{Ni}_{10}$  for different annealing states (a) as-deformed (100 turns at RT), (b) 1h at 400°C, and (c) 10min at 500°C (taken in radial direction).

In the micrographs, Cu-particles are supposed to appear brightest and Fe-particles darkest, whereby Ni-particles exhibit a phase-contrast between Cu and Fe due to Z-contrast. Nevertheless, an exact identification between Cu and Ni is not possible due to the small difference in atomic numbers. Moreover, superimposing channeling contrast is also present. The subsequent annealing for 1h at 400°C and 10min at 500°C (Figure 19 (b) and (c)) result in insignificant grain growth. The quite high phase-contrast compared to the as-deformed sample indicates phase separation. However, the process is in the early stages. The microstructure of 1h at 400°C annealed sample (Figure 19 (b)) exhibits artifacts originating from sample preparation such as grind and polishing. The two crossing lines are scratches and the black globular-shaped particles with white borders are charged residuals on the sample surface.

The averaged chemical composition of this sample was determined using EDX, consisting of 84.4 wt% Cu, 6.8 wt% Fe, and 8.8 wt% Ni.

Figure 20 shows the XRD patterns of  $\text{Cu}_{80}\text{Fe}_{10}\text{Ni}_{10}$  in the as-deformed and annealed state. XRD measurements were performed on MR samples (red and green patterns, labeled with (MR)) and on disc halves (black and blue patterns). The MR samples exhibit a single-phase fcc structure in the as-deformed and annealed states (red and green patterns in Figure 20). Since no Fe-bcc peaks appear, it can be assumed that Fe is dissolved in the fcc matrix. As already demonstrated in chapter 4.1.1, more peaks can occur when the XRD measurement is performed on a half HPT disc instead of a MR sample, due to less deformation (and thus less

intermixing) at lower sample radii. As illustrated in Figure 20, a weak Fe-bcc peak appears at  $2\theta \approx 52^\circ$  in the as-deformed sample (black pattern), resulting from a dual-phase structure, consisting mainly of Cu-fcc and small amounts of Fe-bcc. It should be noted that the patterns of Ni-fcc and Fe-bcc nearly overlap at a Bragg-angle of  $52^\circ$ . However, the annealed sample at 1h at  $400^\circ\text{C}$  (blue pattern) shows a single-phase fcc structure without Fe-bcc peaks. The same behavior already occurred in  $\text{Cu}_{82}\text{Fe}_{12}\text{Co}_6$  samples (see Figure 12), which can be explained by the radial dependent deformation and intermixing behavior.

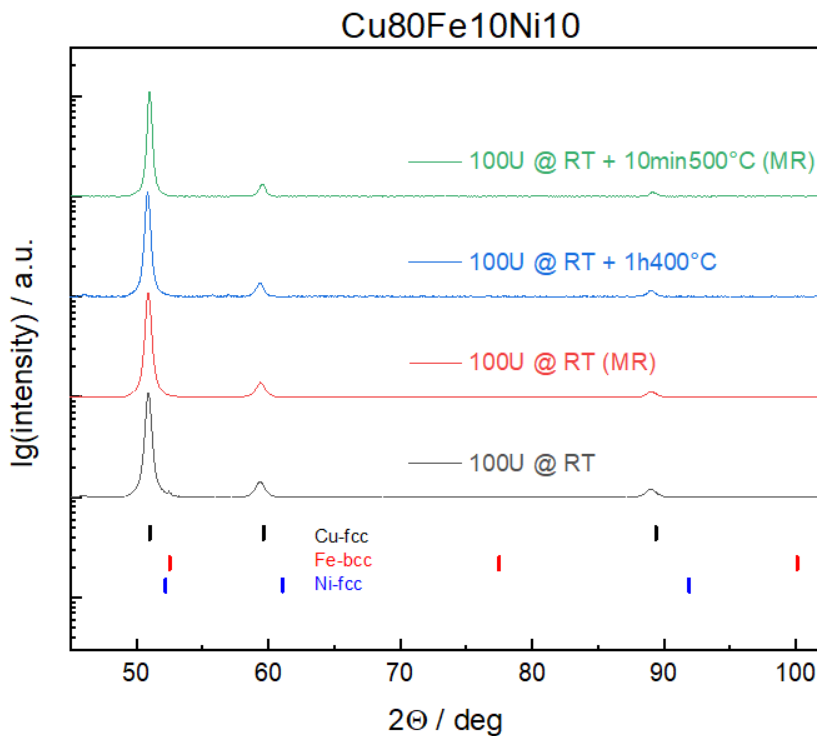


Figure 20: XRD patterns of  $\text{Cu}_{80}\text{Fe}_{10}\text{Ni}_{10}$  for different annealing states. Measurements with an (MR)-label were performed on a MR sample. The others were performed on half HPT discs.

$\text{Cu}_{82}\text{Fe}_{12}\text{Co}_6$  samples (see Figure 13) show phase separation after annealing. In comparison,  $\text{Cu}_{80}\text{Fe}_{10}\text{Ni}_{10}$  does not show a de-mixing of phases, though the samples were exposed to the same annealing parameters (see Figure 20). This indicates, that  $\text{Cu}_{80}\text{Fe}_{10}\text{Ni}_{10}$  exhibits higher single-phase stability than  $\text{Cu}_{82}\text{Fe}_{12}\text{Co}_6$ . The green pattern (10min at  $500^\circ\text{C}$ ) exhibits narrower peaks than the red pattern (as-deformed). This peak narrowing arises from grain growth and correlates with the micrographs in Figure 19.

MR measurements of as-deformed and annealed  $\text{Cu}_{80}\text{Fe}_{10}\text{Ni}_{10}$  are shown in Figure 21. The resistivity decreases in each case with an increasing magnetic field. All MR measurements show a perfect isotropic GMR behavior, i.e., the perpendicular and parallel measured values show almost no deviation from each other. The as-deformed sample (blue data points) shows a linear decrease in resistivity values with increasing field. A GMR of 0.6 % was reached at 22.5 kOe for both  $H$  to  $I$  orientations.

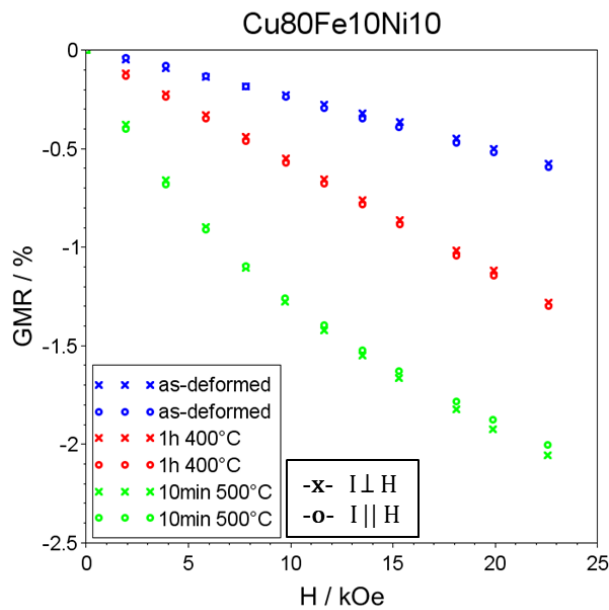


Figure 21: Decrease in resistivity in dependency of the applied magnetic field of  $\text{Cu}_{80}\text{Fe}_{10}\text{Ni}_{10}$  after different annealing states.

In comparison, as-deformed  $\text{Cu}_{82}\text{Fe}_{12}\text{Co}_6$  and  $\text{Cu}_{60}\text{Fe}_{20}\text{Ni}_{20}$  reached higher GMR amplitudes of 1.1 % and 1.83 %, respectively. The subsequent annealing leads in both cases, 1h at 400°C and 10min at 500°C, to an improvement of the GMR amplitude of  $\text{Cu}_{80}\text{Fe}_{10}\text{Ni}_{10}$  (Figure 21). A linear GMR dependency was observed for the 1h at 400°C annealed sample (red data points) with increasing field. The obtained GMR of 1.3 % at the maximum field is more than two times higher compared to the as-deformed state. Annealing for 10min at 500°C (green data points) results in a maximum GMR of approximately 2 %, which is more than a threefold amplification of the GMR amplitude. The 10min at 500°C sample shows a tendency of saturation behavior. The GMR values decrease nearly quadratically with increasing field. Thus, the change in resistivity correlates with the squared global relative magnetization according to equation (3), supposing its linear increase with applied magnetic field.

The same heat treatment (10min at 500°C) resulted only in a weak raise of the GMR amplitude in  $\text{Cu}_{82}\text{Fe}_{12}\text{Co}_6$  (Figure 14) and a reduction of the GMR amplitude in  $\text{Cu}_{60}\text{Fe}_{20}\text{Ni}_{20}$  (Figure 17 (a)) compared to their as-deformed state. Annealing for 1h at 400°C had in each case a positive effect regarding the change in resistivity.

In comparison to literature values [44], GMR values of 8 % were found in  $\text{Cu}_{80}\text{Fe}_{10}\text{Ni}_{10}$  ribbons. These ribbons were fabricated by melt spinning. An even higher GMR amplitude of 19 % could be achieved with subsequent annealing for 2h at 400°C. However, these values were measured at a temperature of 50 K and at a field of 70 kOe. Furthermore, the GMR curves saturate at lower applied fields when the measuring temperature decreases. In the work of Martins and Missell, additional RT MR measurements were carried out on as-casted  $\text{Cu}_{80}\text{Fe}_{15}\text{Ni}_5$  ribbons. This composition achieved a GMR of only about 0.2 % at RT for a field of 20 kOe. This value was estimated out of Fig.3 in reference [44]. Consequently, an enlargement of GMR amplitudes is expected to occur at lower measuring temperatures and higher applied fields.



## 4.2. Ag-based compositions

### 4.2.1. Results of $\text{Ag}_{83}\text{Co}_{17}$

SEM micrographs in Figure 22 show the microstructure of as-deformed  $\text{Ag}_{83}\text{Co}_{17}$ . Due to Z-contrast, Co appears darker than Ag in the micrographs. As can be seen in Figure 22 (a)-(c), residual Co particles (black) appear in different size distributions in the Ag-matrix (gray). The biggest particles exhibit a size in the range of 50  $\mu\text{m}$ . However, the initial particle size of the used Co powder is smaller than 30  $\mu\text{m}$  (see Table 2) and thus smaller than the observed particles in the Ag-matrix. The enlarged particles could arise from an agglomeration of Co-particles during the mixing process of the powder composition. During powder consolidation, more dense and larger particles were formed.

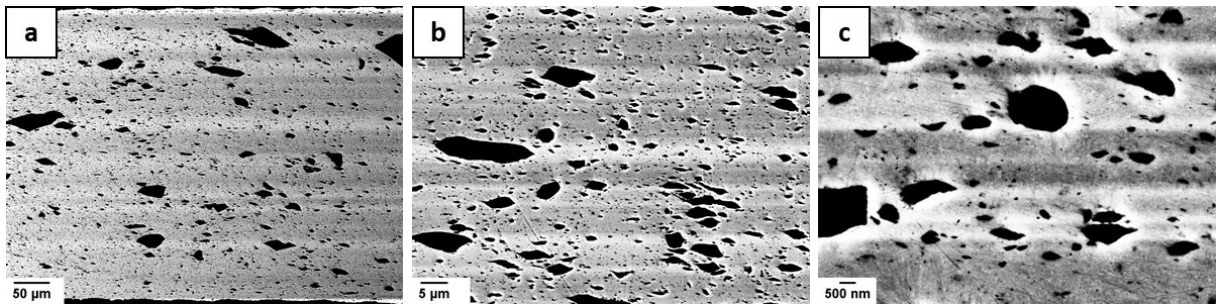


Figure 22: SEM micrographs of different magnifications of as-deformed  $\text{Ag}_{83}\text{Co}_{17}$  (100 turns at RT) performed in the tangential direction at  $r = 3$  mm.

Evidently, the harder Co particles did not properly co-deform in the softer Ag-matrix during the HPT deformation process. Due to the applied pressure (in the axial direction) and shear strain, Co particles were deformed in the shear direction, resulting in the obtained elongated shape. The desired microstructure, an Ag-matrix with finely dispersed NC Co-particles, could not be reached for  $\text{Ag}_{83}\text{Co}_{17}$  in the as-deformed state. Therefore, no heat treatment was carried out for this composition.

The averaged chemical composition of this sample was determined using EDX, consisting of 81.8 wt% Ag and 18.2 wt% Co.

Figure 23 shows the XRD pattern of as-deformed  $\text{Ag}_{83}\text{Co}_{17}$ . The measured pattern (black) of the sample was compared with the calculated diffraction patterns of the individual elements: Ag-fcc, Co-hcp, and Co-fcc. Peaks with higher intensities can be identified as Ag-fcc, which agrees with the measured chemical composition.

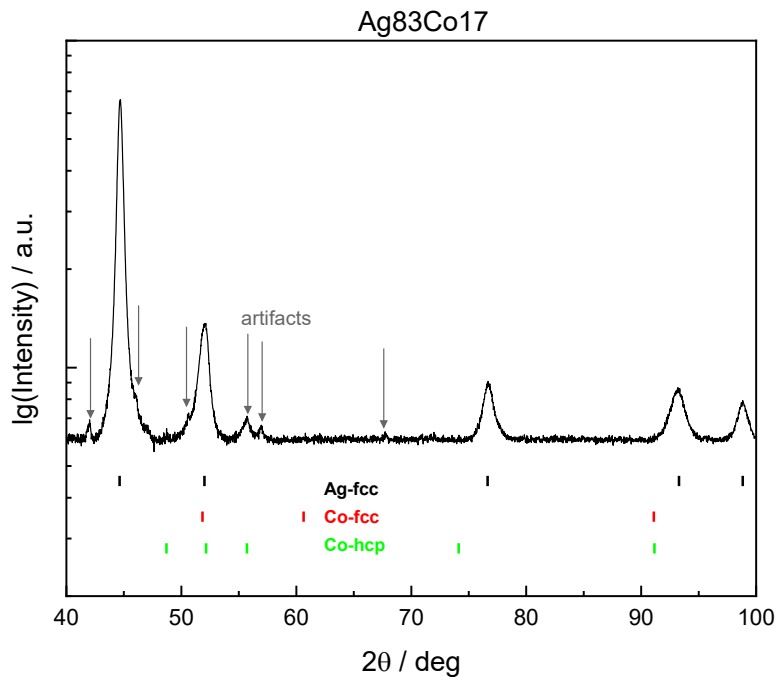


Figure 23: XRD pattern of as-deformed  $\text{Ag}_{83}\text{Co}_{17}$  (100 turns at RT) taken in the axial direction.

It comes to an overlapping of the calculated Ag-fcc and Co-hcp pattern at  $2\theta = 52^\circ$ . Thus, Ag-fcc and Co-hcp peaks cannot be distinguished. However, the EDX measurement and SEM micrographs in Figure 22 confirm the existence of Co in this composition. The occurrence of peak shift due to supersaturation of the Ag-matrix with Co can be excluded since the poorly co-deformed Co particles are too big to dissolve in the Ag-matrix (see SEM micrographs in Figure 22). Peaks with smaller intensities (indicated with gray arrows) correspond to measurement artifacts. They were caused by the plasticine, which was used to fix the sample on the polymer substrate.

For the occurrence of the granular GMR effect, the embedded ferromagnetic particles must be smaller in size (NC regime) and more homogeneously in size distribution. Since the desired microstructure was not reached, no MR measurements were performed on  $\text{Ag}_{83}\text{Co}_{17}$ .

#### 4.2.2. Results of $\text{Ag}_{84}\text{Fe}_{16}$

Besides using elemental powders in the as-received state, initial elemental powders (Ag and Fe) were additionally BMVA-pretreated (as described in chapter 3.1). This aims to enhance the co-deformability and thus the refinement of the ferromagnetic phase in  $\text{Ag}_{84}\text{Fe}_{16}$  during the HPT process. Figure 24 (a) shows the microstructure of as-deformed  $\text{Ag}_{84}\text{Fe}_{16}$  using untreated powders. In contrast, Figure 24 (b) shows the microstructure of as-deformed  $\text{Ag}_{84}\text{Fe}_{16}$  using BMVA-pretreated powders.

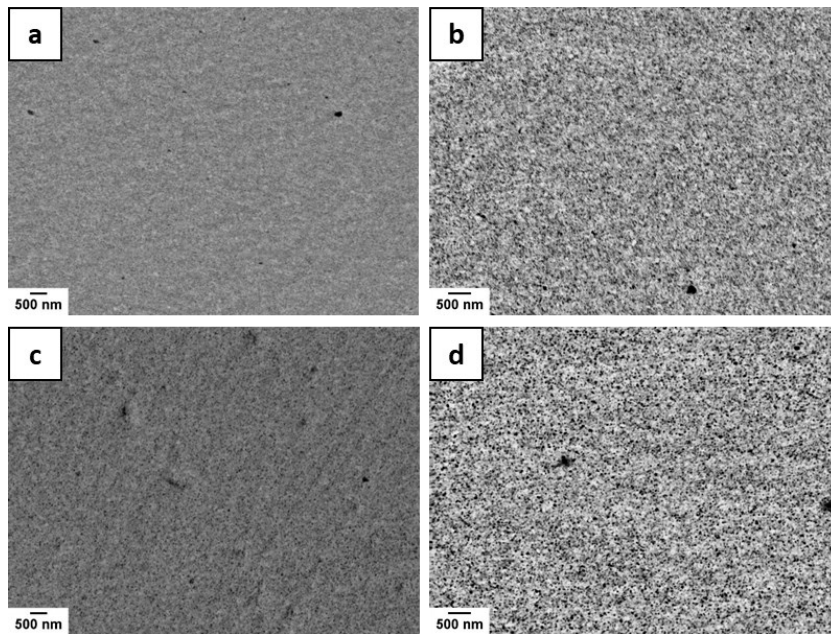


Figure 24: SEM micrographs above show the microstructure of (a) untreated and as-deformed  $\text{Ag}_{84}\text{Fe}_{16}$  and (b) BMVA-pretreated and as-deformed  $\text{Ag}_{84}\text{Fe}_{16}$ . The micrographs below (c) and (d) show the respective microstructures of (a) and (b) after annealing for 1h at  $400^{\circ}\text{C}$ .

After deformation for 100 turns at RT, both samples exhibit a homogeneous NC microstructure. Contrary to expectations, the BMVA pretreatment resulted in a coarser microstructure after HPT processing. Further, the higher phase-contrast of the BMVA-pretreated composition in (b) indicates less intermixing during the deformation process compared to the untreated composition in (a). In general, Ag appears brighter than Fe in the micrographs in Figure 24, due to Z-contrast. The microstructure in (a) appears grayish, which indicates a supersaturated Ag-matrix with Fe. Only a few residual Fe particles (black) are observed in the Ag-matrix.

Subsequent annealing (1h at 400°C) of the untreated as-deformed sample led to fine precipitation of Fe (black), as can be seen in Figure 24 (c). The obtained microstructure is still in the NC regime since almost no grain growth is evident. Annealing (1h at 400°C) of the BMVA-pretreated as-deformed sample (see Figure 24 (d)) caused grain growth. However, the average grain size in (b) and (d) is still in the NC regime. In comparison, the annealed BMVA sample in (d) shows larger grain sizes and phase contrast than the annealed untreated sample in (c).

The averaged chemical composition of these samples was determined using EDX. The as-deformed sample using untreated powders (Figure 24 (a)) consists of 77.9 wt% Ag and 22.1 wt% Fe, and the as-deformed sample using BMVA-treated powders (Figure 24 (b)) consists of 86.2 wt% Ag and 13.8 wt% Fe.

Figure 25 shows XRD patterns of untreated and BMVA-pretreated  $Ag_{84}Fe_{16}$  in the as-deformed (100 turns at RT) and annealed state (1h at 400°C). A single-phase structure consisting of Ag-fcc could be reached for untreated as-deformed  $Ag_{84}Fe_{16}$  (black pattern). However, Fe-bcc peaks could not be detected. Thus, supersaturation of Fe in the Ag-matrix can be assumed. A Fe-bcc peak might be present at  $2\theta \approx 52.5^\circ$ .

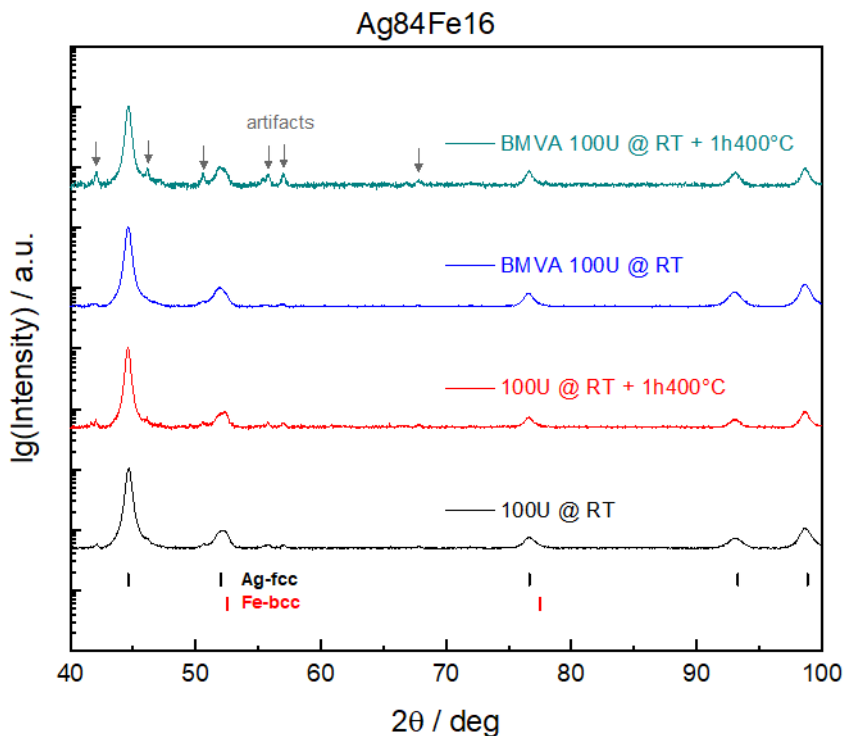


Figure 25: XRD patterns of untreated and BMVA-pretreated  $Ag_{84}Fe_{16}$  in the as-deformed and annealed state.

However, its intensity could be too low for detection and thus disappear in the signal of the Ag-fcc peak at  $2\theta \approx 52^\circ$ . The measured pattern of the as-deformed sample (black) agrees with the observed microstructure in Figure 24 (a). The weak peaks which do not agree with the calculated positions of Ag-fcc and Fe-bcc are measurement artifacts. They arise from the plasticine, which was used to fix the sample on the polymer substrate. These artifacts occur in all patterns in Figure 25, especially in the top pattern (indicated with gray arrows). Subsequent annealing for 1h at  $400^\circ\text{C}$  (red pattern) affected a weak phase separation (towards Fe-bcc) at  $2\theta \approx 52^\circ$ . This indicates precipitation of Fe and correlates with the observed microstructure in Figure 24 (c). Furthermore, the annealed sample (red) shows a smaller FWHM compared to the as-deformed sample (black), arising from grain growth. In comparison, similar patterns were observed in the as-deformed (blue pattern) and annealed state (green pattern) of BMVA-pretreated  $\text{Ag}_{84}\text{Fe}_{16}$ . These measured patterns also correlate with the observed microstructures in Figure 24 (b) and (d).

MR measurements of the investigated  $\text{Ag}_{84}\text{Fe}_{16}$  are shown in Figure 26. The as-deformed sample (blue data points) shows for both fields to current directions a small decrease of resistivity values with increasing field. At the maximum applied field, GMR amplitudes of 0.4 % and 0.5 % were reached for the parallel and perpendicular  $H$  to  $I$  direction.

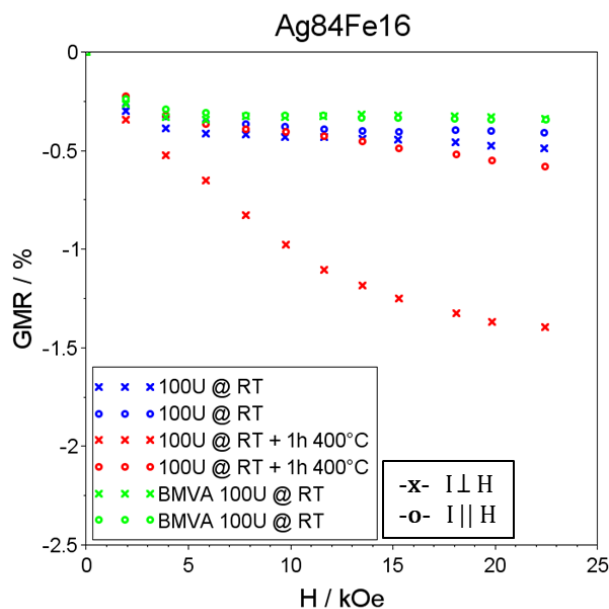


Figure 26: Decrease in resistivity in dependency of the applied magnetic field of as-deformed, annealed, and BMVA-as-deformed  $\text{Ag}_{84}\text{Fe}_{16}$ .

In comparison, the BMVA pretreatment (green data points) led to a decrease of the GMR amplitude (0.35 %) at the maximum applied field. The decrease of GMR amplitude can be explained by the coarser microstructure of the BMVA-pretreated sample (see Figure 24 (b)), which leads to less interface scattering. Both as-deformed samples show a nearly perfect isotropic GMR behavior and their resistivities saturate for applied fields above 5 kOe. Subsequent annealing resulted in a strong deviation between the MR branches (perpendicular and parallel). Thus, annealing led rather into unexpected AMR than GMR behavior. Generally, higher GMR values were reached when the applied field was aligned perpendicularly to the current. At 22.5 kOe, GMR values of 0.6 % and 1.4 % were obtained for the parallel and perpendicular  $H$  to  $I$  orientation.

In comparison to literature values [15], a higher RT GMR amplitude of 6.59 % was found for magnetron-sputtered  $\text{Ag}_{80}\text{Fe}_{20}$  (vol%).  $\text{Ag}_{80}\text{Fe}_{20}$  in vol% is equivalent to  $\text{Ag}_{84}\text{Fe}_{16}$  in wt%. Annealing for 15min at 400°C in a high vacuum resulted in a significant decrease of the RT GMR amplitude to 0.7 %. These GMR amplitudes were determined for very high applied fields up to 80 kOe. Even higher values of 21.5% (as-sputtered) and 5.78 % (annealed, 15min at 400°C) were observed at a measuring temperature of 4 K for the same applied fields.

In contrast to the Cu-based alloys in chapter 4.1,  $\text{Ag}_{84}\text{Fe}_{16}$  shows a saturation behavior but reaches much lower GMR amplitudes.

#### 4.2.3. Results of $\text{Ag}_{84}\text{Fe}_{12}\text{Co}_4$

Co-Ag is supposed to reach higher GMR values for the same ferromagnetic content than Fe-Ag [15]. Since  $\text{Ag}_{83}\text{Co}_{17}$  showed insufficient co-deformability of the individual elements compared to  $\text{Ag}_{84}\text{Fe}_{16}$ , Fe was partially replaced with Co. This approach aims to improve the GMR amplitude and ferromagnetic phase refinement. Moreover, different process parameters were attempted to optimize the microstructure. Figure 27 (a)-(c) shows the microstructure of as-deformed  $\text{Ag}_{84}\text{Fe}_{12}\text{Co}_4$  using untreated and also BMVA-pretreated powders. The untreated powder composition was deformed for (a) 100 turns at RT and (b) 100 turns at 300°C. To enhance the co-deformability and thus the refinement of the ferromagnetic phase in Ag-Fe-Co during the HPT process, the softer Ag-powder was ball-milled and the harder Co and Fe powders were heat treated before the HPT pre-compaction process. The microstructure of BMVA-pretreated and as-deformed (100 turns at RT)  $\text{Ag}_{84}\text{Fe}_{12}\text{Co}_4$  is shown in (c). As-deformed samples in (a), (b), and (c) were subsequently annealed for 1h at 400°C, which are illustrated in (d), (e), and (f).

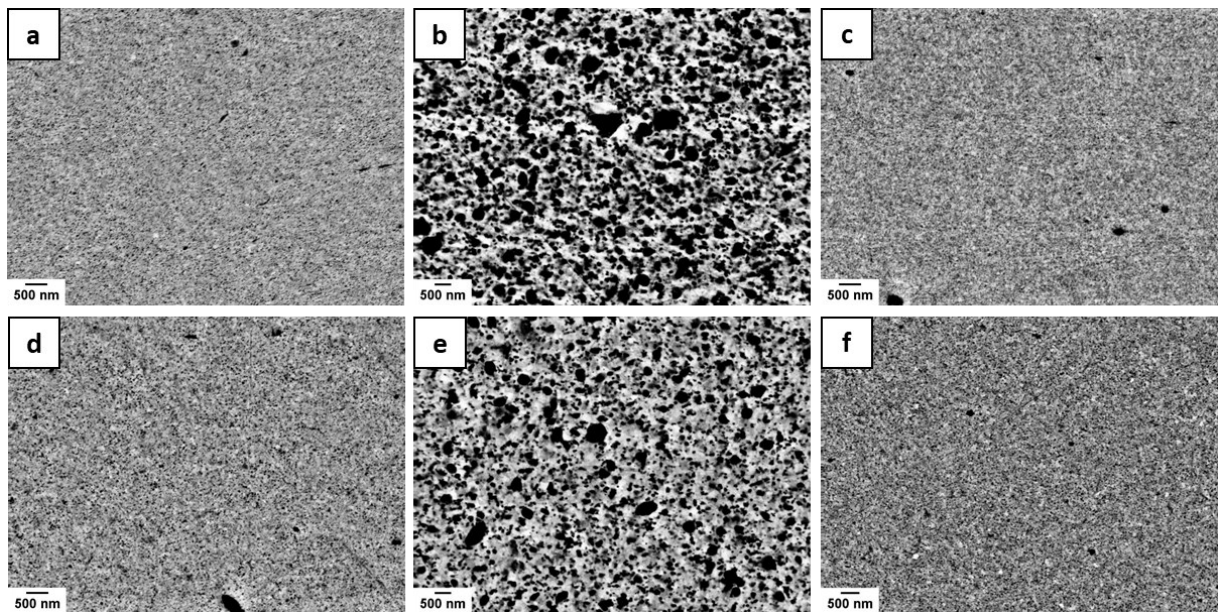


Figure 27: SEM micrographs of the microstructure of  $\text{Ag}_{84}\text{Fe}_{12}\text{Co}_4$  after deformation for (a) 100 turns at RT, (b) 100 turns at 300°C, and (c) 100 turns at RT (BMVA-pretreated). The bottom micrographs (d), (e), and (f) show the respective microstructures of (a), (b), and (c) after annealing for 1h at 400°C.

In the micrographs, Ag-matrix is supposed to appear brightest and Fe-particles darkest, whereby Co-particles exhibit a phase-contrast between Ag and Fe due to Z-contrast. However, there is only a small difference between the atomic numbers of Co and Fe, therefore an exact identification is not possible. Moreover, superimposing channeling contrast is also present. As

can be seen in (a), a homogeneous NC microstructure was obtained after deformation for 100 turns at RT. However, some larger residual ferromagnetic particles remained in the Ag-matrix, as can be seen in Figure A.7 (a) in the appendix. Deformation at higher temperatures (100 turns at 300°C) resulted in a significantly coarser microstructure with grain sizes in the submicron range. Due to the high phase-contrast in (b), the black particles can be identified as ferromagnetic particles (Fe or Co). A prior BMVA treatment to the deformation process led to a NC matrix with residual ferromagnetic particles (see Figure 27 (c)). These ferromagnetic particles are partially quite large (see Figure A.7 (c) in the appendix). The enlarged ferromagnetic particles could arise from an agglomeration of the initial powders due to prior vacuum annealing. During powder consolidation, more dense and larger particles were formed. Thus, the harder Co and Fe particles did not properly co-deform in the softer Ag-matrix during the HPT deformation process. Subsequent annealing of the as-deformed sample in (a), affected a slight grain coarsening as can be seen in (d). In comparison, no significant change in grain size occurs after annealing of the samples in (b) and (c), as shown in (e) and (f). It should be mentioned that no process step led to the desired microstructure for an optimal GMR. Larger ferromagnetic particles remained in the matrix, which did not properly co-deform (see Figure A.7 in the appendix).

The averaged chemical composition of these samples was determined using EDX. The as-deformed sample in Figure 27 (a) consists of 87.0 wt% Ag, 11.8 wt% Fe, and 1.1 wt% Co; in (b) of 78.6 wt% Ag, 16.1 wt% Fe, and 5.3 wt% Co; and in (c) of 86.9 wt% Ag, 11.2 wt% Fe, and 2.0 wt% Co.

XRD measurements were performed to investigate the constituting crystallographic phases after deformation and annealing of  $\text{Ag}_{84}\text{Fe}_{12}\text{Co}_4$  (see Figure 28). The measured XRD patterns of the compositions were compared to the calculated diffraction patterns of the individual elements: Ag-fcc, Fe-bcc, Co-hcp, and Co-fcc. The upper two patterns in Figure 28 correspond to as-deformed  $\text{Ag}_{84}\text{Fe}_{12}\text{Co}_4$  samples using BMVA-pretreated powders. Otherwise, untreated powders were used. As-deformed  $\text{Ag}_{84}\text{Fe}_{12}\text{Co}_4$  (100 turns at RT) exhibits a single-phase fcc structure consisting of Ag-fcc. Co and Fe peaks do not occur, which could be caused by the supersaturation of Co and Fe in the Ag-matrix. However, the measured intensities of Co and Fe might be too low for their detection. Therefore, their peaks disappear in the signal of the Ag-fcc peak at  $2\theta \approx 52^\circ$ . The measured pattern correlates with the observed microstructure in Figure 27 (a). However, further peaks of lower intensities appear which cannot be identified with the calculated patterns of Ag-fcc, Co-hcp, Co-fcc, and Fe-bcc. These peaks are measurement artifacts (indicated with gray arrows) and occur also in the other patterns. They were caused by the plasticine which was used to fix the sample on the polymer substrate. Subsequent annealing for 1h at 400°C led to somewhat narrower peaks in the red pattern,



indicating slight grain growth. This measurement is confirmed with the observed microstructure in the micrographs of Figure 27 (a) and (c).

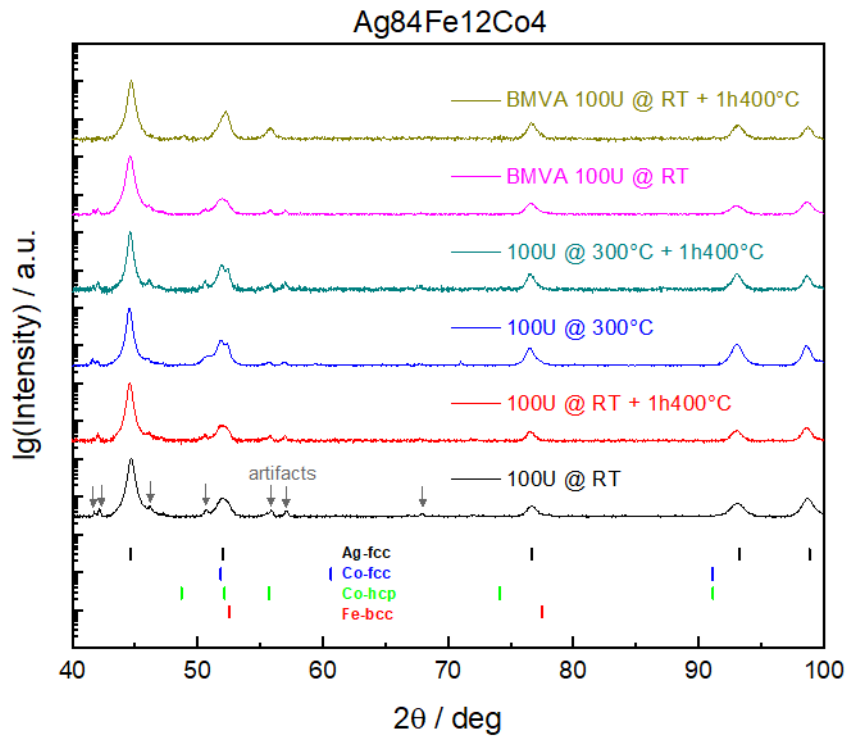


Figure 28: XRD patterns of untreated and BMVA-pretreated  $\text{Ag}_{84}\text{Fe}_{12}\text{Co}_4$  in the as-deformed and annealed states.

In comparison, deformation at higher temperatures (100 turns at  $300^\circ\text{C}$ ) led to separated phases (blue pattern) at  $2\theta \approx 52^\circ$ , which agrees with the observed microstructure in Figure 27 (b). The peak at  $51.8^\circ$  matches with Co-fcc, while the peak at  $52.4^\circ$  is supposed to be a mixed peak of Co-hcp and Fe-bcc. Other peaks with higher intensities in this pattern correspond to Ag-fcc. Thus, all elements co-exist after deformation for 100 turns at  $300^\circ\text{C}$ . Subsequent annealing for 1h at  $400^\circ\text{C}$  (green pattern) resulted in somewhat higher phase separation in comparison to the as-deformed state (blue pattern). A single-phase fcc structure was measured for as-deformed  $\text{Ag}_{84}\text{Fe}_{12}\text{Co}_4$  using BMVA pretreated powders (pink pattern). The BMVA-pretreated as-deformed sample (pink pattern) shows peaks with smaller FWHM compared to the untreated as-deformed sample (black pattern), indicating a larger grain size. These enlarged grains are probably caused by the vacuum annealing of Co and Fe. Subsequent annealing for 1h at  $400^\circ\text{C}$  of the BMVA-as-deformed sample affected a slight shift of the peaks to higher Bragg-angles (brown pattern). The peak at  $2\theta \approx 52^\circ$  exhibits a higher intensity compared to the peaks of other patterns at this position. Due to the shift, a mixed peak ( $52^\circ$ )

of Co-hcp and Fe-bcc was obtained. However, exact identification of this peak is not possible, since the calculated patterns (Ag-fcc, Co-fcc, Co-hcp, Fe-bcc) nearly overlap at  $2\theta \approx 52^\circ$ . In addition, a Co-hcp peak occurs at  $2\theta \approx 56^\circ$ .

MR measurements were only performed on as-deformed  $\text{Ag}_{84}\text{Fe}_{12}\text{Co}_4$  samples, as shown in Figure 29. After deformation for 100 turns at RT (blue data points) of untreated  $\text{Ag}_{84}\text{Fe}_{12}\text{Co}_4$ , a decrease of resistivity values was observed with an increasing field for both field directions. However, the MR branches (perpendicular and parallel) slightly deviate from each other. At 22.5 kOe, GMR values of 0.36 % and 0.27 % were found for perpendicular and parallel applied  $I$  to  $H$ . Further, the GMR curve (blue) shows a saturation behavior. In comparison, somewhat higher GMR amplitudes were measured for as-deformed  $\text{Ag}_{84}\text{Fe}_{16}$  (see Figure 26), which can be attributed to the finer microstructure.

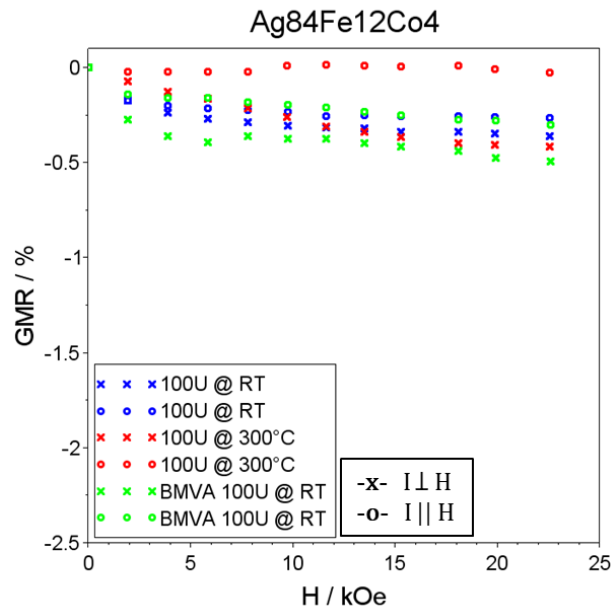


Figure 29: Decrease in resistivity in dependency of the applied magnetic field of as-deformed and BMVA-as-deformed  $\text{Ag}_{84}\text{Fe}_{12}\text{Co}_4$ .

An increasing deformation temperature (100 turns at  $300^\circ\text{C}$ ) resulted in a higher difference between the MR branches (red data points). In the parallel  $I$  to  $H$  measurement, resistivity values change approximately between  $-0.025\%$  and  $+0.02\%$ . In the perpendicular  $I$  to  $H$  measurement, resistivity values decrease with increasing field. A maximum MR of  $-0.42\%$  is reached at 22.5 kOe. Generally speaking, an increasing deviation of the MR branches indicates the tendency of the material towards AMR behavior. Higher deformation temperatures (see

Figure 27 (b)) favor the formation of multiple domains e.g., large ferromagnetic particles or large percolating domains of a ferromagnetic-rich phase. Thus, a co-existing of the AMR and GMR effect is possible, due to multidomain granules which do not contribute to the GMR. However, AMR behavior tends to dominate with larger ferromagnetic grains (induced by higher deformation temperatures). In comparison to the untreated-as-deformed sample (blue data points), MR branches deviate more from each other after deformation for 100 turns at RT of the BMVA-pretreated sample (green data points). The difference might be caused by large residual ferromagnetic particles embedded in the Ag-matrix which contribute some AMR. MR values decrease constantly with increasing parallel applied field, reaching a maximum of 0.3 % at 22.5 kOe. For perpendicularly applied field, MR values decrease constantly with increasing field, except at  $H = 8$  kOe where a slight increase of MR was observed. At 22.5 kOe, a change of resistivity of -0.5 % (perpendicular) was reached.

In comparison to literature values [25], a much higher GMR value of 5.8 % was reported for mechanical alloyed (ball-milled)  $\text{Ag}_{70}\text{Fe}_{4.5}\text{Co}_{25.5}$  (in at%). This GMR amplitude was measured at much lower temperatures (10 K) and higher fields (30 kOe). Furthermore, the work of Cohen et al. also shows that the GMR drops to 1.6% when the ferromagnetic content is 30 at% and the atomic fractions of Fe and Co are equal.

Improvements in GMR amplitude of AgFeCo may be realized by replacing more Fe with Co. However, suitable process parameters still need to be found to optimize the microstructure to reduce AMR contribution.

### 4.3. Cr-based compositions

The successful HPT processability of Cr-based alloys strongly depends on the prior processing route. Weissitsch et al. reported enhanced HPT processability of Fe-Cr alloys by using the arc melting route instead of the powder processing route [37]. Therefore, arc melting was chosen as the prior processing route to obtain NC and homogeneously deformed CrFeCo alloys. In contrast to the previously investigated Ag- and Cu-based alloys, a higher pressure (7.5 GPa) and lower rotational speed ( $0.63 \text{ min}^{-1}$ ) were applied.

#### 4.3.1. Results of $\text{Cr}_{64}\text{Fe}_{27}\text{Co}_9$

Figure 30 shows LM images of the sample cross-section of  $\text{Cr}_{64}\text{Fe}_{27}\text{Co}_9$  after HPT deformation in dependency of the number of applied turns and the deformation temperature. As can be seen, fewer cracks in the sample were obtained by increasing the deformation temperature and decreasing the applied shear strain by decreasing the number of turns.

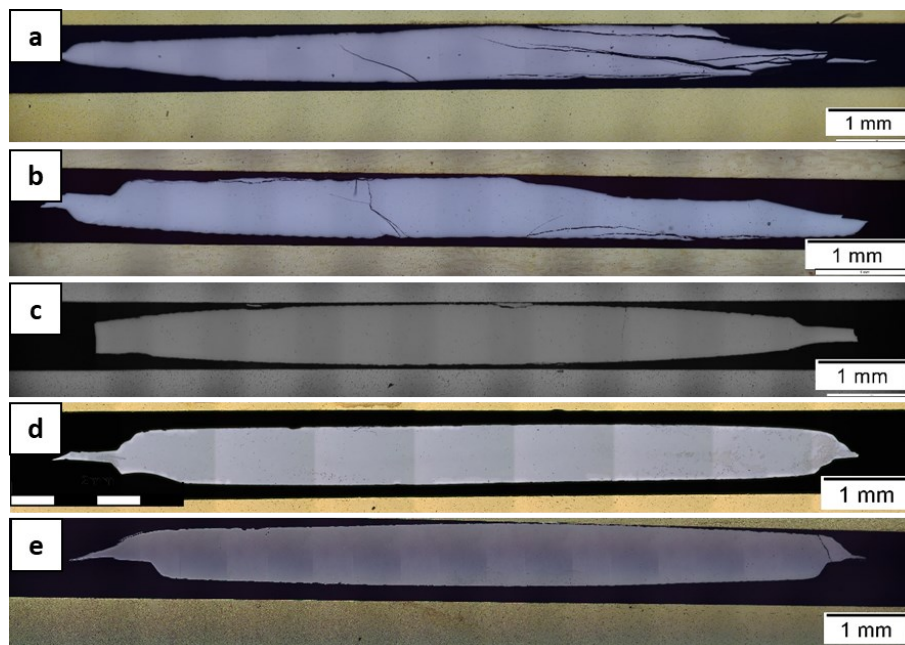


Figure 30: LM images of the macrostructure of  $\text{Cr}_{64}\text{Fe}_{27}\text{Co}_9$  after HPT deformation for (a) 20 turns at RT, (b) 10 turns at RT, (c) 5 turns at  $400^\circ\text{C}$ , (d) 2 turns at  $400^\circ\text{C}$ , and (e) 1 turn at  $400^\circ\text{C}$ .

Cracks occur mainly in the radial sample direction in samples deformed for 10-20 turns at RT (see Figure 30 (a) and (b)). By increasing the deformation temperature to  $400^\circ\text{C}$ , nearly crack-free samples were obtained. The cracks oriented in the axial sample direction in Figure 30 (c) and (e) were caused by sample preparation. No cracks appear in the sample deformed for 2 turns at  $400^\circ\text{C}$  (Figure 30 (d)).

The microstructures of as-deformed (and annealed)  $\text{Cr}_{64}\text{Fe}_{27}\text{Co}_9$  samples in dependency of the processing parameters are shown in Figure 31. As can be seen in (a)-(d), a homogeneous microstructure in the NC regime was obtained in each case. Despite many cracks, deformation for 20 turns at RT resulted in the smallest observed grain size. The low phase contrast in (a) indicates the formation of a supersaturated solid solution. A similar microstructure was obtained in (b). Nevertheless, samples in Figure 31 (a) and (b) were not used for further MR measurements, since the as-deformed samples were too brittle for the extraction of MR samples.

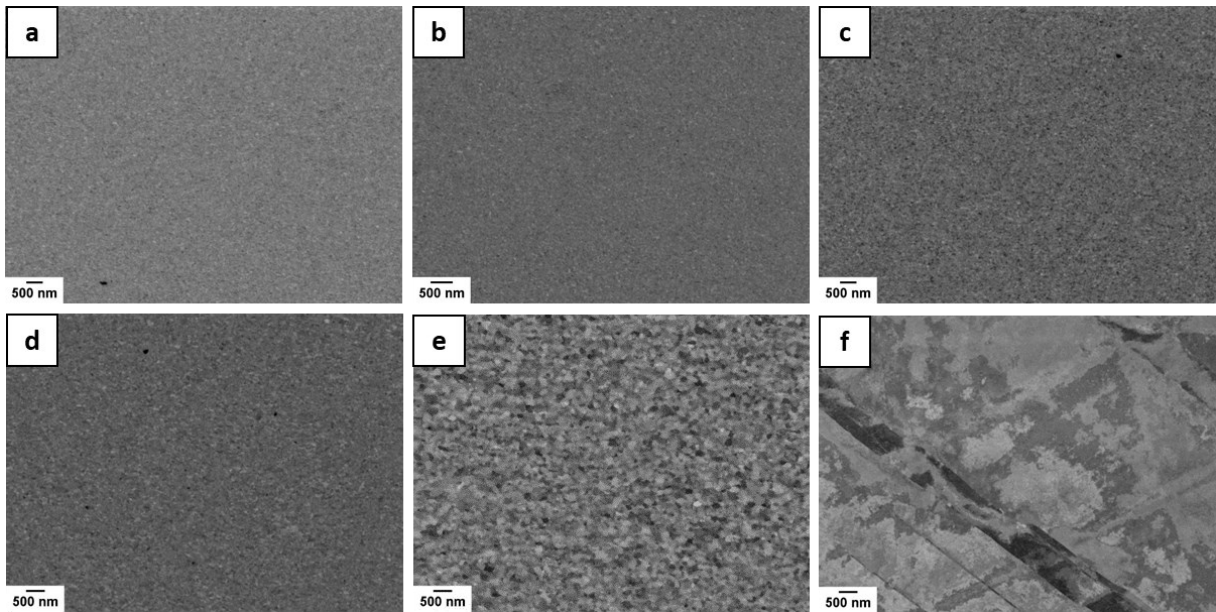


Figure 31: SEM micrographs of the microstructure of  $\text{Cr}_{64}\text{Fe}_{27}\text{Co}_9$  after HPT deformation for (a) 20 turns at RT, (b) 10 turns at RT, (c) 5 turns at  $400^\circ\text{C}$ , (d) 2 turns at  $400^\circ\text{C}$ , (e) 2 turns at  $400^\circ\text{C}$  + subsequently annealed for 1h at  $520^\circ\text{C}$ , and (f) 1 turn at  $400^\circ\text{C}$ . The micrographs were taken at  $r = 3$  mm.

In the micrographs, Cr-particles are supposed to appear darkest and Co-particles brightest, whereby Fe-particles exhibit a phase-contrast between Cr and Fe due to Z-contrast. However, there is only a small difference between the atomic numbers of Co and Fe, therefore an exact identification is not possible. Moreover, superimposing channeling contrast is also present. Somewhat coarser grains were obtained by rising the deformation temperature to  $400^\circ\text{C}$ , as can be seen in the micrographs in (c) and (d). Figure 31 (e) shows the annealed state (1h at  $520^\circ\text{C}$ ) of the sample deformed with 2 turns at  $400^\circ\text{C}$  (Figure 31 (d)). Significant grain growth was obtained after subsequent annealing. In contrast, hardly any deformation took place after deformation for 1 turn at  $400^\circ\text{C}$  (see Figure 31 (f)), resulting in a coarse and needle-like

microstructure. There was probably insufficient friction between the sample surface and the anvils. Consequently, the sample slipped between the anvils and did not deform properly.

Thus, only samples deformed for 2 turns and 5 turns at 400°C were used for further MR measurements, since they are crack-free and show the desired microstructure.

The averaged chemical composition of these samples was determined using EDX. The sample deformed for 5 turns at 400°C (Figure 31 (c)) consists of 63.6 wt% Cr, 26.9 wt% Fe, and 9.5 wt% Co. The sample deformed for 2 turns at 400°C (Figure 31 (d)) consists of 63.7 wt% Cr, 26.8 wt% Fe, and 9.5 wt% Co. The arc melting route is more accurate than the powder route since the deviations from the nominal composition are negligible.

Figure 32 shows XRD patterns of  $\text{Cr}_{64}\text{Fe}_{27}\text{Co}_9$  after HPT processing with different numbers of applied turns at different deformation temperatures. The measurement was carried out on HPT disc halves for the samples deformed at RT (black and blue patterns) since the extraction of MR samples was not possible. At higher deformation temperatures (400°C), XRD measurements were performed on MR samples (labeled with (MR)).

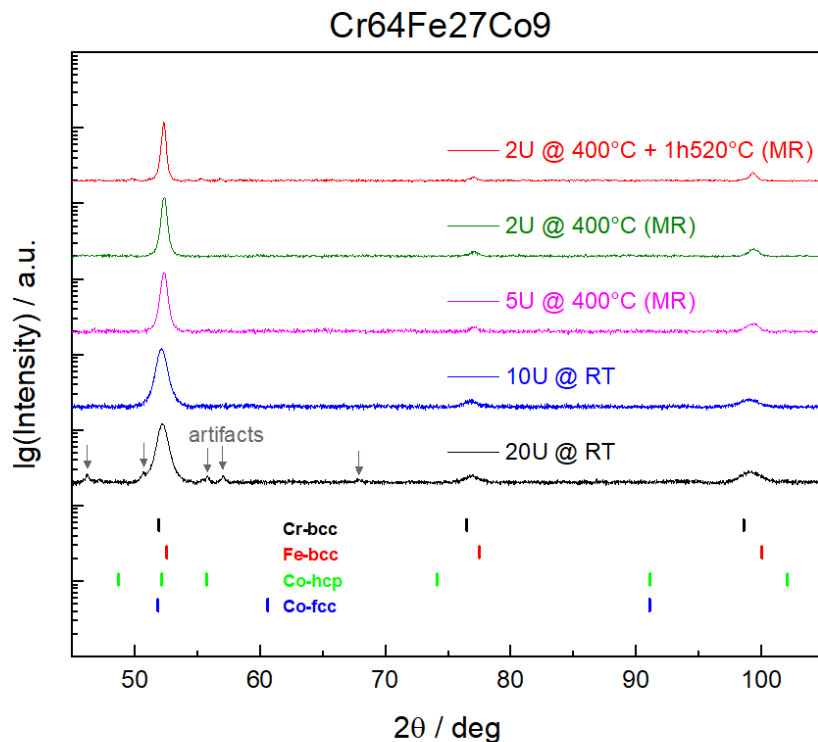


Figure 32: XRD patterns of as-deformed (and annealed)  $\text{Cr}_{64}\text{Fe}_{27}\text{Co}_9$  samples with different processing parameters.

HPT disc halves were fixed with plasticine on a polymer substrate, whilst MR samples were fixed with petroleum jelly on a Si substrate. As already observed in the previous Ag- and Cu-based compositions, measurement artifacts (indicated with gray arrows) can occur when samples were fixed with plasticine. All as-deformed samples exhibit mixed peaks of Cr-bcc and Fe-bcc, resulting in a single-phase bcc structure. No Co peaks appear in the measured patterns. Thus, it can be assumed that the bcc matrix is supersaturated with Co. It should be noted that the calculated patterns of Cr-bcc, Fe-bcc, Co-hcp, and Co-fcc nearly overlap at  $2\theta \approx 52^\circ$ . Therefore, the intensity of Co peaks might be too low for detection. Even after annealing for 1h at 520°C (red pattern), no phase separation took place. This indicates a high single-phase stability of  $\text{Cr}_{64}\text{Fe}_{27}\text{Co}_9$ . Furthermore, peak narrowing is visible with decreasing number of applied turns. Annealing (red pattern) resulted also in a smaller FWHM compared to the as-deformed state (green pattern). This indicates a coarsening of grain size with decreasing number of applied turns (and increasing deformation temperature), agreeing with the observed microstructures in Figure 31.

MR measurements (see Figure 33) were only performed on crack-free as-deformed and annealed  $\text{Cr}_{64}\text{Fe}_{27}\text{Co}_9$  samples, showing a NC microstructure. All as-deformed samples exhibit a linear decrease in resistivity with increasing magnetic field and thus no saturation behavior.

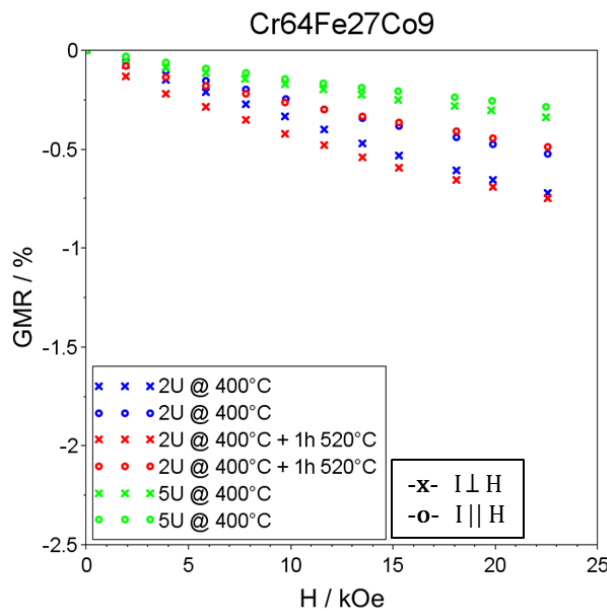


Figure 33: Decrease in resistivity in dependency of the applied magnetic field of as-deformed and annealed  $\text{Cr}_{64}\text{Fe}_{27}\text{Co}_9$ .

After deformation for 5 turns at 400°C (green data points), a nearly perfect GMR behavior was achieved. GMR amplitudes of 0.29 % and 0.34 % were measured at 22.5 kOe for the parallel and perpendicular  $I$  to  $H$  direction. A higher difference of MR branches (parallel and perpendicular) and thus a higher deviation from the perfect GMR behavior was observed for the less deformed sample (2 turns at 400°C). However, higher GMR amplitudes of 0.52 % (parallel) and 0.72 % (perpendicular) were achieved compared to the sample deformed with 5 turns at 400°C. Subsequent annealing for 1h at 520°C (red data points) resulted in a slight deviation from the linear shape. In comparison to the as-deformed state, GMR amplitudes were found at the maximum applied field. In general, a higher ferromagnetic content can lead to AMR contribution, which would explain the deviation of the MR branches.

In comparison to literature values [45], GMR values of about 1.8 % (perpendicular) and 1.4 % (parallel) were found in magnetically optimized FeCrCo samples (CROVAC 10/380) at a measuring temperature of 10 K. At 300 K, lower GMR amplitudes of approximately 0.6 % (perpendicular) and 0.3 % (parallel) were observed. It should be mentioned, that these GMR values were estimated out of Fig.6 in reference [45] for an applied field of about 22.5 kOe. The measured RT GMR values of as-deformed  $\text{Cr}_{64}\text{Fe}_{27}\text{Co}_9$  (2 turns at 400°C) are somewhat higher than the GMR amplitudes in literature at equivalent conditions. Furthermore, the same deviation of MR branches (perpendicular and parallel) occurred in the literature, as observed for as-deformed and annealed  $\text{Cr}_{64}\text{Fe}_{27}\text{Co}_9$  in Figure 33 (blue and red data points). These FeCrCo samples in the literature were fabricated by vacuum melting without subsequent SPD. However, the exact composition of the magnetically optimized FeCrCo sample is not known. Furthermore, a higher drop in resistivity of 3 % was reported for higher applied fields of 80 kOe and lower measuring temperatures at 10 K. This leads to the assumption that enhanced GMR amplitudes can be expected for  $\text{Cr}_{64}\text{Fe}_{27}\text{Co}_9$  for similar measuring conditions.



### 4.3.2. Results of $\text{Cr}_{78}\text{Fe}_{16}\text{Co}_6$

Figure 34 shows LM images of the sample cross-section of  $\text{Cr}_{78}\text{Fe}_{16}\text{Co}_6$  after HPT deformation with different processing parameters. After deformation for 8 turns at RT, a massive crack formation can be observed in  $\text{Cr}_{78}\text{Fe}_{16}\text{Co}_6$ , which led to the fracture of the sample. As a consequence, the number of applied turns was reduced to decrease the applied shear strain. In addition, higher deformation temperatures were chosen to enhance HPT-processability and reduce crack formation. As can be seen in Figure 34 (b) and (c), crack formation and fracture could be significantly reduced. Nevertheless, cracks are present in the radial and the axial sample direction.

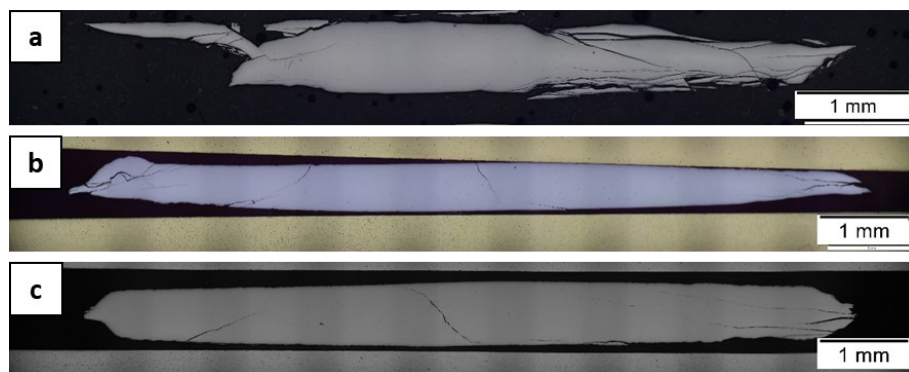


Figure 34: LM images of the macrostructure of  $\text{Cr}_{78}\text{Fe}_{16}\text{Co}_6$  after HPT deformation for (a) 8 turns at RT, (b) 4 turns at RT, and (c) 2 turns at  $400^\circ\text{C}$ .

In contrast to the composition with lower Cr content (see Figure 30 (d)), no crack-free sample could be formed, though the same deformation parameters (2 turns at  $400^\circ\text{C}$ ) were used. The decreasing HPT-processability of Fe-Cr alloys with increasing Cr content was already reported in previous works [37]. Since none of the as-deformed samples are free of cracks, no additional heat treatment was conducted.

To investigate the microstructure of as-deformed  $\text{Cr}_{78}\text{Fe}_{16}\text{Co}_6$  in more detail, SEM micrographs (see Figure 35) were carried out. Due to sample fracture after deformation for 8 turns at RT, the acquisition of micrographs was not possible at  $r = 3$  mm. Thus, they were performed at the maximum possible radius at  $r = 2$  mm. As can be seen in Figure 35 (a)-(c), increasing grain sizes were observed the lower the number of applied turns and the higher the deformation temperature. Deformation at RT (a) and (b) led to a homogeneous microstructure with NC grains. However, grains in (b) are somewhat larger than in (a). In general, Cr particles are supposed to appear darkest and Co-particles brightest, whereby Fe-particles exhibit a phase-contrast between Cr and Fe due to Z-contrast.

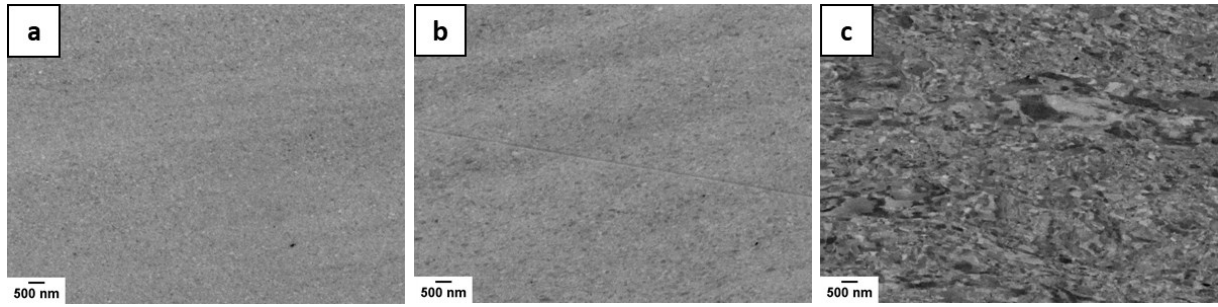


Figure 35: SEM micrographs of the microstructure of  $\text{Cr}_{78}\text{Fe}_{16}\text{Co}_6$  after HPT deformation for (a) 8 turns at RT, (b) 4 turns at RT, and (c) 2 turns at  $400^\circ\text{C}$ . The micrograph in (a) was taken at  $r = 2$  mm and in (b) and (c) at  $r = 3$  mm.

However, there is only a small difference between the atomic numbers of Co and Fe, therefore an exact identification is not possible. Moreover, superimposing channeling contrast is also present. The low phase-contrast in Figure 35 (a) and (b) indicates good intermixing of the phases. After deformation for 2 turns at  $400^\circ\text{C}$ , an inhomogeneous deformed microstructure was obtained (see Figure 35 (c)). In comparison, much larger grains were observed in different sizes.

The averaged chemical composition of these samples was determined using EDX. The sample deformed for 8 turns at RT (Figure 35 (a)) consists of 74.2 wt% Cr, 15.3 wt% Fe, and 5.4 wt% Co. The sample deformed for 4 turns at RT (Figure 35 (b)) consists of 74.4 wt% Cr, 16.2 wt% Fe, and 5.4 wt% Co. The sample deformed for 2 turns at  $400^\circ\text{C}$  (Figure 35 (c)) consists of 77.3 wt% Cr, 16.8 wt% Fe, and 5.9 wt% Co.

Figure 36 shows XRD patterns of  $\text{Cr}_{78}\text{Fe}_{16}\text{Co}_6$  after HPT processing with different numbers of applied turns at different deformation temperatures. In all measured patterns in Figure 36 a bcc single-phase structure is visible. The patterns show mixed peaks of Cr-bcc and Fe-bcc. However, no Co peaks occur, indicating supersaturation of the bcc-matrix with Co (black and blue patterns). This correlates with samples deformed at RT, showing a supersaturated microstructure (see micrographs in Figure 35 (a) and (b)). The presence of Co-grains cannot be excluded in the low deformed material, but the intensity of Co peaks might be too low to be detected (red pattern) and the weak signal could vanish in the background signal. It should be noted that the calculated patterns of Cr-bcc, Fe-bcc, Co-hcp, and Co-fcc nearly overlap at  $2\theta \approx 52^\circ$ . At this position Co-hcp might be present, however, disappeared in the signal of the former peak (Fe and Cr). In addition, the transformation of Co-hcp to Co-fcc can be excluded since the sample deformed for 2 turns at  $400^\circ\text{C}$  shows insufficient co-deformation of phases.

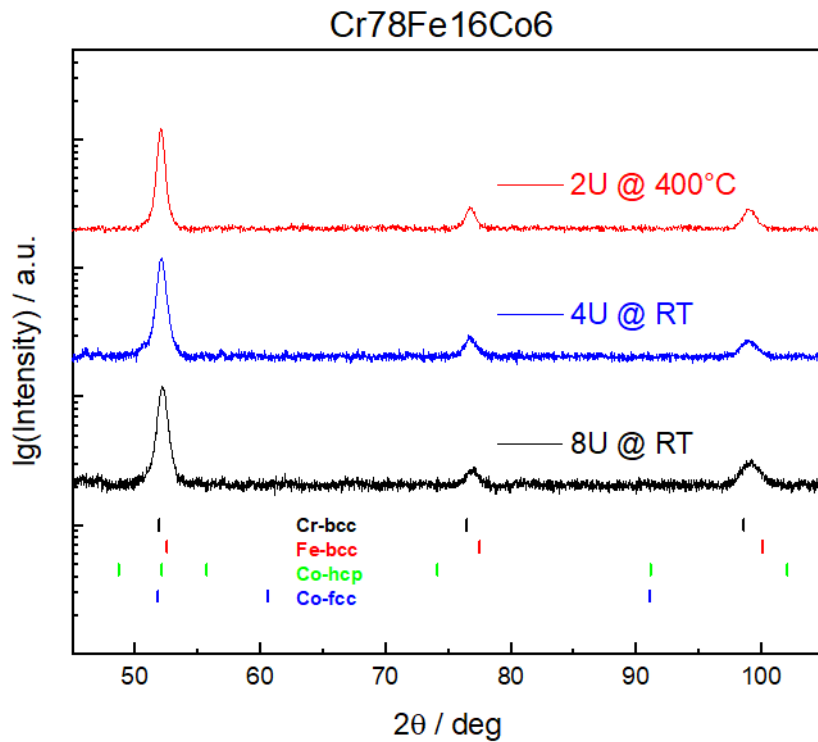


Figure 36: XRD patterns of differently as-deformed Cr<sub>78</sub>Fe<sub>16</sub>Co<sub>6</sub> samples.

In comparison, it comes to a peak narrowing with decreasing number of applied turns, especially at increased deformation temperatures (400°C). This indicates grain coarsening and agrees with the observed microstructure in Figure 35 (a)-(c).

For this composition, MR measurements were not performed. The as-deformed samples were too brittle to extract MR samples by a further cutting and grinding process.

#### 4.4. Discussion of the magnetoresistance

In this chapter, MR results of different matrix materials (Ag, Cu, Cr) containing the same ferromagnetic phase (FeCo) are discussed. Moreover, Cu-based compositions with different elements as ferromagnetic phases (FeCo and FeNi) are compared.

Figure 37 compares the GMR amplitudes of as-deformed and annealed Cr-, Ag-, and Cu-based compositions with the same elements (Fe and Co) for the ferromagnetic phases.  $\text{Cu}_{82}\text{Fe}_{12}\text{Co}_6$  provides the highest GMR amplitudes comparing the as-deformed states (blue data points in Figure 37 (c)). Even higher values were obtained after subsequent annealing (green and red data points), as can be seen in Figure 37 (c). The MR branches (perpendicular and parallel) do not deviate significantly. Thus, a perfect isotropic GMR behavior was obtained for the Cu-based composition. However, no saturation behavior was observed for  $\text{Cu}_{82}\text{Fe}_{12}\text{Co}_6$ .

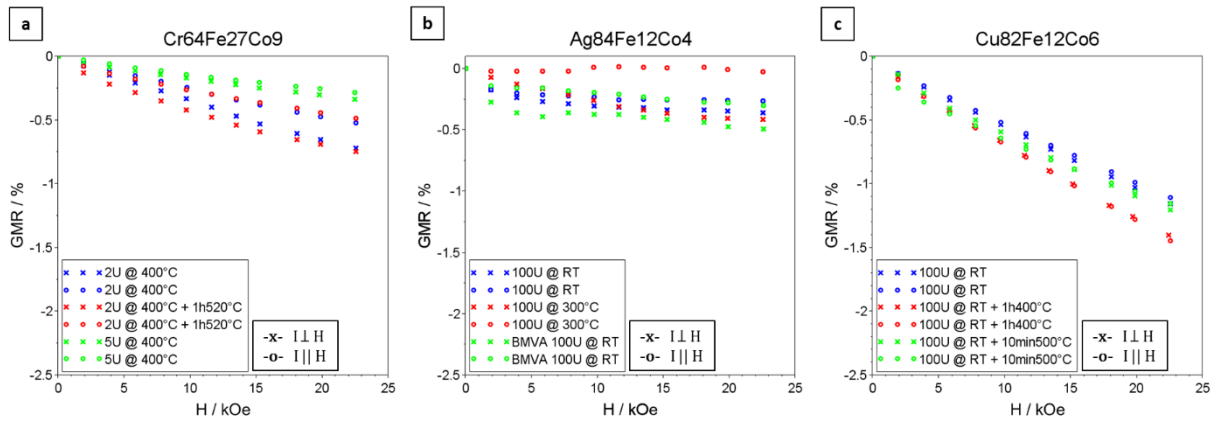


Figure 37: Comparison of GMR amplitudes of as-deformed and annealed Cr-, Ag-, and Cu-based compositions with Fe and Co as ferromagnetic phases.

A saturation in GMR was observed for  $\text{Ag}_{84}\text{Fe}_{12}\text{Co}_4$  deformed for 100 turns at RT (blue data points) in Figure 37 (b). However, only approximately one-third of the GMR amplitude of as-deformed  $\text{Cu}_{82}\text{Fe}_{12}\text{Co}_6$  was achieved, despite similar ferromagnetic volume contents (20 vol%). This might be caused by the obtained microstructure of  $\text{Ag}_{84}\text{Fe}_{12}\text{Co}_4$ , showing bigger residual ferromagnetic particles. Bigger ferromagnetic particles saturate already at lower applied fields compared to smaller ones [15]. However, spin-dependent scattering is reduced due to the lower surface-to-volume ratio of bigger ferromagnetic particles, leading to lower GMR amplitudes [22]. The Ag-based composition shows a higher deviation of MR branches, indicating AMR contributions, due to the formation of magnetic multidomains [10,43].

The Cr-based composition (Figure 37 (a)) shows a somewhat higher GMR amplitude than as-deformed  $\text{Ag}_{84}\text{Fe}_{12}\text{Co}_4$  (Figure 37 (b)) after deformation for 2 turns at 400°C, whereas a

somewhat lower GMR amplitude after deformation for 5 turns at RT. It should be noted that the Cr-based composition exhibits a ferromagnetic volume fraction of approximately 40 %, and Ag- and Cu-based compositions about 20 %. A decreasing GMR was found for binary Cr-Fe for ferromagnetic contents above 20 vol% [46]. A higher ferromagnetic content favors the formation of magnetic clusters which lowers the MR [22,47]. Therefore, a higher drop in resistivity is expected to occur in the Cr-rich composition.

Since the Cu-based compositions showed the most promising results, a variety of heat treatments were performed to obtain the optimum GMR. Figure 38 shows a comparison of magnetic field-dependent resistivities of different Cu-based compositions which were equally processed (100 turns at RT) and annealed (1h at 400°C and 10min at 500°C).

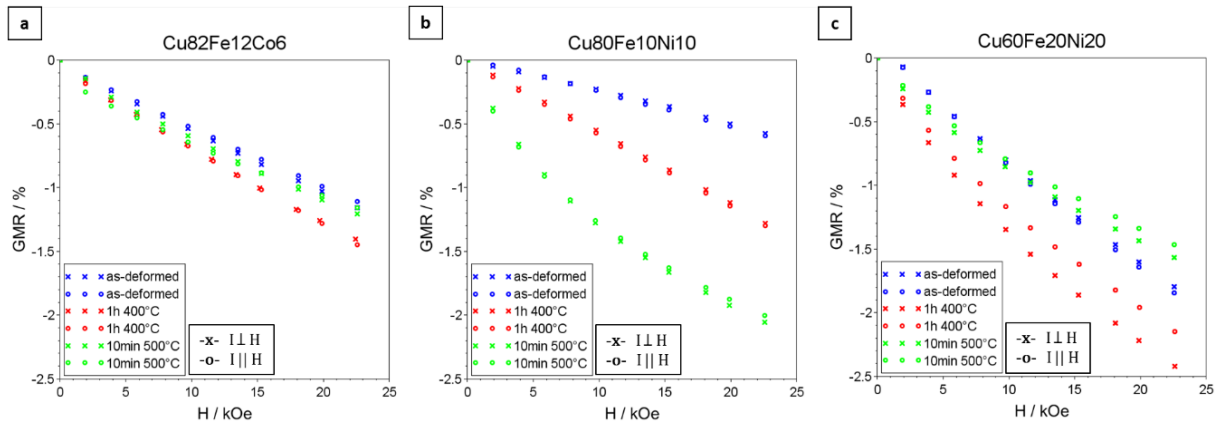


Figure 38: Comparison of GMR amplitudes of different Cu-based compositions which were similarly deformed and annealed.

All as-deformed samples (blue data points in Figure 38) show a linear and isotropic decrease in resistivity with increasing field. Cu<sub>60</sub>Fe<sub>20</sub>Ni<sub>20</sub> exhibits a higher GMR amplitude than Cu<sub>80</sub>Fe<sub>10</sub>Ni<sub>10</sub>, whereby Cu<sub>82</sub>Fe<sub>12</sub>Co<sub>6</sub> shows GMR values in between. Wang et al. found for as-deposited Cu-FeNi films an increasing GMR with increasing ferromagnetic volume fraction. An optimum GMR of 1.8 % was reached for 32 vol% FeNi for an applied field of 12.5 kOe. Above 32 vol%, GMR decreases for as-deposited Cu-FeNi films due to the formation of multidomain granules [47]. A similar GMR amplitude was reached for as-deformed Cu<sub>60</sub>Fe<sub>20</sub>Ni<sub>20</sub>. However, the applied field is about two times higher. It can be assumed, that even higher GMR values can be achieved for as-deformed CuFeNi for a ferromagnetic volume content between 20 % and 40 %. A peak in GMR was observed after annealing for 1h at 400°C of Cu<sub>60</sub>Fe<sub>20</sub>Ni<sub>20</sub> (red data points in (c)). However, the MR branches deviate, which might arise from the formation of multidomain granules leading to some AMR contributions. In comparison, no deviation of MR branches occurred after similar annealing of Cu<sub>82</sub>Fe<sub>12</sub>Co<sub>6</sub> and Cu<sub>80</sub>Fe<sub>10</sub>Ni<sub>10</sub> (see Figure 38

(a) and (b)) containing less ferromagnetic material. In general, subsequent annealing for 1h at 400°C (red data points) led for each Cu-based composition to enhanced GMR amplitudes. Except for  $\text{Cu}_{60}\text{Fe}_{20}\text{Ni}_{20}$ , annealing for 10min at 500°C (green data points) had a positive effect regarding GMR, especially for  $\text{Cu}_{80}\text{Fe}_{10}\text{Ni}_{10}$ . The drop in resistivity after annealing (10min at 500°C) is more than three times higher compared to its as-deformed state at the maximum applied field, demonstrating the utmost importance of adequate annealing treatments after SPD by HPT. Furthermore,  $\text{Cu}_{80}\text{Fe}_{10}\text{Ni}_{10}$  shows after annealing for 10min at 500°C (see (b)) a tendency of saturation. Generally, no heat treatment resulted in a saturation of GMR. In almost all Cu-based compositions, the resistivity decreases linearly with increasing field, which might be explained by the occurrence of superparamagnetic particles [48]. Superparamagnetism can occur when ferromagnetic particles decrease under a critical size. It was found that superparamagnetism only influences the GMR saturation process but not its saturation value [15]. All Cu-based compositions show high-temperature phase stability after HPT deformation. Therefore, subsequent annealing did not change the grain size significantly. The GMR saturation behavior (goal: high GMR at low fields) could not be enhanced, but the absolute values of GMR were improved by proper annealings for certain systems.

## 5. Summary

This thesis aims to fabricate a variety of severe plastically deformed bulk materials showing the granular GMR effect. The granular GMR effect arises from spin-dependent scattering at interfaces between nonmagnetic and ferromagnetic phases. Thus, the mutual immiscibility of both phases is mandatory. Consequently, ternary alloy systems, Cu-Fe-Ni, Cu-Fe-Co, Ag-Fe-Co, and Cr-Fe-Co, but also binary alloy systems, Ag-Fe and Ag-Co, were chosen. Furthermore, bulk materials show only the granular GMR effect, when the nonmagnetic matrix contains finely distributed small ferromagnetic particles in the NC regime. Such granular structures are formed classically with bottom-up techniques, e.g., melt spinning and magnetron sputtering. However, top-down techniques, such as HPT (a SPD method), were barely studied for the fabrication of bulk nanomagnetic structures. Especially, no investigations were yet made to the magnetoresistive properties of HPT-processed Cu-Fe-Co, Cu-Fe-Ni, Cr-Fe-Co, Ag-Fe-Co, Ag-Fe, and Ag-Co. The powders were mixed to compositions containing 20 vol% ferromagnetic phases since a peak in granular GMR is expected to occur for this ferromagnetic content. In addition, a ferromagnetic volume fraction of 40 % was chosen for CuFeNi and CrFeCo. The nanogranular GMR structure in bulk form was generated either directly during the SPD process or indirectly through the formation of a supersaturated solid solution. For the latter, appropriate subsequent heat treatments were conducted to enhance the saturation behavior and the magnetoresistive response of the materials by segregating fine ferromagnetic particles out of the supersaturated phase in a second step.

A variety of experiments, including LM, SEM, microhardness and XRD measurements were performed on the HPT-deformed (and annealed) materials to investigate the influence of microstructural changes on their magnetoresistive properties. These microstructural investigations were linked to MR measurements which were carried out in a self-built measurement setup. Therefore, the resistivity of the materials was measured with the four-point probe method at RT, while the current-carrying material was exposed to magnetic fields between 0 kOe and 22.5 kOe. Two measurements were performed for each sample to ensure the isotropic GMR behavior. The current was first applied parallel and then perpendicular to the magnetic field. In general, the measurement accuracy of the MR setup could be validated by a reference measurement of severely deformed tungsten.

The granular GMR effect could be achieved in all Cu-based compositions processed by HPT deformation.  $\text{Cu}_{60}\text{Fe}_{20}\text{Ni}_{20}$  shows the highest GMR amplitude compared to the as-deformed states. XRD measurements reveal a fcc single-phase structure in all as-deformed Cu-based compositions, indicating the formation of a supersaturated solid solution. Subsequent heat treatments (1h at 400°C and 10min at 500°C) led to higher GMR amplitudes in  $\text{Cu}_{82}\text{Fe}_{12}\text{Co}_6$

and  $\text{Cu}_{80}\text{Fe}_{10}\text{Ni}_{10}$  samples. Annealing  $\text{Cu}_{80}\text{Fe}_{10}\text{Ni}_{10}$  for 10min at  $500^\circ\text{C}$  resulted in a more than threefold amplification of the GMR amplitude at the maximum applied field. Generally, the highest GMR of 2.45 % (at 22.5 kOe) was found in  $\text{Cu}_{60}\text{Fe}_{20}\text{Ni}_{20}$  after annealing for 1h at  $400^\circ\text{C}$ . A weakening of the effect was observed for higher annealing temperatures (and durations). The maximum measured RT GMR of  $\text{Cu}_{60}\text{Fe}_{20}\text{Ni}_{20}$  is somewhat higher than the reported GMR value of spinodal decomposed  $\text{Cu}_{60}\text{Fe}_{20}\text{Ni}_{20}$  films at similar measuring conditions. In comparison to the literature,  $\text{Cu}_{82}\text{Fe}_{12}\text{Co}_6$  and  $\text{Cu}_{80}\text{Fe}_{10}\text{Ni}_{10}$  show smaller GMR values. However, no saturation in GMR was observed in any Cu-based composition after deformation and annealing. Furthermore, the microstructure of as-deformed  $\text{Cu}_{60}\text{Fe}_{20}\text{Ni}_{20}$  exhibits astonishingly high-temperature stability up to  $600^\circ\text{C}$ , which corresponds to a homologous temperature of 0.64 of Cu. In comparison, CuFeNi exhibits a higher single-phase stability than CuFeCo.

The ferromagnetic phase within  $\text{Ag}_{83}\text{Co}_{17}$  did not co-deform properly in contrast to  $\text{Ag}_{84}\text{Fe}_{16}$ . Thus, no MR measurements were carried out on AgCo. However, Co was partly replaced with Fe to improve the refinement process of the ferromagnetic phase. In addition, the elemental powders were BMVA pre-treated, which enhanced the co-deformability. Granular GMR was measured for as-deformed  $\text{Ag}_{84}\text{Fe}_{16}$  and  $\text{Ag}_{84}\text{Fe}_{12}\text{Co}_4$ . However, some contributions of AMR were presently arising from residual ferromagnetic particles in the Ag-matrix. These occur especially in BMVA pretreated samples, due to agglomeration of the initial powders. AgFe and AgFeCo show a saturation behavior in GMR, though exhibiting much smaller GMR amplitudes compared to Cu-based compositions and literature values of the same compositions.

Regarding the CrFeCo system, HPT processability succeeded only for CrFeCo with lower Cr content. XRD measurements revealed a bcc single-phase structure of as-deformed  $\text{Cr}_{64}\text{Fe}_{27}\text{Co}_9$ , indicating the formation of a supersaturated solid solution. Granular GMR was measured also in HPT processed  $\text{Cr}_{64}\text{Fe}_{27}\text{Co}_9$  samples. However, GMR amplitudes of  $\text{Cr}_{64}\text{Fe}_{27}\text{Co}_9$  are in the range of the Ag-based compositions, whereby showing no saturation behavior. Furthermore, AMR contributions are present due to the high ferromagnetic content leading to the percolation of magnetic domains.

In general, SPD by HPT is a suitable method for the fabrication of bulk samples showing the granular GMR effect. However, the investigated alloy systems are not suitable for GMR-based sensor applications, since they show only at high applied fields a sufficient drop in resistivity. Higher GMR amplitudes are expected to occur in higher applied fields at lower measuring temperatures. Ag-based compositions seem to be promising concerning applications. Nevertheless, the RT GMR amplitude must be enhanced by finding further processing steps to obtain a suitable microstructure free of residual particles.



## 6. References

- [1] W. Thomson, XIX. On the electro-dynamic qualities of metals:—Effects of magnetization on the electric conductivity of nickel and of iron, *Proc. R. Soc. Lond.* 8 (1857) 546–550. <https://doi.org/10.1098/rspl.1856.0144>.
- [2] A. Bland, B. Heinrich, eds., *Ultrathin magnetic structures*, Springer, Berlin ; New York, 1994.
- [3] Y. Pu, Charge-spin conversion in 2D systems, in: *Spintronic 2D Materials*, Elsevier, 2020: pp. 125–136. <https://doi.org/10.1016/B978-0-08-102154-5.00004-7>.
- [4] M.N. Baibich, J.M. Broto, A. Fert, F.N. Van Dau, F. Petroff, P. Etienne, G. Creuzet, A. Friederich, J. Chazelas, Giant Magnetoresistance of (001)Fe/(001)Cr Magnetic Superlattices, *Phys. Rev. Lett.* 61 (1988) 2472–2475. <https://doi.org/10.1103/PhysRevLett.61.2472>.
- [5] G. Binasch, P. Grünberg, F. Saurenbach, W. Zinn, Enhanced magnetoresistance in layered magnetic structures with antiferromagnetic interlayer exchange, *Phys. Rev. B.* 39 (1989) 4828–4830. <https://doi.org/10.1103/PhysRevB.39.4828>.
- [6] I. Ennen, D. Kappe, T. Rempel, C. Glenske, A. Hütten, Giant Magnetoresistance: Basic Concepts, Microstructure, Magnetic Interactions and Applications, *Sensors.* 16 (2016) 904. <https://doi.org/10.3390/s16060904>.
- [7] V.D. Krishna, K. Wu, A.M. Perez, J.-P. Wang, Giant Magnetoresistance-based Biosensor for Detection of Influenza A Virus, *Front. Microbiol.* 7 (2016). <https://doi.org/10.3389/fmicb.2016.00400>.
- [8] J.Q. Xiao, J.S. Jiang, C.L. Chien, Giant magnetoresistance in nonmultilayer magnetic systems, *Phys. Rev. Lett.* 68 (1992) 3749–3752. <https://doi.org/10.1103/PhysRevLett.68.3749>.
- [9] A.E. Berkowitz, J.R. Mitchell, M.J. Carey, A.P. Young, S. Zhang, F.E. Spada, F.T. Parker, A. Hutten, G. Thomas, Giant magnetoresistance in heterogeneous Cu-Co alloys, *Phys. Rev. Lett.* 68 (1992) 3745–3748. <https://doi.org/10.1103/PhysRevLett.68.3745>.
- [10] S. Wurster, L. Weissitsch, M. Stückler, P. Knoll, H. Krenn, R. Pippan, A. Bachmaier, Tuneable Magneto-Resistance by Severe Plastic Deformation, *Metals.* 9 (2019) 1188. <https://doi.org/10.3390/met9111188>.
- [11] S. Wurster, M. Stückler, L. Weissitsch, T. Müller, A. Bachmaier, Microstructural Changes Influencing the Magnetoresistive Behavior of Bulk Nanocrystalline Materials, *Applied Sciences.* 10 (2020) 5094. <https://doi.org/10.3390/app10155094>.
- [12] K. Suehiro, S. Nishimura, Z. Horita, S. Mitani, K. Takanashi, H. Fujimori, High-pressure torsion for production of magnetoresistance in Cu–Co alloy, *J Mater Sci.* 43 (2008) 7349–7353. <https://doi.org/10.1007/s10853-008-2813-9>.
- [13] T.A. Rabedeau, M.F. Toney, R.F. Marks, S.S.P. Parkin, R.F.C. Farrow, G.R. Harp, Giant magnetoresistance and Co-cluster structure in phase-separated Co-Cu granular alloys, *Phys. Rev. B.* 48 (1993) 16810–16813. <https://doi.org/10.1103/PhysRevB.48.16810>.

- [14] S. Rubin, M. Holdenried, H. Micklitz, A model system for the GMR in granular systems:, *Journal of Magnetism and Magnetic Materials*. 203 (1999) 97–99. [https://doi.org/10.1016/S0304-8853\(99\)00200-0](https://doi.org/10.1016/S0304-8853(99)00200-0).
- [15] J.-Q. Wang, G. Xiao, Transition-metal granular solids: Microstructure, magnetic properties, and giant magnetoresistance, *Phys. Rev. B*. 49 (1994) 3982–3996. <https://doi.org/10.1103/PhysRevB.49.3982>.
- [16] L.H. Chen, S. Jin, T.H. Tiefel, T.C. Wu, Giant magnetoresistance in spinodally decomposed Cu–Ni–Fe films, *Journal of Applied Physics*. 76 (1994) 6814–6816. <https://doi.org/10.1063/1.358138>.
- [17] L.H. Chen, S. Jin, T.H. Tiefel, R. Ramesh, Creation of bulk, superlatticelike structure and giant magnetoresistance effect in a deformed Cu-Ni-Fe alloy, *Appl. Phys. Lett.* 64 (1994) 1039–1041. <https://doi.org/10.1063/1.110963>.
- [18] R.E. Hummel, Electrical Conduction in Metals and Alloys, in: *Electronic Properties of Materials*, Springer New York, New York, NY, 2011: pp. 79–114. [https://doi.org/10.1007/978-1-4419-8164-6\\_7](https://doi.org/10.1007/978-1-4419-8164-6_7).
- [19] Tech Report: HPL-95-60: Magnetoresistance Overview, (n.d.). <https://www.hpl.hp.com/techreports/95/HPL-95-60.html> (accessed November 30, 2021).
- [20] J. Inoue, GMR, TMR and BMR, in: *Nanomagnetism and Spintronics*, Elsevier, 2009: pp. 15–92. <https://doi.org/10.1016/B978-0-444-53114-8.00002-9>.
- [21] P. Grünberg, D.E. Bürgler, Metallic Multilayers: Discovery of Interlayer Exchange Coupling and GMR, in: Y. Xu, D.D. Awschalom, J. Nitta (Eds.), *Handbook of Spintronics*, Springer Netherlands, Dordrecht, 2016: pp. 107–126. [https://doi.org/10.1007/978-94-007-6892-5\\_6](https://doi.org/10.1007/978-94-007-6892-5_6).
- [22] C. Wang, Z. Guo, Y. Rong, T.Y. Hsu (Xu Zuyao), A phenomenological theory of the granular size effect on the giant magnetoresistance of granular films, *Journal of Magnetism and Magnetic Materials*. 277 (2004) 273–280. <https://doi.org/10.1016/j.jmmm.2003.10.033>.
- [23] W. Zhang, R. Yang, Giant magnetoresistance of magnetic granular films in an effective medium theory, *Physics Letters A*. 255 (1999) 343–348. [https://doi.org/10.1016/S0375-9601\(99\)00115-2](https://doi.org/10.1016/S0375-9601(99)00115-2).
- [24] S. Ikeda, T. Houga, W. Takakura, Y. Ueda, Magnetoresistance in  $(\text{Co}_x\text{Fe}_{1-x})_{20}\text{Cu}_{80}$  granular alloys produced by mechanical alloying, *Materials Science and Engineering: A*. 217–218 (1996) 376–380. [https://doi.org/10.1016/S0921-5093\(96\)10331-2](https://doi.org/10.1016/S0921-5093(96)10331-2).
- [25] N.S. Cohen, Q.A. Pankhurst, L.F. Barquín, Structural and magnetoresistive properties of mechanically alloyed Fe-Co-Ag, *J. Phys.: Condens. Matter*. 11 (1999) 8839–8853. <https://doi.org/10.1088/0953-8984/11/45/308>.
- [26] Y.T. Zhu, T.C. Lowe, T.G. Langdon, Performance and applications of nanostructured materials produced by severe plastic deformation, *Scripta Materialia*. 51 (2004) 825–830. <https://doi.org/10.1016/j.scriptamat.2004.05.006>.
- [27] R. Valiev, Nanostructuring of metals by severe plastic deformation for advanced properties, *Nature Mater.* 3 (2004) 511–516. <https://doi.org/10.1038/nmat1180>.

- [28] R. Pippan, S. Scheriau, A. Taylor, M. Hafok, A. Hohenwarter, A. Bachmaier, Saturation of Fragmentation During Severe Plastic Deformation, *Annu. Rev. Mater. Res.* 40 (2010) 319–343. <https://doi.org/10.1146/annurev-matsci-070909-104445>.
- [29] R. Pippan, A. Hohenwarter, S. Scheriau, A. Bachmaier, Nanokristalline Metalle. Neue Werkstoffe aus plastischer Hochverformung, *Phys. Unserer Zeit.* 41 (2010) 23–29. <https://doi.org/10.1002/piuz.201001215>.
- [30] ultra fine grained steel, UFG steel, carbon, strength, UTS, ductility, welding, EBSD, texture, GND, RVE, modeling, processing, (n.d.). <http://www.dierk-raabe.com/ultrafine-grained-steels/> (accessed November 11, 2021).
- [31] A. Bachmaier, R. Pippan, Generation of metallic nanocomposites by severe plastic deformation, *International Materials Reviews.* 58 (2013) 41–62. <https://doi.org/10.1179/1743280412Y.0000000003>.
- [32] A. Hohenwarter, A. Bachmaier, B. Gludovatz, S. Scheriau, R. Pippan, Technical parameters affecting grain refinement by high pressure torsion, *International Journal of Materials Research.* 100 (2009) 1653–1661. <https://doi.org/10.3139/146.110224>.
- [33] R. Pippan, F. Wetscher, M. Hafok, A. Vorhauer, I. Sabirov, The Limits of Refinement by Severe Plastic Deformation, *Adv. Eng. Mater.* 8 (2006) 1046–1056. <https://doi.org/10.1002/adem.200600133>.
- [34] K.S. Kormout, R. Pippan, A. Bachmaier, Deformation-Induced Supersaturation in Immiscible Material Systems during High-Pressure Torsion: Deformation-Induced Supersaturation, *Adv. Eng. Mater.* 19 (2017) 1600675. <https://doi.org/10.1002/adem.201600675>.
- [35] O. Renk, R. Pippan, Saturation of Grain Refinement during Severe Plastic Deformation of Single Phase Materials: Reconsiderations, Current Status and Open Questions, *Mater. Trans.* 60 (2019) 1270–1282. <https://doi.org/10.2320/matertrans.MF201918>.
- [36] F.L. Matthews, R.D. Rawlings, *Composite Materials: Engineering and Science.*, Elsevier Science, Cambridge, 2014. <https://public.ebookcentral.proquest.com/choice/publicfullrecord.aspx?p=1639482> (accessed January 26, 2022).
- [37] L. Weissitsch, M. Stücker, S. Wurster, R. Pippan, A. Bachmaier, Processing of Nanostructured Bulk Fe-Cr Alloys by Severe Plastic Deformation, *MSF.* 1016 (2021) 1603–1610. <https://doi.org/10.4028/www.scientific.net/MSF.1016.1603>.
- [38] M. Stücker, L. Weissitsch, S. Wurster, P. Felfer, H. Krenn, R. Pippan, A. Bachmaier, Magnetic dilution by severe plastic deformation, *AIP Advances.* 10 (2020) 015210. <https://doi.org/10.1063/1.5128058>.
- [39] W. ESPE, *Materials of high vacuum technology; vol.1, p. 18-76, (1987).*
- [40] K. Edalati, S. Toh, M. Arita, M. Watanabe, Z. Horita, High-pressure torsion of pure cobalt: hcp-fcc phase transformations and twinning during severe plastic deformation, *Appl. Phys. Lett.* 102 (2013) 181902. <https://doi.org/10.1063/1.4804273>.
- [41] R. Lardé, J.M. Le Breton, Influence of the milling conditions on the magnetoresistive properties of a Cu<sub>80</sub>(Fe<sub>0.7</sub>Co<sub>0.3</sub>)<sub>20</sub> granular alloy elaborated by mechanical alloying,

- Journal of Magnetism and Magnetic Materials. 290–291 (2005) 1120–1122. <https://doi.org/10.1016/j.jmmm.2004.11.471>.
- [42] A. Bachmaier, A. Katzensteiner, S. Wurster, K. Aristizabal, S. Suarez, R. Pippan, Thermal stabilization of metal matrix nanocomposites by nanocarbon reinforcements, *Scripta Materialia*. 186 (2020) 202–207. <https://doi.org/10.1016/j.scriptamat.2020.05.014>.
- [43] V. Franco, X. Batlle, A. Labarta, CoFe–Cu granular alloys: From noninteracting particles to magnetic percolation, *Journal of Applied Physics*. 85 (1999) 7328–7335. <https://doi.org/10.1063/1.369357>.
- [44] C.S. Martins, F.P. Missell, Annealing dependence of giant magnetoresistance in CuFeNi alloys, *Journal of Applied Physics*. 87 (2000) 4840–4842. <https://doi.org/10.1063/1.373176>.
- [45] A. Hutten, A. Handstein, D. Eckert, H.-K. Muller, L. Schultz, Giant magnetoresistance in pseudo-binary bulk alloys, *IEEE Trans. Magn.* 32 (1996) 4695–4697. <https://doi.org/10.1109/20.539121>.
- [46] T. Sugawara, K. Takanashi, K. Hono, H. Fujimori, Study of giant magnetoresistance behavior in sputter-deposited Cr–Fe alloy films, *Journal of Magnetism and Magnetic Materials*. 159 (1996) 95–102. [https://doi.org/10.1016/0304-8853\(95\)00948-5](https://doi.org/10.1016/0304-8853(95)00948-5).
- [47] C.Z. Wang, Z.H. Guo, Y.H. Rong, T.Y. Hsu, Magnetic-Transport and Microstructure of FeNi–Cu Nanogranular Films, *MSF*. 475–479 (2005) 3733–3736. <https://doi.org/10.4028/www.scientific.net/MSF.475-479.3733>.
- [48] M. Stückler, H. Krenn, R. Pippan, L. Weissitsch, S. Wurster, A. Bachmaier, Magnetic Binary Supersaturated Solid Solutions Processed by Severe Plastic Deformation, *Nanomaterials*. 9 (2018) 6. <https://doi.org/10.3390/nano9010006>.

## 7. Appendix

### 7.1. Cu-based compositions



Figure A.1: LM images of the HPT sample cross-section of (a)  $\text{Cu}_{82}\text{Fe}_{12}\text{Co}_6$ , (b)  $\text{Cu}_{60}\text{Fe}_{20}\text{Ni}_{20}$ , and (c)  $\text{Cu}_{80}\text{Fe}_{10}\text{Ni}_{10}$  after deformation for 100 turns at RT.

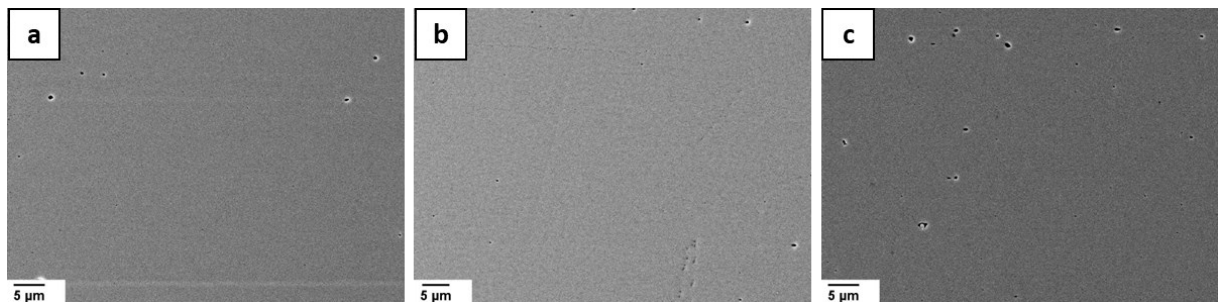


Figure A.2: SEM micrographs of the microstructure of (a)  $\text{Cu}_{82}\text{Fe}_{12}\text{Co}_6$ , (b)  $\text{Cu}_{60}\text{Fe}_{20}\text{Ni}_{20}$ , and (c)  $\text{Cu}_{80}\text{Fe}_{10}\text{Ni}_{10}$  after deformation for 100 turns at RT.

## 7.2. Ag-based compositions

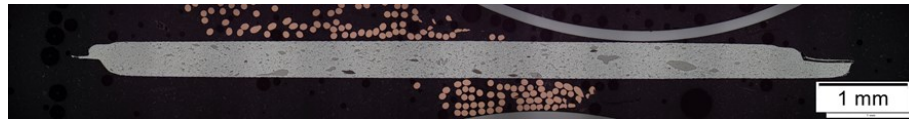


Figure A.3: LM images of the HPT sample cross-section of  $\text{Ag}_{83}\text{Co}_{17}$  after deformation for 100 turns at RT.

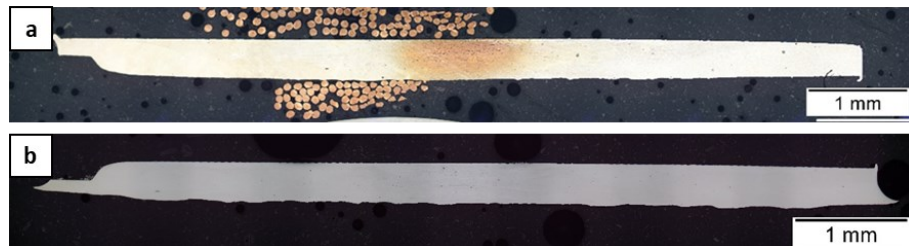


Figure A.4: LM images of the HPT sample cross-section of (a) untreated  $\text{Ag}_{84}\text{Fe}_{16}$ , and (b) BMVA-pretreated  $\text{Ag}_{84}\text{Fe}_{16}$  after deformation for 100 turns at RT.



Figure A.5: LM images of  $\text{Ag}_{84}\text{Fe}_{12}\text{Co}_4$  after deformation for (a) 100 turns at RT (untreated), (b) 100 turns at 300°C (untreated), and (c) 100 turns at RT (BMVA-pretreated).

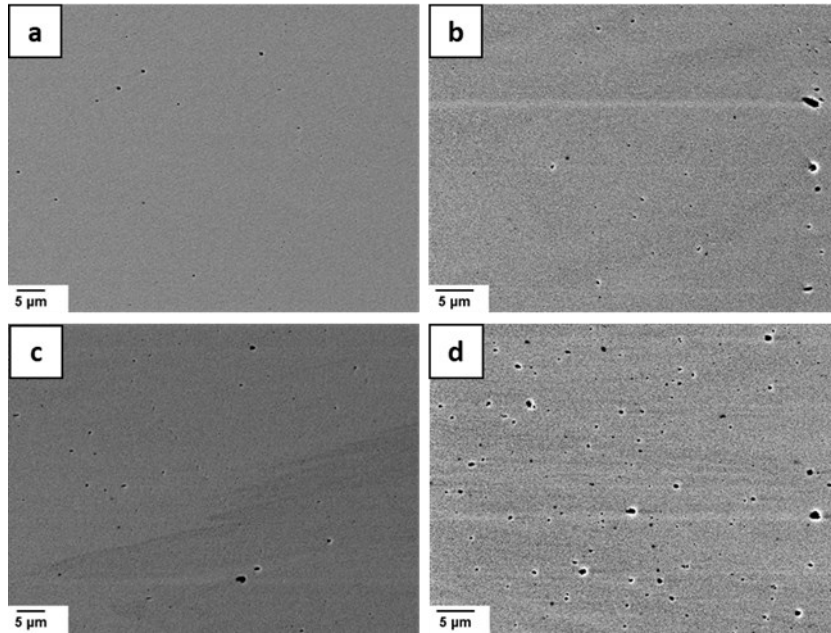


Figure A.6: SEM micrographs above show the microstructure of (a) untreated and as-deformed  $\text{Ag}_{84}\text{Fe}_{16}$  and (b) BMVA-pretreated and as-deformed  $\text{Ag}_{84}\text{Fe}_{16}$ . The micrographs below (c) and (d) show the respective microstructures of (a) and (b) after annealing for 1h at  $400^\circ\text{C}$ .

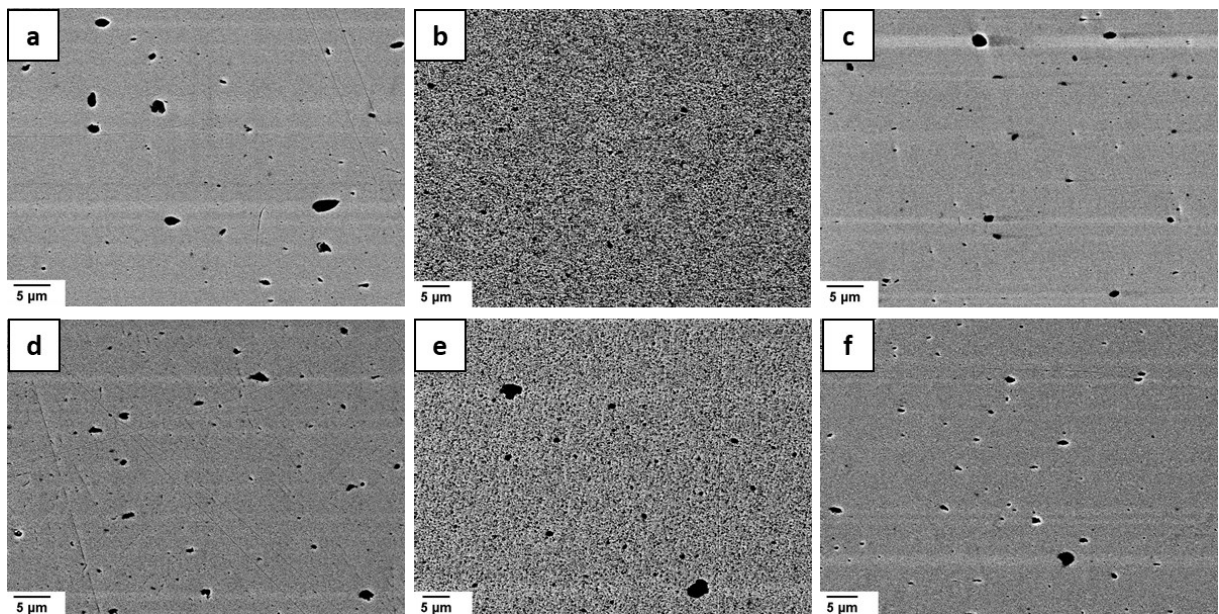


Figure A.7: SEM micrographs of the microstructure of  $\text{Ag}_{84}\text{Fe}_{12}\text{Co}_4$  after deformation for (a) 100 turns at RT, (b) 100 turns at  $300^\circ\text{C}$ , and (c) 100 turns at RT (BMVA-pretreated). The bottom micrographs (d), (e), and (f) show the respective microstructures of (a), (b), and (c) after annealing for 1h at  $400^\circ\text{C}$ .

### 7.3. Cr-based compositions

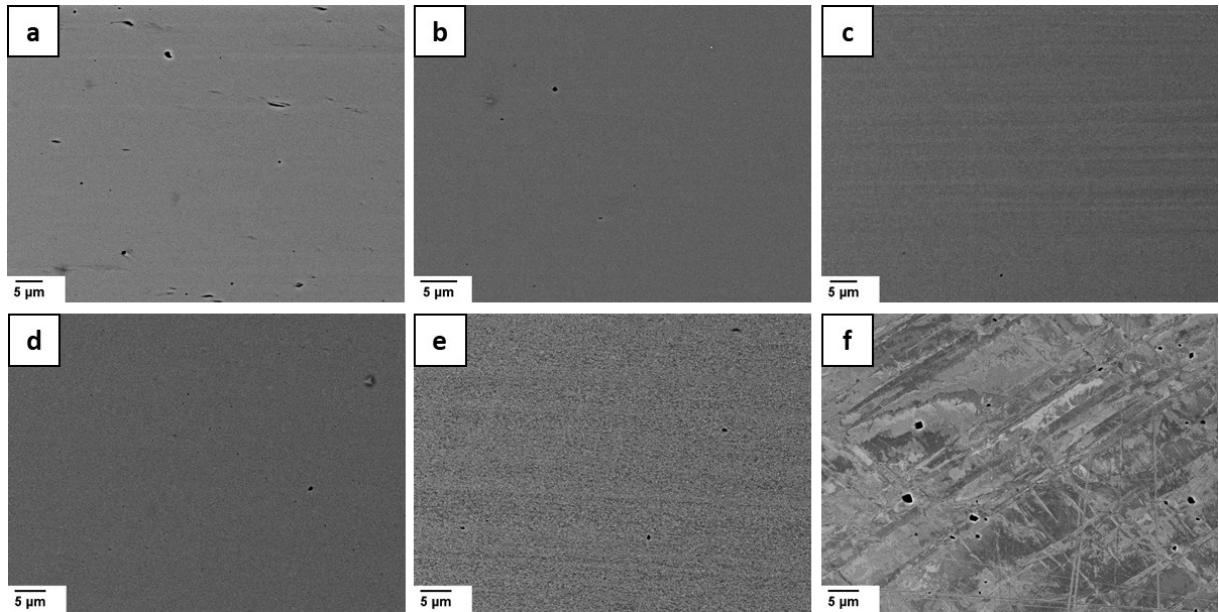


Figure A.8: SEM micrographs of the microstructure of  $\text{Cr}_{64}\text{Fe}_{27}\text{Co}_9$  after HPT deformation for (a) 20 turns at RT, (b) 10 turns at RT, (c) 5 turns at 400°C, (d) 2 turns at 400°C, (e) 2 turns at 400°C + subsequently annealed for 1h at 520°C, and (f) 1 turn at 400°C.

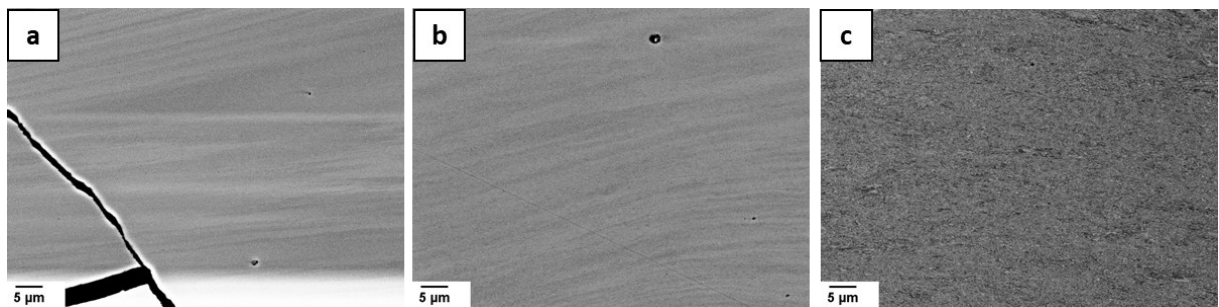


Figure A.9: SEM micrographs of the microstructure of  $\text{Cr}_{78}\text{Fe}_{16}\text{Co}_6$  after HPT deformation for (a) 8 turns at RT, (b) 4 turns at RT, and (c) 2 turns at 400°C. The micrograph in (a) was taken at  $r = 2$  mm and in (b) and (c) at  $r = 3$  mm.